Optical wave manipulation and signal processing in anisotropic photorefractive materials

Habilitation Thesis

Author(s):
Montemezzani, Germano Luigi

Publication date:
2003

Permanent link:
https://doi.org/10.3929/ethz-a-004491891

Rights / license:
In Copyright - Non-Commercial Use Permitted

Optical wave manipulation and signal processing in anisotropic photorefractive materials

Inaugural Thesis

Germano Montemezzani

Institute of Quantum Electronics
Swiss Federal Institute of Technology
Zurich, Switzerland

Table of Contents

Abstract

The photorefractive effect, an indirect nonlinear optical effect mediated by the material photoconductivity, offers the unique opportunity to obtain high sensitivity light-light interaction already at moderate intensity levels below 1 W/cm^2 typical of unfocused continuous wave laser beams. We distinguish two kinds of photorefractive effects. In the conventional one the photoconductivity arises from carriers photoexcited from mid-gap levels, while in the interband photorefractive effect the carriers are produced by band-to-band transitions through the absorption of higher energy photons.

In this work we concentrate on two important aspects of photorefractive nonlinear optics that were not addressed previously. We show that interband photorefractive effects offers new interesting opportunities for optical parallel processing and clarify the role of the various anisotropic material properties on the strength of conventional and interband photorefractive gratings.

As compared to the conventional one, the interband photorefractive effect leads to a much faster response speed of the order of few μs at the 1 W/cm^2 intensity level and to dynamic holographic gratings which are very robust against simultaneous illumination with light having sub-band gap energy. The usefulness of this effect for optical signal processing and for wave manipulation is shown by demonstrating: (a) a high resolution optically addressed spatial light modulator operating at a refresh cycle of 70 μs based on KNbO$_3$; (b) an optical joint Fourier transform correlator based on Sn$_2$P$_2$S$_6$ which can operate at the record frame rate of 10 kHz; (c) light induced dynamic waveguides in KNbO$_3$ that can be reconfigured in real time.

We present here the first study elucidating the role of the complete set of anisotropic material properties on the resulting coupling constant among the optical waves. Anisotropic crystals are in general the materials of choice for obtaining large refractive index changes for both, conventional and interband photorefractive effects. This anisotropy has an enormous influence on the magnitude of the nonlinear interaction. As an important new result, it is shown theoretically and experimentally that an anisotropy of the photoexcitation process with respect to light polarization dramatically influences the two-wave mixing coupling gain landscape in wavevector space. By proper material engineering, this effect can be used for the enhancement of the maximum gain in a given photorefractive medium. Diffraction of light at volume gratings is obviously also influenced by an anisotropy of the medium and/or of the grating itself. The well known isotropic coupled wave theory of Kogelnik (H. Kogelnik, Bell Syst. Tech. J. **48**, 2909 (1969).) is extended here to the anisotropic case. This leads to the first complete set of analytic expressions valid in general geometries and that describe mixtures of anisotropic phase and absorption gratings with arbitrary phase relationship. This approach is valid also for non photorefractive media. A predictive understanding of the

diffraction properties of emerging holographic materials with strong optical anisotropy can be gained. These include for instance organic crystals, liquid crystals, and polymer dispersed liquid crystals.

Chapter 1

Introduction

Conventional nonlinear optical effects are due to the higher order material polarization induced by oscillating optical fields [1]. The order of the effect is associated with the corresponding nonlinear susceptibility $\chi^{(2)}$, $\chi^{(3)}$, and so on. These effects can give dramatic and basically instantaneous light induced changes of the optical properties of a material provided that the optical intensity is very large. This can be realized by using high energy short laser pulses and highly focused light, leading to effects such as second- or third-harmonic generation, optical rectification, sum and difference frequency generation, optical parametric amplification or nonlinear refraction.

In contrast, the efficiency and sensitivity of these effects become very small when using low power unfocused light from continuous wave (cw) lasers. Therefore, these effects are in general not well suited for applications involving moderate intensity levels of the order of 1 W/cm^2 or less and for exploiting one of the most attractive properties of light, its parallelism. The photorefractive effect, which concerns this work the most, offers the possibility to obtain high sensitivity light-light interaction at these moderate intensity levels. As will be discussed in more detail in Chapt. 2, photorefraction is an indirect nonlinear optical effect and can occur in $\chi^{(2)}$ optically nonlinear materials, which are noncentrosymmetric (piezoelectric) materials showing the linear electro-optic effect. It is indirect in the sense that one of the two electric fields at the source of the induced polarization is a spatially modulated quasi-static electric field produced indirectly by the optical wave (or waves) as a result of photoinduced charge transport in the bulk of the material. This transport of charges leads to an highly increased sensitivity with respect to conventional direct nonlinear effects for cw power levels. However, the charge transport also brings about the most important drawback. Moving a sufficient number of charges needs time and the 1 W/cm^2 response speed for the most commonly used materials may typically range between a fraction of 1 ms and a few minutes.

Most of the materials showing efficient photorefractive effects are strongly anisotropic. Although photorefractive nonlinear optics is becoming a mature research field [2–8] a complete description of the influence of all the various material anisotropies was never developed. This work closes this gap. We describe the role of all relevant materials anisotropies and give new general expressions predicting the light diffraction properties and wave mixing interaction. An important new finding is that an anisotropy of the photoexcitation cross-section with respect to light polarization plays a dramatic role on the wave interaction strength. The new predictions are confirmed experimentally and can give guidance for optimizing material production and geometrical arrangements for different tasks.

In conventional photorefraction the photoexcitation at the origin of the charge trans-

port process occurs from mid-gap defect levels introduced by intentional crystal doping. In this work we treat also a very interesting alternative which we call the interband photorefractive effect. In this case the photoexcitation occurs by using light with a photon energy able to induce band-to-band transitions. This leads to a much faster rise of the internal space-charge fields and opens interesting perspectives for parallel optical processing and optical wave manipulation tasks, such as dynamic splitting and switching. An optical addressed spatial light modulator (incoherent-to-coherent converter), a high speed optical correlator and the creation of dynamic light induced waveguides all basing on this effect are demonstrated here.

We begin in Chapt. 2 by presenting first the simplest band transport model of the photorefractive effect describing the formation of the light induced space-charge electric field. For reasons that will become clear in Chapt. 5, unlike in standard literature, the initial equations are written with the density of the "usefully dissipated" energy instead of the light intensity as the driving quantity. This is the optical energy which is locally dissipated for the generation of mobile charge carriers and ensures that any anisotropy of the photoexcitation process is correctly taken into account. In addition to the theory for conventional photorefraction, we describe in Chapt. 2 our own simplest model for interband photorefractive effects and give a short review of other models applying in special situations, such as the presence of electron-hole competition, ionic movement, or multiple active levels.

For anisotropic crystals containing a modulated space-charge grating the effective dielectric constant and the strength of the electro-optic response depend in a complicated way on the piezoelectric, elastic and photoelastic properties of the material. This is discussed in Chapter 3. The phenomena are illustrated for $BaTiO_3$ and $KNbO_3$, two among the materials showing the strongest photorefractive effects [9–11]. It is also shown that the occurrence of enigmatic fanning patterns observed after light passes a $BaTiO_3$ crystal can be fully explained as a direct consequence of these mechanical coupling effects.

Chapter 4 gives a general treatment of light diffraction at anisotropic volume gratings in optically anisotropic materials. We build on the (isotropic) coupled-wave theory of Kogelnik [12] and extend it to the anisotropic case. The new expressions are valid in general geometries and can be used to describe anisotropic or isotropic diffraction at phase and/or absorption gratings with arbitrary relative phase and produced by any physical mechanism. For transmission type holograms their validity extends also to the case of gain gratings. The new relationships evidence the role played by walk-off and by the anisotropy of the modulated part of the real and imaginary components of the dielectric tensor. Therefore their use is particularly important for holographic materials having strong birefringence and/or containing gratings with strongly anisotropic properties, such as several organic crystals, liquid crystals, oriented polymers or polymer dispersed liquid crystals.

The two-wave mixing technique can be viewed as being the basis of the majority of applications of the photorefractive effect. Chapter 5 treats two-wave mixing in view of the various material anisotropies. It is shown and experimentally verified that an anisotropy of the photoexcitation cross section has a dramatic influence on the expected two-wave mixing gain. This can lead to a significant gain enhancement in proper geometries, thus giving important guidance for material engineering and selection of the

best geometrical arrangement.

In the final chapter we give a brief summary of the observed photorefractive effects under interband photoexcitation in the two materials $KNbO_3$ and $Sn_2P_2S_6$ and demonstrate three potential applications for optical processing and wave manipulation. A high speed high resolution incoherent-to-coherent converter with superior performance with respect to what is achievable with the conventional photorefractive effect is demonstrated using $KNbO_3$. An unprecedented optical correlation rate of 10 kHz is achieved by using pulsed interband gratings in $Sn_2P_2S_6$ in connection with a holographic memory stage for the fast image input. Finally, it is shown that light can be guided by the refractive index channels produced by the interband photorefractive effect. In $KNbO_3$ these dynamic waveguides are easily reconfigured in a time frame of the order of 100 μs.

Chapter 2

Photorefractive effects

By its literal interpretation, the word photorefraction may describe all kind of photoinduced changes of the refractive index of a material and therefore any photoinduced phase grating would belong to this category. However, it has become customary in the literature to consider only a smaller class of materials as those showing the photorefractive effect [3, 5, 6, 8]. These materials possess two important properties, they are photoconductive and exhibit an electro-optic effect. Photoconductivity ensures charge transport, resulting in the creation of a space-charge distribution under inhomogeneous illumination. The electro-optic effect translates the internal electric fields induced by the inhomogeneous space-charges into a modulation of the material refractive index. In more recent literature the concept of photorefraction has been slightly expanded to include also the effects observed in some polymeric compounds, where the refractive index change is governed by a field assisted molecular reorientation [13]. The photorefractive effect is distinguished from many other mechanisms leading to optical induced refractive index gratings also by the fact that it is an intrinsically nonlocal effect, in the sense that the maximum refractive index change does not need to occur at the same spatial locations where the light intensity or the rate of photoexcitation processes are largest.

In the strict sense mentioned above, the photorefractive process, that culminates with the formation of a phase grating or a spatially variation of the refractive index, is described by the mechanisms shown in the schematic diagram of Fig. 2. The three most important properties which a material must fulfill are depicted in the outlined boxes, optical absorption, charge transport and electro-optic effect or field assisted molecular reorientation. Optical absorption and charge transport together give rise to photoconductivity, while the electro-optic effect or molecular reorientation translate the internal electric field into refractive index changes. The mechanisms in the top loop indicated by dashed arrows are also necessary in most materials under low intensity continuous illumination. Under these conditions, a large number of trapping sites allows to create a considerable space-charge modulation amplitude, even though the number of mobile charges is small at any moment in time. Large photorefractive effects without the necessity of trapping may be observed by studying the initial response to intense short-pulsed light [14–16] , or, in some conditions, by using a continuous light with a wavelength short enough to produce interband photoexcitations [17] and thus create a large number of mobile electrons and holes.

In this chapter we describe the simplest theoretical model for the formation of a modulated space-charge distribution and space-charge field in photorefractive materials. Besides the single-carrier band-model relevant to conventional photoexcitation of carriers
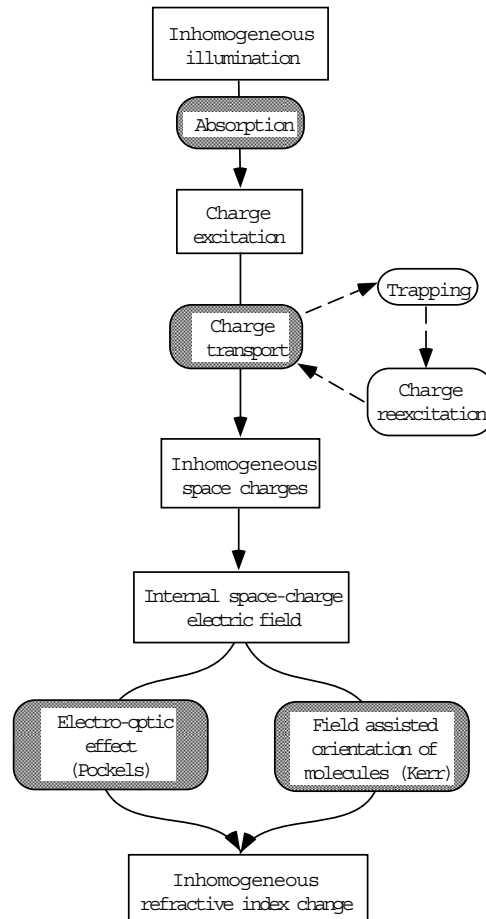
Figure 2.1: The important mechanisms for the photorefractive effect.

from a mid-gap impurity level to the conduction or valence band we will treat in some detail the simplest model describing interband photorefractive effects induced by direct band-to-band carrier phototransitions. This model is important for the understanding of the applications of interband photorefractive effects reported in Chapter 6. In addition, a few refined models put forward in the literature to describe special situations such as the presence of multiple defect levels, simultaneous electron and hole charge transport, or ionic charge compensation and grating fixing, will be cited briefly. The translation of the space-charge field distribution calculated in this chapter into a refractive-index modulation by means of the electro-optic effect will be the matter of Chapter 3.

2.1   Single-carrier band transport model

Crystalline photorefractive materials can be considered as wide band-gap semiconductors containing mid-gap impurity levels. The dynamics of charge redistribution can therefore be described by rate equations which are similar to the ones which are common in semiconductor physics. The most successful model describing the formation of the space-charge gratings in photorefractive crystals is the single-level single-carrier band model introduced by the Kiev group in the second half of the seventies [18–20]. This 'Kukhtarev-Vinetskii' model can explain satisfactorily the experimental observations in most materials. Alternative approaches such as Feinberg's 'Hopping model' [21] essentially give the same predictions.

Here we present a slight modification of the standard 'Kukhtarev-Vinetskii' model that takes explicitely the number density of photoexcited carriers (or what we call the 'usefully dissipated energy') as the primary quantity driving the whole photorefractive effect. In this way the correct grating modulation is calculated even in the case where the photoexcitation process is strongly anisotropic with respect to the recording waves polarization, the consequences of which will become clear in Chapter 5. The model presented here assumes the presence of a single active impurity level between the two bands. The valence of these impurity centers can change between the states A^{n+} and $A^{[n+1]+}$ by excitation/retrapping of electrons to and from the conduction band. Charge transport occurs only in the conduction band by means of drift, diffusion or the photogalvanic effect, the latter being due to the fact that upon thermalization the carriers can be emitted into the conduction band in a preferential direction due to asymmetric local potentials [22, 23].

Within the framework of the single-carrier single-level band model the charge redistribution and the creation of a space-charge electric field in a photorefractive material are governed by following equations

$$\frac{\partial N_D^+ (\vec{r}, t)}{\partial t} = (\chi w (\vec{r}, t) + \beta) \left(N_D - N_D^+ (\vec{r}, t) \right)$$
$$- \gamma n (\vec{r}, t) N_D^+ (\vec{r}, t), \tag{2.1a}$$

$$\frac{\partial n (\vec{r}, t)}{\partial t} = \frac{\partial N_D^+ (\vec{r}, t)}{\partial t} + \frac{1}{e} \vec{\nabla} \cdot \vec{J} (\vec{r}, t), \tag{2.1b}$$

$$\vec{J} (\vec{r}, t) = e n (\vec{r}, t) \overleftrightarrow{\mu} \cdot \vec{E} (\vec{r}, t) + k_B T \overleftrightarrow{\mu} \cdot \vec{\nabla} n (\vec{r}, t)$$
$$+ \chi w (\vec{r}, t) \left(N_D - N_D^+ (\vec{r}, t) \right) e \vec{L}_{pg}, \tag{2.1c}$$

$$\vec{\nabla} \cdot \vec{E} (\vec{r}, t) = \frac{e}{\varepsilon_{eff} \varepsilon_0} \left(N_D^+ (\vec{r}, t) - n (\vec{r}, t) - N_A \right), \tag{2.1d}$$

where n is the free electron concentration in the conduction band, N_D is the total donor concentration, N_D^+ is the concentration of ionized donors, N_A is the concentration of ionized donors in the dark, $\vec{J}$ is the current density vector, $\vec{E}$ is the electric field vector, $\chi = [\hbar (N_D - N_A)]^{-1}$ is a normalization constant, β is the dark generation rate, γ is the recombination constant, $\overleftrightarrow{\mu}$ is the electron mobility tensor, ε_0 is the permittivity of vacuum, ε_{eff} is the (scalar) effective dielectric constant for the given photorefractive configuration that will be discussed in more detail in Chapter 3, e is the absolute value of the elementary charge, k_B is the Boltzmann-constant, T is the absolute temperature, $\vec{r}$ is the position vector, t is the time, and $\vec{L}_{pg}$ is the photogalvanic drift-vector and depends on the direction of polarization of the illuminating light [1]. Finally, the driving quantity in the above equations is the "usefully dissipated energy" w, that is the optical energy which is locally dissipated for the generation of mobile charge carriers. It is defined as [25]

$$w(\vec{r}, t) = \frac{1}{2} \varepsilon_0 \left[\vec{\mathcal{E}} (\vec{r}, t) \cdot \overleftrightarrow{\kappa} \cdot \vec{\mathcal{E}}^* (\vec{r}, t) \right], \tag{2.2}$$

where $\vec{\mathcal{E}} (\vec{r}, t)$ is the complex amplitude of the total optical electric field obtained by

---

[1]An alternative description of the photogalvanic component $\vec{J}_{pg}$ to the current density (last term on the right-hand side of Eq. (2.1c)) relates it directly to the optical electric field via the photogalvanic tensor $\overleftrightarrow{\beta}$; $\vec{J}_{pg} (\vec{r}, t) = \vec{\mathcal{E}} (\vec{r}, t) \cdot \overleftrightarrow{\beta} \cdot \vec{\mathcal{E}}^* (\vec{r}, t)$. The third-rank tensor $\overleftrightarrow{\beta}$ contains the point group symmetry of the crystal and depends on extrinsic parameters such as doping level and reduction state of the material [23, 24] .

the coherent superposition of all the illuminating waves. The real second rank tensor $\overset{\leftrightarrow}{\kappa}$ describes the anisotropy of the photoexcitation process and is related to the absorptive part of the dielectric tensor, i.e. to the symmetric imaginary part $\overset{\leftrightarrow}{\varepsilon}''$ of the complex material dielectric tensor $\overset{\leftrightarrow}{\varepsilon} = \overset{\leftrightarrow}{\varepsilon}' + i\,\overset{\leftrightarrow}{\varepsilon}''$. It is defined as

$$\kappa_{kl} \equiv \phi_{kl}\left(\varepsilon''\right)_{kl}, \tag{2.3}$$

where the quantities ϕ_{kl} describe the light polarization dependence of the quantum efficiency, that is the probability that an absorbed photon of given polarization produces a photoexcited mobile carrier. Note that in Eq. (2.3) no summing over equal indices is performed.

For the present treatment we consider specifically the grating formed by the interference of two coherent plane waves of the form

$$\vec{\mathcal{E}}_S(\vec{r}, t) \equiv E_S\left(\vec{r}\right)\hat{e}_S \exp\left[i\left(\vec{k}_S \cdot \vec{r} - \omega t\right) - \alpha_S \hat{\zeta} \cdot \vec{r}\right], \tag{2.4a}$$

$$\vec{\mathcal{E}}_P(\vec{r}, t) \equiv E_P\left(\vec{r}\right)\hat{e}_P \exp\left[i\left(\vec{k}_P \cdot \vec{r} - \omega t\right) - \alpha_P \hat{\zeta} \cdot \vec{r}\right], \tag{2.4b}$$

the first representing the signal wave (S), the second the pump wave (P). Here $\hat{e}_S$ $(\hat{e}_P)$ are unit vectors along the direction of the optical electric field of the two waves, $E_S\,(E_P)$ are scalar complex amplitudes, $\vec{k}_S\,(\vec{k}_P)$ are the corresponding wave-vectors, and $\alpha_S\,(\alpha_P)$ are the amplitude absorption coefficient measured in the direction given by the unit vector $\hat{\zeta}$, which is normal to the entrance surface of the two waves into the recording material[2]. Interference of the two above plane waves leads to a sinusoidally varying expression for the time-averaged 'usefully dissipated energy',

$$w(\vec{r}) = w_0 \mathrm{Re}\left[1 + m\exp\left(i\vec{K}\cdot\vec{r}\right)\right], \tag{2.5}$$

where $\vec{K} \equiv \vec{k}_S - \vec{k}_P$ is the grating wavevector,

$$m\left(\vec{r}\right) = \frac{2E_S\left(\vec{r}\right)E_P^*\left(\vec{r}\right)\left[\hat{e}_S \cdot \overset{\leftrightarrow}{\kappa} \cdot \hat{e}_P\right]e^{-(\alpha_S+\alpha_P)\hat{\zeta}\cdot\vec{r}}}{|E_P\left(\vec{r}\right)|^2\left[\hat{e}_P \cdot \overset{\leftrightarrow}{\kappa} \cdot \hat{e}_P\right]e^{-2\alpha_P\hat{\zeta}\cdot\vec{r}} + |E_S\left(\vec{r}\right)|^2\left[\hat{e}_S \cdot \overset{\leftrightarrow}{\kappa} \cdot \hat{e}_S\right]e^{-2\alpha_S\hat{\zeta}\cdot\vec{r}}} \tag{2.6}$$

is the (complex) fringe modulation index, and

$$w_0 = |E_P\left(\vec{r}\right)|^2\left[\hat{e}_P \cdot \overset{\leftrightarrow}{\kappa} \cdot \hat{e}_P\right]e^{-2\alpha_P\hat{\zeta}\cdot\vec{r}} + |E_S\left(\vec{r}\right)|^2\left[\hat{e}_S \cdot \overset{\leftrightarrow}{\kappa} \cdot \hat{e}_S\right]e^{-2\alpha_S\hat{\zeta}\cdot\vec{r}} \tag{2.7}$$

is the average value of $w(\vec{r})$ corresponding to the incoherent superposition of the contributions of the signal and pump waves.

2.1.1   Steady-state

The steady-state situation is found by solving Eqs. (2.1) and (2.5) with all time derivatives equalling zero. By inserting only spatially homogeneous variables in these equations one can easily find expressions for the spatially averaged values n_0, N_{D0}^+ and J_0 of

---

[2]We choose here the same kind of coordinate representation that will be used in Chapt. 4 for the calculation of light diffraction at volume gratings in general geometries. The reason for calculating the absorption constants along the specific direction $\hat{\zeta}$ will become clear in Chapter 4 and in Appendix A, where the expressions for the absorption constants are explicitly derived.

the quantities n, N_D^+ and J, respectively. First, with (2.1d) we obtain immediately the charge neutrality relationship

$$N_{D0}^+ - n_0 - N_A = 0, \tag{2.8}$$

which shows that any increase of the average electron concentration n_0 in the conduction band is compensated by an equal increase of the number density of ionized donors N_{D0}^+. Usually, for cw laser illumination at a wavelength outside the interband electronic resonance we have always $n_0 \ll N_{D0}^+$ and therefore the average density N_{D0}^+ is not significantly influenced by the illumination. This statement is no longer true for high intensity pulsed laser photoexcitation or for cw illumination in resonance. The spatially averaged quantities give us also an important relationship between the photoconductivity and the illumination strength. The first term on the right-hand side of (2.1c) gives the drift conductivity contribution to the current density, that is $\vec{J}_0 = e\overleftrightarrow{\mu}n_0\vec{E}_0$, the conductivity tensor is therefore given by $\overleftrightarrow{\sigma} = e\overleftrightarrow{\mu}n_0$. The average carrier density n_0 is calculated with (2.1a) to be

$$n_0 = \frac{(\chi w_0 + \beta)\left(N_D - N_{D0}^+\right)}{\gamma N_{D0}^+}, \tag{2.9}$$

therefore the conductivity has a photoconductivity contribution increasing linearly with the average energy density w_0 [3] and a constant dark conductivity contribution ($\propto \beta$).

We concentrate now our interest on the spatially modulated quantities appearing in Eqs. (2.1), and specially on the space-charge field $\vec{E}(\vec{r})$. With the driving quantity given by Eq. (2.5) the set of equations (2.1) can be solved analytically under the assumption that the light modulation index is small ($|m| \ll 1$) as first put forward by Kukhtarev et al. [19] [4]. In this limit, the magnitude of the space-charge electric field $\vec{E}(\vec{r})$ is not strongly influenced by the coupling between the interacting waves. The space-charge field can then be written in a sinusoidal form of the type (2.5), i.e.

$$\vec{E}(\vec{r}) = \vec{E}_0 + \text{Re}\left[\vec{E}_1 \exp\left(i\vec{K}\cdot\vec{r}\right)\right]. \tag{2.10}$$

The calculation of the amplitude $\vec{E}_1$ from the initial equations (2.1) and (2.5) is lengthy but straightforward. Here we give only the final result, first assuming that there are no contributions from photogalvanic currents ($\vec{L}_{pg} = 0$). In this case the steady-state field distribution can be shown to be

$$\vec{E}_1 = \widehat{K}\left[-im\frac{E_q\left(E_D - iE_0\right)}{E_q + E_D - iE_0}\right], \tag{2.11}$$

which can be rewritten as

$$\vec{E}_1 = -m\widehat{K}\left[\frac{E_q^2 E_0}{\left(E_q + E_D\right)^2 + E_0^2} + i\frac{E_q E_D^2 + E_q E_0^2 + E_q^2 E_D}{\left(E_q + E_D\right)^2 + E_0^2}\right]. \tag{2.12}$$

---

[3]By neglecting the fine but sometimes important difference between the 'usefully dissipated energy' w and the light intensity I (see Chapter 5), this statement is equivalent to a a linear increase of photoconductivity with light intensity, as usually referred in literature.

[4]For a general light distribution one has usually to rely on numerical calculations for the solution of Eqs. (2.1). However, besides the small-modulation approximation presented here, in some special situations analytical solutions may be obtained also using a whole-beam method, see for instance Refs. [26–29]. It has to be noticed, that approximated analytical expressions valid for sinusoidal light distributions up to higher order Fourier components, that is outside the small-modulation approximation, have also been obtained [30–33].

In (2.11) and (2.12) $E_0 \equiv \vec{E}_0 \cdot \widehat{K}$ is the projection of the externally applied electric field $\vec{E}_0$ along the direction of the unit vector along the grating $\widehat{K} \equiv \vec{K}/|\vec{K}|$. The scalar quantities E_D and E_q have the dimension of an electric field and are called the diffusion and the trap-limited field, respectively. They are defined as

$$E_D \equiv \frac{|\vec{K}|k_B T}{e} \tag{2.13}$$

and

$$E_q \equiv \frac{e}{\varepsilon_0 \varepsilon_{eff}|\vec{K}|} \frac{N_{D0}^+ \left(N_D - N_{D0}^+\right)}{N_D} \equiv \frac{e}{\varepsilon_0 \varepsilon_{eff}|\vec{K}|} N_{eff}, \tag{2.14}$$

where N_{eff} is an effective trap concentration that becomes maximal if $N_{D0}^+ = N_D/2$, that is if the donor level is in average half-filled in the dark. For the case where no external electric field is applied to the sample ($\vec{E}_0 = 0$) the above Eq. (2.11) simplifies to

$$\vec{E}_1 = -im\widehat{K} \frac{E_q E_D}{E_q + E_D}. \tag{2.15}$$

In this case the driving charge transport mechanisms is solely the diffusion of the photoexcited charge-carriers. As can be easily recognized by using (2.10) and comparing (2.5) with (2.15), in this regime the electric-field grating is shifted by $\pi/2$ with respect to the fringes defined by the rate of photoexcitations.
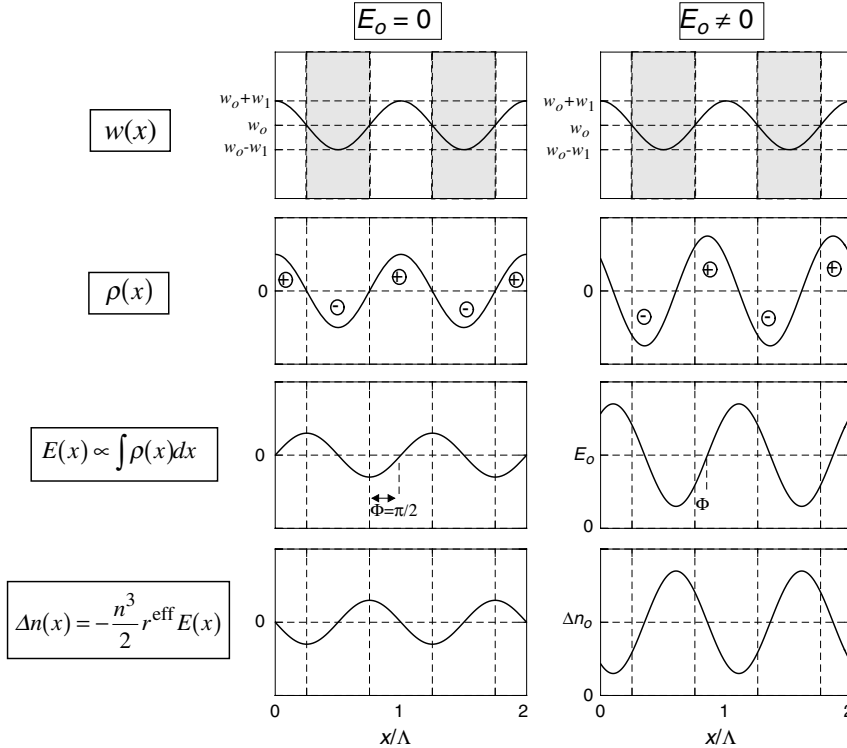
Figure 2.2: Phase relationship between "usefully dissipated energy", space-charge, space-charge field and refractive index distributions. Left hand side: no external field; Right-hand side: with applied electric field.

Figure 2.2 shows schematically the phase relationship between $w(x)$, the total space-charge $\rho(x)$, the space-charge field $E(x)$ and the refractive index change $\triangle n(x)$ for a one-dimensional photorefractive grating pointing along the x-axis. Both diffusion-only

($E_0 = 0$) and drift-assisted cases ($E_0 \neq 0$) are considered. In the latter case the phase shift ϕ between $w(x)$ and $\triangle n(x)$ differs from $\pi/2$ and depends on the magnitude of the applied field E_0 as obtained from

$$\tan \phi = \frac{E_q E_D^2 + E_q E_0^2 + E_q^2 E_D}{E_q^2 E_0}, \tag{2.16}$$

which is derived directly from (2.12). Figure 2.3 shows the in-phase (real part) and

Figure 2.3: Dependence of space-charge field amplitude on grating spacing according to (2.12). a) No applied field; b) With externally applied electric field.
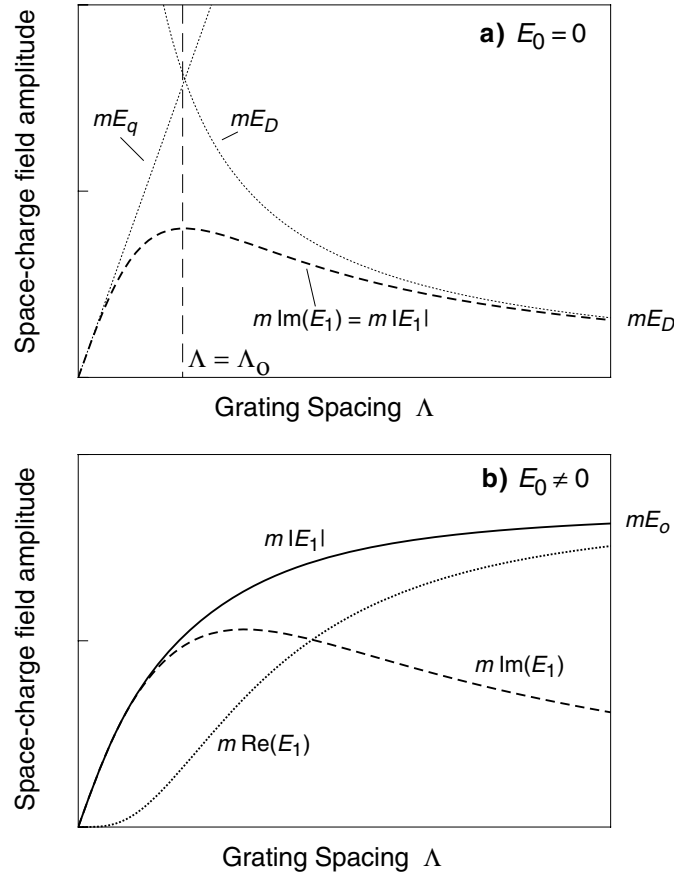
out-of-phase components (imaginary part) of the scalar space-charge field amplitude E_1 inside the square brackets of (2.12) as a function of the grating spacing $\Lambda = 2\pi/|\vec{K}|$, together with the total space-charge field amplitude E_1. At small grating spacings the density of available charges N_{eff} limits the achievable space-charge field amplitude to the value of the field E_q. In absence of applied field the long-grating-spacing space-charge field amplitude diminishes as $E_D \propto 1/\Lambda$ because the charge diffusion mechanisms is less efficient, the longer the grating spacing is. It has to be noted that in absence of an applied field ($E_0 = 0$) the dotted curve (real component) in Fig. 2.3(a) vanishes and the dashed curve for the imaginary component shows a maximum at the Debye grating spacing

$$\Lambda_0 = 2\pi \sqrt{\frac{\varepsilon_0 \varepsilon_{eff} k_B T}{e^2 N_{eff}}}, \tag{2.17}$$

for which $E_q = E_D$. In typical inorganic crystals the Debye grating spacing ranges

between ≈ 0.3 μm and ≈ 1.5 μm. Note also that the dashed curves in Fig. 2.3 can be directly measured by means of two-wave mixing experiments (see Chapt. 5).

For completeness we give now the expressions derived in the steady-state in the presence of photogalvanic effects ($\vec{L}_{pg} \neq 0$) [34–36]. In this case it is important to consider explicitly the electrical boundary conditions. If the crystal surface is fully illuminated, the sample is connected to an external voltage supply (applied electric field $\vec{E}_0$), and dark conductivity is negligible ($\beta \ll \chi w_0$), (2.11) transforms into

$$\vec{E}_1 = \widehat{K} \left[-im \frac{E_q \left[E_D - i \left(E_0 + E_{pv} \right) \right]}{E_q + E_D - i \left(E_0 + \eta E_{pv} \right)} \right], \tag{2.18}$$

where $E_{pv} \equiv \widehat{K} \cdot \vec{E}_{pv}$ is the projection along the grating vector of the photovoltaic field $\vec{E}_{pv}$. The latter corresponds to the equivalent externally applied field that would give rise to a photocurrent equal to the photogalvanic current and is defined by the relationship

$$\overleftrightarrow{\mu} \cdot \vec{E}_{pv} = \gamma N_{D0}^+ \vec{L}_{pg}. \tag{2.19}$$

In Eq. (2.18) η is a factor that takes into account the reduction state of the crystal and is defined as $\eta \equiv N_{D0}^+/N_D$. Note that in many photorefractive materials, such as LiNbO$_3$, LiTaO$_3$ and KNbO$_3$, the longitudinal photogalvanic current is always antiparallel to the spontaneous polarization [23], therefore E_{pv} has opposite sign than an electric field applied along the positive c-axis.

One common experimental situation in strongly photogalvanic crystals such as LiNbO$_3$ and LiTaO$_3$ is the one where the two electrode end-faces are short circuited but no external voltage is applied. In this case Eq. (2.18) is still valid by inserting $E_0 = 0$. In contrast, for an open circuit situation the boundary conditions require a vanishing steady state current density across the sample. This is satisfied if an internal electric field $E_0 = -E_{pv}$ builds up to compensate the photogalvanic current. Therefore from (2.18) the open-circuit steady-state space-charge field is

$$\begin{aligned}
\vec{E}_1 &= \widehat{K} \left[-im \frac{E_q E_D}{E_q + E_D - i E_{pv} \left(\eta - 1 \right)} \right] \\
&= -m\widehat{K} \left[\frac{E_q E_D E_{pv} \left(1 - \eta \right)}{\left(E_q + E_D \right)^2 + E_{pv}^2 \left(\eta - 1 \right)^2} \right. \\
&\quad \left. + i \frac{E_q E_D^2 + E_q^2 E_D}{\left(E_q + E_D \right)^2 + E_{pv}^2 \left(\eta - 1 \right)^2} \right].
\end{aligned} \tag{2.20}$$

Figure 2.4 shows an example of the expected amplitude of the real ($\mathrm{Re}\,(E_1)$) and imaginary component ($\mathrm{Im}\,(E_1)$) of the steady-state space-charge field in the case where the photogalvanic effect is strong. The short circuit configuration usually give rise to stronger fields with a dominating real component that reaches the value of the photovoltaic field at longer grating spacings. In open circuit, in contrast, the field is generally smaller. Note that the imaginary component, which is important for two-wave mixing energy coupling, can show two maxima at two different gratings spacing corresponding to the condition $(E_q + E_D) = |E_{pv}|(1 - \eta)$. Note also that for perfect open circuit boundary conditions the imaginary component can exceed the value of the real one also at longer grating spacing. However, it should be remarked that, due to electrodes effects
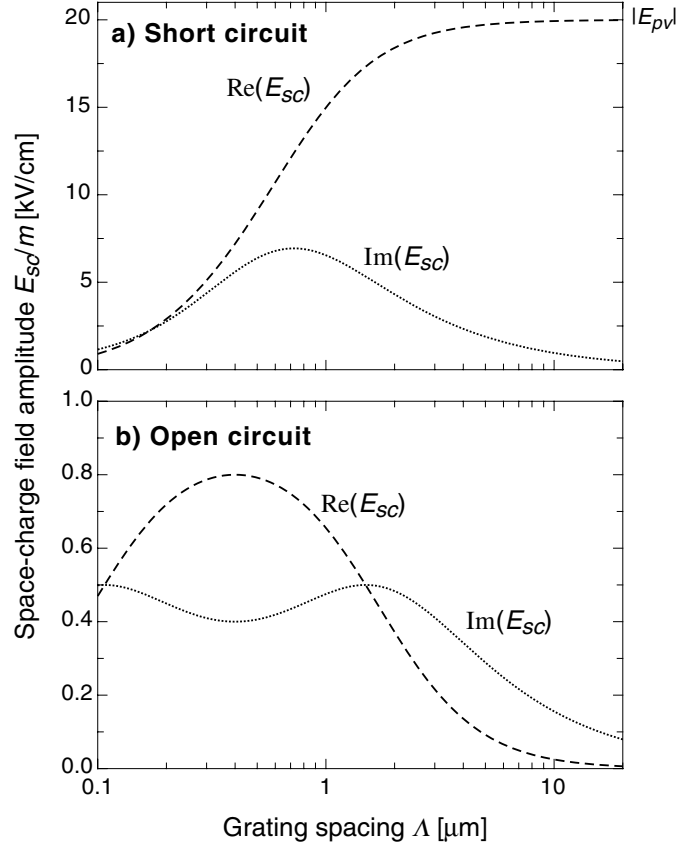
Figure 2.4: Real and imaginary components of the space-charge field amplitude as a function of the grating spacing in the presence of photogalvanic effect. a) Short circuit, (2.18) $E_0 = 0$; b) Open circuit, (2.20). Parameters: $E_{pv} = -20$ kV/cm, $E_D(\Lambda = 1~\mu\text{m}) = 1.6$ kV/cm, $E_q(\Lambda = 1~\mu\text{m}) = 10$ kV/cm, $\eta = 0.2$.

and surface conduction influence, in materials showing strong photogalvanic effects it is not always easy to experimentally define the electrical boundary conditions.

2.1.2 Space-charge field dynamics

The dynamic evolution of the space-charge field amplitude $\vec{E}_1$ upon switching on or switching off the cw periodic illumination (2.5) can be determined from the equation set (2.1). Again, in the small modulation approximation the calculation is lengthy but straightforward[5]. The build-up upon switching on of the illumination at time $t = 0$ evolves exponentially in time as

$$\vec{E}_1(t) = \vec{E}_{1,sat} \left[1 - \exp\left(-\Gamma t\right) \right], \qquad (2.21)$$

while the decay follows

$$\vec{E}_1(t) = \vec{E}_1(t = 0) \exp\left(-\Gamma t\right), \qquad (2.22)$$

which is valid both under homogeneous illumination ($w(\vec{r}) = w_0$), or in the dark. The

---

[5]A detailed derivation of the following expressions (2.21)-(2.24) is not given here. Examples of such a derivation may be found in Refs. [37, 38].

time rate Γ is in general complex, thus allowing for damped oscillations in the dynamics[6]

$$\text{Re}(\Gamma) = \Gamma_{die} \frac{K_e^2(K^2 + K_e^2)\left(1 + \frac{K^2}{K_0^2}\right) + \frac{K_e^2 K^2}{K_0^2}K_D^2}{(K^2 + K_e^2)^2 + K^2 K_D^2}, \tag{2.23}$$

$$\text{Im}(\Gamma) = \Gamma_{die} \frac{K_e^2\left(1 + \frac{K_e^2}{K_0^2}\right)K K_D}{(K^2 + K_e^2)^2 + K^2 K_D^2}. \tag{2.24}$$

These equations are valid in absence of photogalvanic effects, the situation for photogalvanic materials is considerably more complicated and will not be treated here. The reason is that the electrical boundary conditions can change dynamically during the processes of hologram recording and erasure [35]. In (2.23) and (2.24), $K = |\vec{K}|$, $K_0 \equiv 2\pi/\Lambda_0$ is the Debye grating vector,

$$K_e \equiv \sqrt{\frac{e\gamma N_A}{\mu k_B T}} \tag{2.25}$$

is the (scalar) inverse diffusion length in direction $\widehat{K}$, and

$$K_D \equiv \frac{e(\vec{E}_0 \cdot \widehat{K})}{k_B T} \equiv \frac{e E_0}{k_B T} \tag{2.26}$$

is the wavevector for which the applied field equals the diffusion field. Finally, the driving quantity in (2.23) and (2.24) is the dielectric relaxation rate Γ_{die} which is the inverse of the dielectric relaxation time τ_{die} given as

$$\tau_{die} \equiv \frac{1}{\Gamma_{die}} \equiv \frac{\varepsilon_0 \varepsilon_{eff}}{e \mu n_0}, \tag{2.27}$$

where the average electron density n_0 is given by Eq. (2.9). Note that the mobility μ in (2.25) and (2.27) is the scalar mobility for drift in direction of the grating vector, that is

$$\mu \equiv \widehat{K} \cdot \overleftrightarrow{\mu} \cdot \widehat{K}. \tag{2.28}$$

Because of the linear increase of the electron density with w_0 (Eq. (2.9)), the single-carrier band transport model predicts a direct proportionality of both $\text{Re}(\Gamma)$ and $\text{Im}(\Gamma)$ from w_0, and thus usually also from the light intensity. In the absence of applied fields and photogalvanic currents the time rate Γ becomes real and the predicted dynamics is simply exponential. In this case we get

$$\text{Re}(\Gamma) = \Gamma_{die} \frac{1 + \frac{K^2}{K_0^2}}{1 + \frac{K^2}{K_e^2}}, \quad \text{Im}(\Gamma) = 0. \tag{2.29}$$

In general one is mainly interested in the non-oscillating term (real part) of the time rate Γ, Figure 2.5 shows $\text{Re}(\Gamma)$ in absence and in presence of an applied electric field E_0. In the presence of the field, the short grating spacing ($K \to \infty$) limiting time

---

[6]The existence of strong oscillations with low damping constant in the photorefractive dynamics is related with the existence of photorefractive space-charge waves, over which a wide literature exists, see for instance [39–44]. Space-charge waves are observed in photorefractive materials with large drift lengths, such as $Bi_{12}SiO_{20}$ and semiinsulating semiconductors.
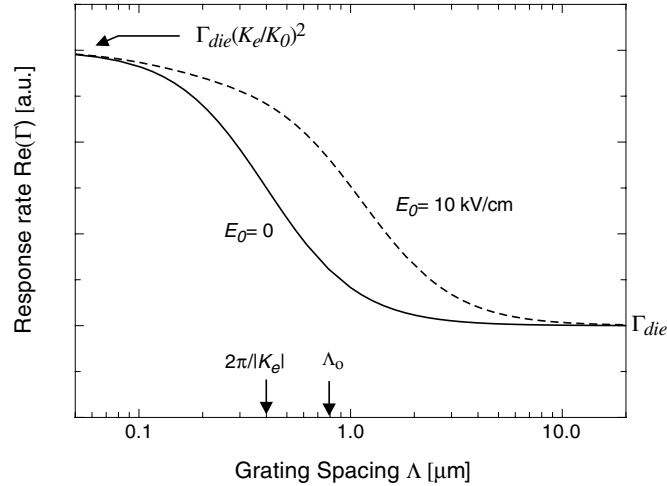
Figure 2.5: Grating spacing dependence of photorefractive response rate
Re(Γ) in absence and presence of an applied electric field.

rate $\text{Re}(\Gamma) = \Gamma_{die}(K_e/K_0)^2 = w_0/(\hbar N_{eff})$ is reached already at longer Λ. Note that in this limit the photorefractive time constant $\tau = 1/\Gamma$ corresponds to the excitation time, that is the time needed to photoexcite a number of charges equal to the effective number of traps N_{eff} [45]. In contrast, at very long grating spacings ($K \ll K_0$, K_e) the photorefractive response rate $\text{Re}(\Gamma)$ always corresponds to the dielectric response rate Γ_{die}.

2.2 Interband photorefractive effects

In this section we present the simplest theoretical model describing the formation of photorefractive gratings by band-to-band photoexcitation. Our interest on this effect rely mainly on the three following interesting properties which are a direct consequence of the physics described below. (a) The short response time due to the efficient photoexcitation process induced by the resonantly absorbed photons. (b) The possibility of obtaining thin gratings which are a prerequisite for several high resolution optical processing elements, such as Joint Fourier Transform Optical Correlators or Incoherent-to-Coherent Converters (see Chapt. 6). (c) The robustness of the induced refractive index changes with respect to below band-gap illumination, which is particularly important for the dynamic waveguide structures created using this effect.

As mentioned above, for interband photorefractive effects the photoexciting light wavelength is in the high absorption spectral region for electronic resonances. Therefore the primary charge transfer mechanism is the phototransition of electrons between the valence and conduction band. Neglecting the effect of mid-gap traps the rate equations (2.1) describing the formation of an internal space-charge field can be reformulated in this case as [46]

$$\frac{\partial n(\vec{r})}{\partial t} = \hbar^{-1}w(\vec{r}) - \gamma_{dir}n(\vec{r})p(\vec{r}) + \frac{1}{e}\vec{\nabla}\cdot\vec{J}_e(\vec{r}) , \qquad (2.30a)$$

$$\frac{\partial p(\vec{r})}{\partial t} = \hbar^{-1}w(\vec{r}) - \gamma_{dir}n(\vec{r})p(\vec{r}) - \frac{1}{e}\vec{\nabla}\cdot\vec{J}_p(\vec{r}), \qquad (2.30b)$$

$$\vec{J}_e(\vec{r}) = en(\vec{r})\overleftrightarrow{\mu}_e\vec{E}(\vec{r}) + k_BT\overleftrightarrow{\mu}_e \cdot \vec{\nabla}n(\vec{r}), \tag{2.30c}$$

$$\vec{J}_p(\vec{r}) = ep(\vec{r})\overleftrightarrow{\mu}_p\vec{E}(\vec{r}) - k_BT\overleftrightarrow{\mu}_p \cdot \vec{\nabla}p(\vec{r}), \tag{2.30d}$$

$$\vec{\nabla} \cdot \vec{E}(\vec{r}) = \frac{e}{\varepsilon_{eff}\varepsilon_0}\left(p(\vec{r}) - n(\vec{r})\right), \tag{2.30e}$$

where all space-dependent variables are also time-dependent. Here p is the hole density in the valence band, $\vec{J}_e$, $\vec{J}_p$, $\overleftrightarrow{\mu}_e$ and $\overleftrightarrow{\mu}_p$ are the electron and hole current densities and mobility tensors, respectively, γ_{dir} is the direct recombination constant between the two bands [7], and the other quantities have been defined previously. As mentioned above, equations (2.30a-2.30e) completely neglect the redistribution of charges within mid-gap traps, which is the dominating effect for conventional photorefraction. This approximation is allowed only in the case where the light intensity (energy density w) are large enough, so that the average densities of free electrons and holes become the same and are given by

$$n_0 = p_0 = \sqrt{\frac{w_0}{\hbar\gamma_{dir}}} \left(= \sqrt{\frac{gI_0}{\gamma_{dir}}}\right). \tag{2.31}$$
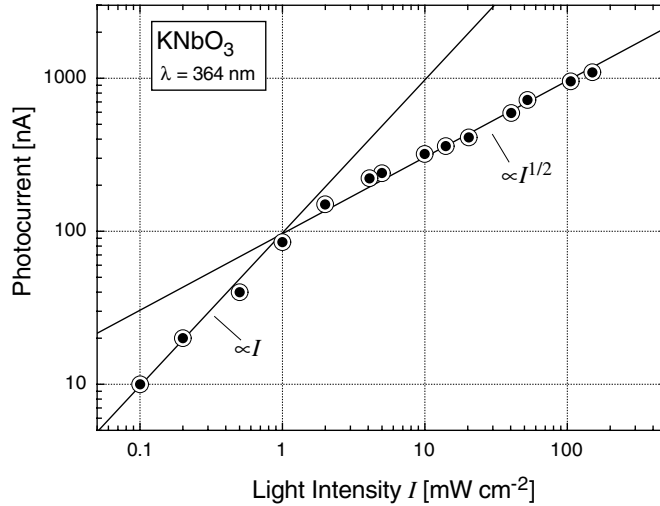

Figure 2.6: Photocurrent as a function of light intensity under interband illumination of $KNbO_3$. In the low intensity regime the photocurrent increases linearly and charge recombination in deep traps plays a major role. In the high intensity regime the photocurrent increases with the square root of light intensity and interband transitions dominate the process.

However, even though experiments involving the interband photorefractive effect are best performed in crystals as pure as possible, we could demonstrate experimentally that deep traps can still play an important role at moderate or low intensities [46–48]. For instance, the presence of deep traps predicts a deviation of the photoconductivity from the square root dependence on light intensity predicted by (2.31), as shown experimentally in Fig. 2.6 [49]. We have presented theoretical models including explicitly the effect of deep traps previously [46–48]. For simplicity, here we keep with equations

---

[7]Neglecting the effect of absorption anisotropy equations (2.30a) and (2.30b) may be written also directly as a function of the light intensity I. In this case the term $\hbar^{-1}w(\vec{r},t)$ is equivalent to $gI(\vec{r},t)$, with $g = \alpha_{dir}/(\hbar k_0 c) = \alpha_{dir}/h\nu$, α_{dir} being the (intensity) absorption constant for the band-to-band transition and $k_0 = 2\pi/\lambda$ being the free space light wavevector.

(2.30a-e) and we present the expected behaviour for this "trap-free" case only, which describes in a satisfactory way the physics of space-charge field formation near the surface illuminated by the highly absorbed recording light.

2.2.1 Steady state

Under a sinusoidal illumination of the type (2.5) the equations (2.30a-2.30e) can be solved in a similar way as in the case of the single carrier band transport model. For the scalar space-charge field amplitude we obtain [46]

$$\vec{E}_1 = \widehat{K} \left\{ -im \frac{[E_D (E_{Rh} - E_{Re}) - iE_0 (E_{Re} + E_{Rh})] E_{qf}}{[(2E_{qf} + E_D)(E_D + E_{Re} + E_{Rh}) + E_0^2] + iE_0 [E_{Re} - E_{Rh}]} \right\}, \quad (2.32)$$

where

$$E_{qf} \equiv \frac{e}{\varepsilon_0 \varepsilon_{eff} |\vec{K}|} n_0 = \frac{e}{\varepsilon_0 \varepsilon_{eff} |\vec{K}|} \sqrt{\frac{w_0}{\hbar \gamma_{dir}}} \quad (2.33)$$

is the free charge limiting field in analogy with (2.14), and

$$E_{Re} \equiv \frac{1}{|\vec{K}| \mu_e} \gamma_{dir} p_0 = \frac{1}{|\vec{K}| \mu_e} \sqrt{\frac{\gamma_{dir} w_0}{\hbar}}, \quad (2.34)$$

$$E_{Rh} \equiv \frac{1}{|\vec{K}| \mu_p} \gamma_{dir} n_0 = \frac{1}{|\vec{K}| \mu_p} \sqrt{\frac{\gamma_{dir} w_0}{\hbar}}, \quad (2.35)$$

are the electron and hole recombination fields, respectively. Their magnitude can be interpreted as the average internal electric fields in which electrons (or holes) drift for an average distance $(K)^{-1} = \Lambda/2\pi$ before a recombination to the other band takes place. The projected mobilities μ_e and μ_p in (2.34) and (2.35) are found according to (2.28).

Figure 2.7 shows the typical dependence of the space-charge field amplitude on grating spacing for the interband case. A comparison with Fig. 2.3(b) shows that the long grating spacing saturation value in presence of an applied field is only half as big with respect to the conventional case. The reason for that is the quadratic recombination process leading to relationship (2.31) for the free charge density, as a consequence the modulation amplitude of the photoexcited charges is only half as big as the one for the energy density $w(\vec{r})$. Another big difference with the conventional photorefraction is the behaviour at small grating spacings Λ. While in the conventional case the space-charge field rises proportional to Λ, in interband photorefraction the initial rise is proportional to Λ^3. This is because not only the free-carrier limiting field E_{qf} is giving a limitation to the space-charge field amplitude, but also the recombination fields E_{Re} and E_{Rh}. The overlinear increase of $\text{Im}(E_1)$ with grating spacing was confirmed experimentally in pure KNbO$_3$ by means of interband two-wave mixing investigations [46, 50]. Figure 2.7(a) also shows that in absence of an external field the space-charge field is bound by the function $(m/2)E_D|(\mu_e - \mu_p)/(\mu_e + \mu_p)|$, therefore, as expected, no space-charge field can build up in this regime if the electron and hole mobilities are the same.

The role of the pseudo-fields E_{qf}, E_{Re} and E_{Rh} merits some additional discussion. A significant space-charge field amplitude can be reached only if E_{qf} and at least one among the recombination fields E_{Re} and E_{Rh} are large enough, say, of the order of 1 kV/cm. Looking at Eq. (2.33) we recognize that the requirement of a large field E_{qf} means nothing else than the charge density n_0 should be large enough to sustain the modulated
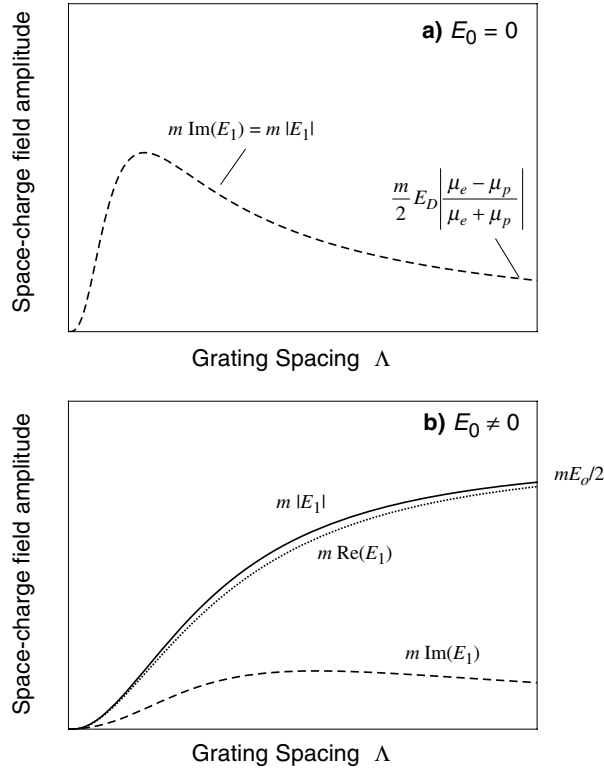
Figure 2.7: Dependence of space-charge field amplitude on grating spacing for interband photorefractive effects in absence of deep traps (2.32). a) No applied field; b) With externally applied field.

space-charge field. The second condition implies that at least one of the carrier mobilities should be small enough so that, before recombination, the carrier is prevented to drift too far as compared to the fringe distance. If the drift or diffusion distances are too long, the carrier looses coherence with the illuminating light distribution and the resulting space-charge field modulation amplitude decreases. In pure $KNbO_3$, the limitations due to E_{qf}, E_{Re} and E_{Rh} normally become important only at grating spacings below ~ 0.5 μm. In general significant space-charge field amplitudes at submicron grating spacing can be easily achieved already for an illuminating intensity of the order of few tens of mW/cm^2 ($\lambda = 364$ nm). For experiments where the typical distances are larger (5-10 μm), such as the dynamic waveguides described in Sect. 6.4, the constraints on E_{qf}, E_{Re} and E_{Rh}, and thus on the illumination intensity, are even less stringent.

2.2.2 Dynamics

The dynamic behaviour of interband photorefractive effects is more complex than the one for the conventional case. In the latter situation, the carriers are photoexcited from mid gap levels and the equilibrium average carrier density in the conduction (or valence) band is reached in a time, which is short as compared to the build-up time of the space-charge field. This is no longer true for interband gratings. The large free carrier density has to build-up first and the time required for this process may be comparable or even longer than the characteristic time constants for the charge redistribution process, such

as the dielectric time τ_{die} (2.27) or the diffusion time $\tau_D \equiv e/(K^2 k_B T\mu)$ for electrons or holes. As discussed in more depth in [46], it is clear that the space-charge field cannot reach a steady-state before the average charge density $n_0(t)$ also does so. Upon switching on the illumination at time $t = 0$, in absence of deep traps the latter grows approximately as

$$n_0(t) = n_0(t = \infty)\frac{1 - \exp(-2\Gamma_{dir}t)}{1 + \exp(-2\Gamma_{dir}t)}, \qquad (2.36)$$

where $n_0(t = \infty)$ is the steady-state value given by (2.31) and

$$\Gamma_{dir} \equiv \gamma_{dir}n_0(t = \infty) = \sqrt{\frac{\gamma_{dir}w_0}{\hbar}} \left(= \sqrt{gI_0\gamma_{dir}}\right) \qquad (2.37)$$

is the recombination rate that governs the charge density build-up. Correspondingly, upon switching off the illumination, the free charge density initially decays in the dark as

$$n_0(t) = n_0(t = 0)\frac{1}{1 + \Gamma_{dir}t}. \qquad (2.38)$$

In pure KNbO$_3$ at wavelengths around 350 nm the time rate Γ_{dir} is typically of the order of $(10\ \mu s)^{-1}$ for illumination intensities of the order of 100 mW/cm^2. As will be shown later, the photorefractive response time in the interband regime is also in the 10-100 μs range, which is faster by at least two order of magnitude with respect to the typical speed of the same material in the conventional photorefractive regime.

Equations (2.36) and (2.38) describe the build-up and decay of the average charge density and therefore do not consider any charge transport issues which are important to describe the formation of the space-charge field. An exact analytical solution of the dynamic equations (2.30a-2.30e) is made difficult by the above time dependence of n_0. Therefore we rely here on a simpler approach that assumes that the build up of the modulated space-charge field starts from a state in which the average free carrier density is already established. In other words, at time $t = 0$ only the modulation m in Eq. (2.5) is being switched on. Following [47] the dynamic solution of the set (2.30a-e) takes the form

$$\vec{E}_1(t) = \vec{E}_{1,sat}\{1 - \frac{1}{2}\left[(1 - B/C)\,e^{-\Gamma_1 t} + (1 + B/C)\,e^{-\Gamma_2 t}\right]\}, \qquad (2.39)$$

where $\vec{E}_{1,sat}$ corresponds to the steady-state solution (2.32) and

$$B \equiv (E_D + E_{qf})(E_{Re} + E_{Rh}) + iE_0(E_{Re} - E_{Rh}) + 2E_{Re}E_{Rh}, \qquad (2.40)$$

$$C \equiv \{[(E_D + E_{qf})(E_{Re} - E_{Rh}) - iE_0(E_{Re} + E_{Rh})]^2 \\ + 4E_{Re}E_{Rh}(E_{qf} - E_{Re})(E_{qf} - E_{Rh})\}^{1/2}. \qquad (2.41)$$

The exponential time rates $\Gamma_{1,2}$ are given by

$$\Gamma_{1,2} = \frac{\Gamma_{dir}}{2E_{Re}E_{Rh}}(B \mp C). \qquad (2.42)$$

In Fig. 2.8 we show the dependence of the time rates Γ_{dir}, Γ_1 and Γ_2 on light intensity. The experimentally observed square root dependence is predicted also theoretically. Note that if Γ_{dir} is smaller than Γ_1 or Γ_2 as in the case shown here, the photorefractive
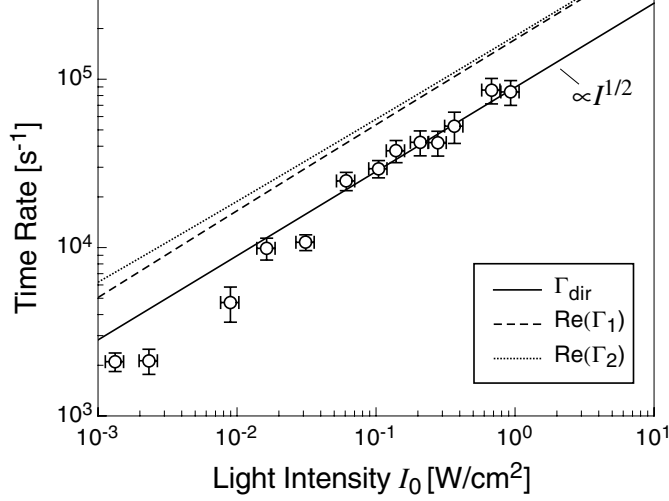
Figure 2.8: Direct recombination rate Γ_{dir} and photorefractive time rates Γ_1 and Γ_2 (2.42) for interband gratings. The points show the measured time rate in pure $KNbO_3$ under illumination at the wavelength $\lambda = 351$ nm and for $\Lambda = 4.7$ μm and $E_0 = 2.2$ kV/cm [46]. The additional parameters for the plot are: $g = 10^{24}$ J^{-1}m^{-1}, $\gamma_{dir} = 8 \cdot 10^{-19}$ m^3/s, $\mu_e = 10^{-9}$ m^2/(Vs).

grating is still expected to build up in a time which is not faster than $(\Gamma_{dir})^{-1}$ because otherwise the average free charge concentration would not have reached a stationary value. It is worth noting that in some limits the time rates Γ_1 and Γ_2 may be expressed in a simpler form. First, for small grating spacings ($\Lambda \rightarrow 0$) the rates Γ_1 and Γ_2 converge towards the diffusion rates $\Gamma_{Dh} \equiv k_B T K^2 \mu_p / e$ and $\Gamma_{De} \equiv k_B T K^2 \mu_e / e$, respectively. On the other hand, for large grating spacings Λ ($E_D \ll E_{qf}$) and for the case where the free charge limiting field is the dominating quantity ($E_{qf} \gg E_{Re}, E_{Rh}$) the expression (2.39) takes the simpler form

$$\vec{E}_1(t) = -im\widehat{K}\frac{E_D}{2}\frac{\mu_p - \mu_e}{\mu_p + \mu_e}\{1 - \exp[-(\Gamma_{die} + \Gamma_{dih})t]\}, \tag{2.43}$$

where $\Gamma_{die} \equiv (e\mu_e n_0 / \varepsilon_0 \varepsilon_{eff}) = (\tau_{die})^{-1}$ is the dielectric rate for electrons and Γ_{dih} is the corresponding dielectric rate for holes. Eq. (2.43) is valid for $E_0 = 0$. Therefore, multiple measurements of the time dynamics in the latter regime allow the determination of the ratio of the effective bipolar mobility μ_p / μ_e along the different crystallographic directions, as performed in [49].

2.3   Other models

In the two sections above we have described in some detail the simplest band models for conventional and interband photorefractive effects, respectively. For the sake of completeness we mention here few other models for conventional photorefractive effects. In particular situations these models describe the space-charge field formation better than the single-level single-carrier band model described in Section 2.1.

2.3.1 Models for electron-hole competition

In several photorefractive materials it is observed that a photon of given wavelength may induce both, photoexcitation and charge transport of electrons in the conduction band, and photoexcitation and charge transport of holes in the valence band. This kind of competition between electrons and holes usually leads to a reduction of the achievable amplitude of the space-charge field grating. The two mostly applied models for electron-hole competition were presented by Valley [51] and Stohkendl [52]. The first model [51, 52] considers a single level from which both electrons and holes can be photoexcited (Fig. 2.9(b)). The second model [51] considers two independent levels, one giving rise to electron charge transport, the other to hole charge transport (Fig. 2.9(c)).
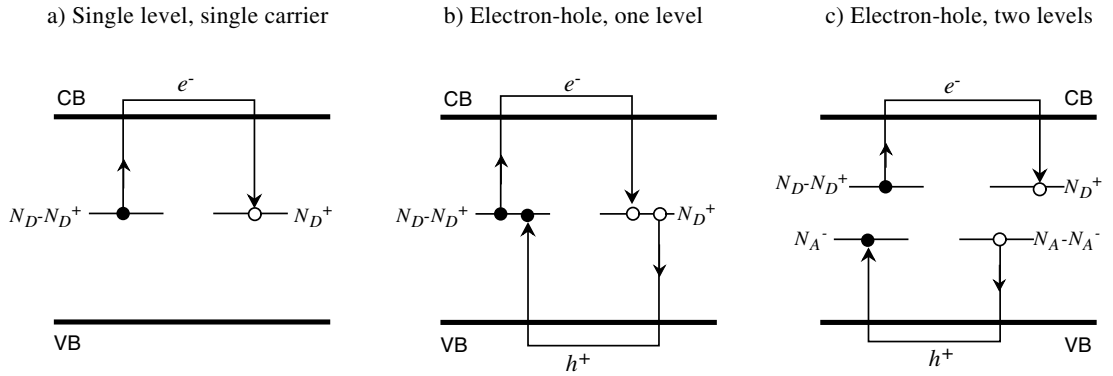

Figure 2.9: Schematics of band models for conventional photorefractive effects. a) Single level, single carrier band model of Sect. 2.1; b) Electron-hole model with single level; c) Electron-hole model with two independent levels.

2.3.1.1 One level

Like in the conventional single level model, in the first electron-hole model there exist a single charge reservoir where the space-charges forming the space-charge field are being trapped. The behaviour is therefore similar to the case of the conventional single-level model, however with some grating-spacing dependent correction terms $R(|\vec{K}|)$ for the space-charge field amplitude [51, 52], so that Eq. (2.15) transforms into

$$\vec{E}_1 = -im\widehat{K}\frac{E_q E_D}{E_q + E_D}R(|\vec{K}|), \tag{2.44}$$

which is given here for the case where no fields are externally applied. The reduction term $R(|\vec{K}|) < 1$ takes the form $R(|\vec{K}|) = (\sigma_e - \sigma_p)/(\sigma_e + \sigma_p)$ at large grating spacings Λ (meaning large in comparison to the electron and hole diffusion lengths). Here $\sigma_e = e\mu_e n_0$ and $\sigma_h = e\mu_h p_0$ are the electron and hole photoconductivities, respectively. On the other hand, for short grating spacings the correction term contains exclusively terms related to the photoexcitation process. Using the same formalism as in Eqs. (2.1) one can write $R(|\vec{K}|) = (w_{e0} - w_{h0})/(w_{e0} + w_{h0})$, where w_{e0} and w_{h0} are the energies absorbed for the generation of mobile electrons and mobile holes, respectively, that is the usefully dissipated energies for electrons and holes defined in accordance with (2.2) and (2.5). Note that since the sign of $(\sigma_e - \sigma_p)$ and $(w_{e0} - w_{h0})$ may differ from each other, a switch in sign of the quantity $\text{Im}(\vec{E}_1)$ may occur at intermediate grating spacings, which

results in a switch of the direction of energy transfer in a two-wave mixing experiment (see Chapter 5). Since it still possesses a unique independent charge reservoire, the dynamics of the first electron-hole model of Fig. 2.9(b) is characterized by a single exponential behaviour as given in (2.21) and (2.22). In analogy with (2.29) the time rate $\Gamma \equiv 1/\tau$ is obtained as

$$\Gamma = \Gamma_{die} \frac{1 + \dfrac{K^2}{K_0^2}}{1 + \dfrac{K^2}{K_e^2}} + \Gamma_{dih} \frac{1 + \dfrac{K^2}{K_0^2}}{1 + \dfrac{K^2}{K_h^2}}, \tag{2.45}$$

where $\Gamma_{dih} \equiv \tau_{dih}^{-1}$ and K_h are the dielectric rate and the inverse diffusion length for holes and are defined equivalently to (2.27) and (2.25).

2.3.1.2 Two levels

The second electron-hole model [51, 53–55] of Fig. 2.9(c) assumes the presence of two independent charge reservoirs. Charge redistribution in the first reservoire occurs uniquely through transport in the conduction band, in the second reservoire uniquely through the valence band. Coupling between the two systems occurs only via the internal space-charge field. This model leads to partial compensation of the space-charge field by formation of two quasi-independent space-charge gratings. In absence of applied fields the two gratings are mutually phase shifted by 180 degrees and the space-charge field amplitude is given as

$$\vec{E}_1 = -im\widehat{K}\frac{E_D\left(E_{qe} - E_{qh}\right)}{E_D + E_{qe} + E_{qh}}, \tag{2.46}$$

where $E_{qh} \equiv (e/\varepsilon\varepsilon_0 K)(N_{A0}^-(N_A - N_{A0}^-)/N_A)$ is the hole trap limited field equivalent to (2.14) and N_{A0}^- is the density of empty hole acceptors in the dark. Note that according to this model, the space-charge field can be completely compensated only if $E_{qe} = E_{qh}$. After compensation, the application of an external electric field can lead to significant transient enhancement of the grating amplitude because drift leads to a phase movement of the two grating components in opposite directions.

One of the most attractive features predicted by this model is the possibility to slow down the dynamics of the process. Due to the presence of the two charge reservoires the grating build-up and decay are given by double exponential functions. In general, one of the involved time constants may become very long even as compared to the dielectric time constant of the slower carriers [8]. Therefore quasi nondestructive readout of the holograms is possible even though the holograms are not permanently fixed. Explicit expressions for the two exponential time rates Γ_1 and Γ_2 were calculated in [61] and [62], in absence of an electric field they read

$$\Gamma_1 = \Gamma_{die} \frac{1 + \dfrac{K^2}{K_{0e}^2}}{1 + \dfrac{K^2}{K_e^2}} + \Gamma_{dih} \frac{1 + \dfrac{K^2}{K_{0h}^2}}{1 + \dfrac{K^2}{K_h^2}}, \tag{2.47}$$

---

[8]This phenomenon is closely related to what can be observed during electret formation in several materials [56–60].

$$\Gamma_2 = \Gamma_{dih} \frac{\Gamma_{die} \left[\frac{K^2}{K_{0h}^2} + \frac{K^2}{K_{0e}^2} \left(1 + \frac{K^2}{K_{0h}^2} \right) \right]}{\Gamma_{die} \left[\left(1 + \frac{K^2}{K_h^2} \right) \left(1 + \frac{K^2}{K_{0e}^2} \right) \right] + \Gamma_{dih} \left[\left(1 + \frac{K^2}{K_e^2} \right) \left(1 + \frac{K^2}{K_{0h}^2} \right) \right]}, \tag{2.48}$$

where $\Gamma_{dih} \equiv \tau_{dih}^{-1}$ and K_h are the dielectric rate and the inverse diffusion length for holes and are defined equivalently to (2.27) and (2.25). $K_{0e} \equiv 2\pi/\Lambda_{0e}$ and $K_{0h} \equiv 2\pi/\Lambda_{0h}$ are the independent Debye screening wave vectors for the two sub-systems and are defined equivalently to (2.17). While the fast time rate Γ_1 essentially behaves like the time rate (2.45) for the first electron-hole model, the time rate Γ_2 reflects the collective motion and the interaction between the electron and hole sub-systems. This can lead to very small values for this time rate and thus to the slow dynamics mentioned above. Specifically, at large grating spacing ($K \to 0$) the time rate evolves as $\Gamma_2 \propto K^2$, that is $\tau_2 = 1/\Gamma_2 \propto \Lambda^2$, which is the same behaviour encountered in the case of grating compensation through ionic charges, as will be discussed in section 2.3.2.

2.3.1.3   Two levels, one with thermal excitation only

If in the above two-level model (Fig. 2.9(c)) one of the levels is considered to be emptied uniquely by thermal transitions the expected steady-state amplitude of the space-charge field differs from the one calculated in (2.46). In this case the thermal excited carriers just try to compensate the field built-up by the photoexcited carriers of the other sign. Therefore, perfect grating compensation does not depend on the delicate equilibrium between the fields E_{qe} and E_{qh} as in (2.46) and the stationary space-charge field takes the form [38]

$$\vec{E}_1 = -im\widehat{K} \frac{E_D E_{qe}}{E_D + E_{qe} + E_{qh}}, \tag{2.49}$$

where it is assumed that electrons are the primary (photoexcited) carriers and m is the modulation of photoexcited free electrons in the conduction band before charge transport. As one can easily see, if E_{qh} and the effective number of hole traps ($N_{A0}^-(N_A - N_{A0}^-)/N_A$) are large, an almost perfect compensation can be obtained. The dynamics is given by the same double exponential behaviour as described by the above electron-hole two level model. The time rates are still given by Eqs. (2.47) and (2.48) where now one of the dielectric time rates does not depend on light intensity. The slowing down of the time rate Γ_2 is observed also here in full analogy with the above case.

2.3.2   Electron-ion compensation, ionic fixing

In the electron-ion model it is assumed that there is single mid-gap level from which a single kind of carrier (for instance electrons) are photoexcited. In addition there is a background of thermal ionic conductivity, the ions move in the field generated by the primary carriers and try to zero the field amplitude. In this respect the electron-ion model is very similar to the latter model above. In absence of applied electric field the steady state space-charge field amplitude after simultaneous electron redistribution and ionic compensation can be calculated as [38, 62, 63]

$$\vec{E}_1 = -im\widehat{K} \frac{E_q E_D \left(E_D - iE_{pv} \right)}{E_q E_D + \left(E_D - i\eta E_{pv} \right) \left(E_{qI} + E_D \right)}, \tag{2.50}$$

where

$$E_{qI} \equiv \frac{e}{\varepsilon_0 \varepsilon_{eff} |\vec{K}|} N_{I0}, \tag{2.51}$$

is the maximum space-charge field that can be induced by the density N_{I0} of ionic charges which are movable and $\eta \equiv N_{D0}^+/N_D$ was already defined in Sect. 2.1.1. For materials with negligible photogalvanic effect ($E_{pv} = 0$) one has then

$$\vec{E}_1 = -im\widehat{K} \frac{E_q E_D}{E_D + E_q + E_{qI}}. \tag{2.52}$$

In materials like LiNbO$_3$ and KNbO$_3$ the density N_{I0} at high temperatures usually exceeds largely the effective trap concentration N_{eff} so that the ratio E_{qI}/E_q is large. In this case Eqs. (2.50) and (2.52) show that the grating is largely compensated and has a very small amplitude at steady state. However, this grating is composed by two large opposite components almost canceling each other. Specially at longer grating spacings the electron and the ion component of the grating may individually reach amplitudes which are larger by orders of magnitude with respect to the electron component (2.15) or (2.18) that would be reached in absence of compensation [38].

Like in the two-level electron-hole model the dynamics is characterized by a double exponential behaviour with the time rates given as

$$\Gamma_1 = \Gamma_{die} \frac{1 + \dfrac{K^2}{K_{0e}^2}}{1 + \dfrac{K^2}{K_e^2}} + \Gamma_{diI} \left(1 + \frac{K^2}{K_{0I}^2} \right), \tag{2.53}$$

$$\Gamma_2 = \Gamma_{diI} \frac{\Gamma_{die} \left[\frac{K^2}{K_{0I}^2} + \frac{K^2}{K_{0e}^2} \left(1 + \frac{K^2}{K_{0I}^2} \right) \right]}{\Gamma_{die} \left(1 + \frac{K^2}{K_{0e}^2} \right) + \Gamma_{diI} \left(1 + \frac{K^2}{K_e^2} \right) \left(1 + \frac{K^2}{K_{0I}^2} \right)}, \tag{2.54}$$

where

$$K_{0I} \equiv \sqrt{\frac{e^2 N_{I0}}{\varepsilon_{eff} \varepsilon_0 k_B T}} \tag{2.55}$$

is the Debye wavevector for ions and $\Gamma_{diI} \equiv e\mu_I N_{I0}/(\varepsilon_{eff}\varepsilon_0)$ is the dielectric relaxation rate for the ions with ionic mobility μ_I. Again, due to the collective motion of electrons and ions the time rate Γ_2 can be made significantly smaller than both leading quantities Γ_{die} and Γ_{diI}, leading to permanent or quasi-permanent holograms. In combination with temperature cycling, ionic compensation is one of the most commonly used techniques for the fixing of photorefractive holograms [64–68]. After high temperature recording and reaching the compensated state the sample may be cooled down to room temperature, where the ionic grating becomes freezed. The final room-temperature grating evolution is related to the time rate Γ_2, however, now with a dielectric relaxation rate Γ_{diI} associated with a much smaller ionic mobility. As a result, in LiNbO$_3$ the fixed gratings may be stable for several years or even decades. Note that in materials with large photogalvanic effects and slow time response of the electronic grating such as LiNbO$_3$ and LiTaO$_3$, a room-temperature revealing of the space-charge grating by means of homogeneous illumination is usually necessary. Several investigations have treated this step in detail [62, 63, 69–72] .

2.3.3   Two-level models, one carrier type

There are several photorefractive materials showing unipolar conductivity where the physics is not fully explained by the simplest one level one carrier model of Sect. 2.1. Not too uncommon phenomena are for instance the observation of double exponential decays or of a sublinear photoconductivity of the type $\sigma_{ph} \propto I^x$, which are not predicted by the simplest model. In this case models invoking the presence of more than one defect level in the band-gap can come to help. The first two-level model was put forward by Valley [73] by considering optically driven transitions only. Several authors have developed the concept further by recognizing that shallow trap centers being thermally coupled to the conduction (or valence) band may contribute to charge transport and lead to the peculiar observations [74–80]. A complete summary of this kind of two-level models has been given recently by Buse [81], distinction between the "two-center model" and the "three-valence model" is made. In the first case the two levels are assumed to be associated with different impurities, each occurring in two valence states. In the second case a single impurity species A that may occur in three different valence states A^+, A^0 and A^- is assumed, leading to the two levels A^+/A^0 and A^0/A^-. The fine difference between the two models lye in the charge neutrality conditions. In the "two-center model" charge neutrality does not need to be satisfied within each impurity type while this is obviously required for the single-impurity "three-valence model". Both models deliver very similar predictions. In absence of applied electric field the space-charge field amplitude is of the form (2.15), however with an additional reduction factor $R(I, \vec{K})$ that depends on light intensity and on the grating wavevector [81]. The limiting field E_q and the effective density of traps N_{eff} are slightly redefined with respect to (2.14) in order to account for the individual model characteristics.

2.4   Summary

In this chapter we have presented the fundamentals of the photorefractive effect. Besides for the conventional single-level single-carrier model, we have described also the simplest model for the formation of the space-charge electric field in response to inter-band absorbed light. In this case the space-charge field amplitude becomes critically dependent on the density of free carriers and therefore on the incident energy. Finally, models valid in specific situations such as simultaneous electron and hole conduction, ionic conduction, or the presence of two active photorefractive defect levels were also discussed shortly. Unlike the common approach, we have taken here the 'usefully dissipated energy' instead of the light intensity as the quantity driving charge redistribution and thus the space-charge field formation. The necessity of this choice will be proven by the experiments presented in Chapt. 5.

Chapter 3

Dielectric response and electro-optic effect

In Chapter 2 the formation of the space-charge electric field was calculated for different physical models starting from the initial rate equations. Through the Gauss equation (2.1d) the space-charge field amplitude will depend on the effective relative dielectric constant ε_{eff}, whose form will be specified below. In addition, we concentrate here our attention to the correct value for the effective linear electro-optic coefficient r_{eff} that translates the modulated internal electric field into a refractive index modulation.

It is well known that the static dielectric tensor and the electro-optic tensor are of anisotropic nature for most of the point group symmetries to whom the major photore-fractive crystals belong. This anisotropy is obvious and, to our knowledge, it is taken into account in all works aimed at optimizing photorefractive geometries. However, as pointed out by several researchers [82–85], the magnitude of the effective dielectric constant and electro-optic coefficient being active in a particular experiment does not depend only on this primary tensor properties. The mechanical state of the crystal plays also a major role. It could be shown that, in general, an electro-optic crystal containing a sinusoidal electric-field grating modulation is neither in a mechanically free, nor in a mechanically totally clamped state. In fact, some of the possible local mechanical re-laxations in response to the periodic electric field are allowed, while other are clamped. As a consequence the magnitude of the dielectric response results from a combination of several contributions involving the piezoelectric effect and the material elasticity. To calculate the electro-optic response also the elasto-optic properties should be added to the picture.

3.1 Mechanical response to modulated electric field

The response of a piezoelectric crystal to external electrical and mechanical fields is given as [86]

$$T_{ij} = C_{ijkl}^{E} S_{kl} - e_{kij} E_k, \tag{3.1}$$

$$D_i = e_{ijk} S_{jk} + \varepsilon_0 \varepsilon_{ij}^{S} E_j. \tag{3.2}$$

Here the Einstein summation convention over equal indices is used, and T_{ij} is the elastic stress tensor, C_{ijkl}^{E} is the elastic stiffness tensor at constant electric field, e_{ijk} is the piezoelectric stress tensor; ε_{ij}^{S} is the clamped static dielectric tensor, E_j is the electric

field vector, D_i is the electric displacement vector, and

$$S_{kl} = \frac{1}{2}\left(\frac{\partial u_k}{\partial x_l} + \frac{\partial u_l}{\partial x_k}\right) \tag{3.3}$$

is the strain tensor corresponding to the symmetrized part of the displacement gradient matrix $\partial u_l/\partial x_k$. The crystal response can be easily calculated in the case of a homogenous field $\vec{E}$. In contrast, as mentioned above, for a photorefractive periodic electric field of the form $\vec{E}(\vec{r}) = E_1\widehat{K}\mathrm{Re}\left[\exp\left(i\vec{K}\cdot\vec{r}\right)\right]$ (2.10) the mechanical response is more complex. In order to determine the effective dielectric constant and electro-optic coefficient it is therefore necessary to calculate the modulated displacement vector field $\vec{u}(\vec{r})$ for this situation. Since the piezoelectric effect is linear, $\vec{u}$ must have the form

$$\vec{u}(\vec{r}) = \vec{u}_1\mathrm{Re}\left[\exp i\left(\vec{K}\cdot\vec{r} - \pi/2\right)\right], \tag{3.4}$$

where the displacement amplitude vector $\vec{u}_1$ in general differs from the direction of the normalized grating vector $\widehat{K} \equiv \vec{K}/|\vec{K}|$ with Cartesian components $\widehat{K}_i$. In steady-state the equation of motion for a crystal volume element leads to the equilibrium condition [86]

$$\frac{\partial T_{ij}}{\partial x_j} = 0 = C_{ijkl}^E \frac{\partial^2 u_{1,k}}{\partial x_j \partial x_l} - e_{kij}\frac{\partial E_{1,k}}{\partial x_j}, \tag{3.5}$$

which can be rewritten as

$$C_{ijkl}^E \widehat{K}_j \widehat{K}_l u_{1,k} = \frac{E_1}{K}e_{kij}\widehat{K}_k\widehat{K}_j, \tag{3.6}$$

or $A_{ik}u_{1,k} = B_i(E_1/K)$, that is

$$u_{1,k} = A_{ki}^{-1}B_i(E_1/K). \tag{3.7}$$

The matrix A_{ik} and the vector B_i are defined as [84],

$$A_{ik} \equiv C_{ijkl}^E \widehat{K}_j\widehat{K}_l, \tag{3.8}$$

$$B_i \equiv e_{kij}\widehat{K}_k\widehat{K}_j. \tag{3.9}$$

Figure 3.1 shows schematically the periodic crystal deformations in the case of a crystal with point group symmetry $4mm$ such as BaTiO$_3$ at room temperature. The partial clamping of some deformation modes leads to the complex displacement field (see for instance case (d)).

3.2   Static dielectric constant

The effective scalar static dielectric constant ε_{eff} which acts in a photorefractive experiment is the quantity connecting the space-charge field amplitude E_1 to the modulation amplitude of the charge density ρ_1 by means of the Gauss equation $\vec{\nabla}\cdot\vec{D} = \rho$ (2.1d). By using this equation, the dielectric relationship (3.2) and the displacement field $\vec{u}$ determined above (3.7), one obtains [84]

$$\varepsilon_{eff} \equiv \frac{\rho_1}{\varepsilon_0 KE_1} = \widehat{K}_i\widehat{K}_j\left[\varepsilon_{ij}^S + \frac{1}{\varepsilon_0}e_{ijk}A_{kl}^{-1}B_l\right]. \tag{3.10}$$
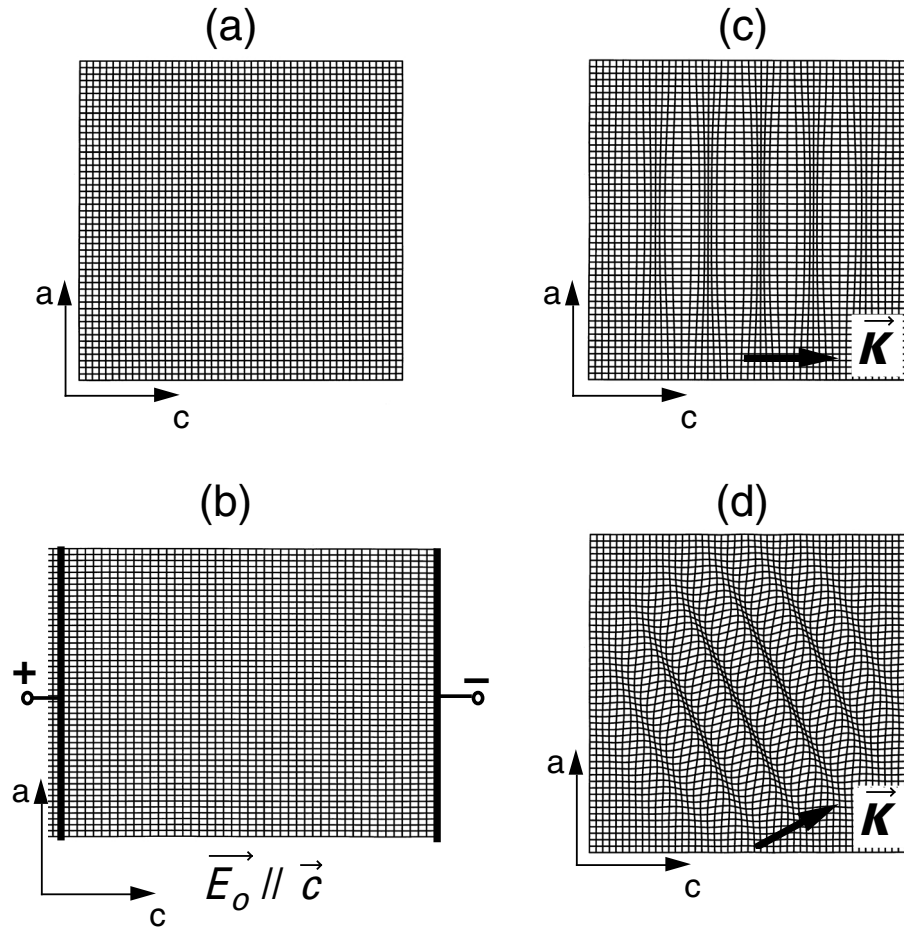
Figure 3.1: Elastic deformations of an ideal crystal belonging to the $4mm$ point group symmetry. (a) undisturbed crystal; (b) homogeneous strain induced by homogeneous electric field along the 4-fold c-axis; (c) periodic dilation/compression under the effect of a periodic space-charge field with grating $\vec{K}$-vector $\parallel$ c-axis. (d) same as (c), but for a $\vec{K}$-vector in the ac plane, the deformations are a combination of dilation/compression and shear deformations. The space-charge field in cases (c) and (d) is assumed to interest only the central part of the crystal. The deformation amplitudes are highly exaggerated.

The quantity in the square bracket represents a new second-rank tensor whose components depend on the direction $\widehat{K}$ of the grating vector. In general, even in the principal system of coordinates of the crystal, this tensor is no longer diagonal. It differs significantly from the unclamped (free) dielectric tensor ε_{ij}^{T} measured at constant stress. The latter can be expressed as [86]

$$\varepsilon_{ij}^{T} = \varepsilon_{ij}^{S} + \frac{1}{\varepsilon_0} e_{ilm} d_{jlm} \tag{3.11}$$

by using (3.2) and the relationship $s_{lm} = d_{jlm} E_j$ for the inverse piezoeffect, with d_{jlm}

being the inverse piezoelectric tensor. Examples visualizing the consequence of equation (3.10) will be given in Sect. 3.4.

3.3 Electro-optic effect

If we consider a homogeneous electric field $\vec{E}(\vec{r}, t) = \vec{E}_0(t)$ the change of the optical indicatrix due to the linear electro-optic effect is given by the well known relationship

$$\Delta \left(\frac{1}{n^2}\right)_{ij} = r_{ijk} E_k, \tag{3.12}$$

where the third-rank electro-optic tensor r_{ijk} depends on the frequency ω of the field. More generally, for a spatially inhomogeneous deformation of the kind resulting in the presence of a periodic space-charge grating (3.4) the change of the indicatrix is expressed as

$$\Delta \left(\frac{1}{n^2}\right)_{ij} = r_{ijk}^S E_k + p_{ijkl}^{'E} \frac{\partial u_k}{\partial x_l}, \tag{3.13}$$

where r_{ijk}^S is the clamped electro-optic tensor that contains the electronic as well as the optical phonon contributions, and $p_{ijkl}^{'E}$ is the modified elasto-optic tensor at constant electric field. The latter tensor contains also the roto-optic contributions and has no symmetry upon interchange of the last two indices [87]. By inserting (3.7) and the space-charge field amplitude $\vec{E}_1 = E_1 \widehat{K}$ in the above equation after a small index rearrangement one obtains

$$\Delta \left(\frac{1}{n^2}\right)_{ij} = E_1 \left[r_{ijk}^S + p_{ijlk}^{'E} A_{lm}^{-1} B_m \right] \widehat{K}_k. \tag{3.14}$$

The expression in the square brackets represents an effective third-rank electro-optic tensor

$$r_{ijk}^{eff} \equiv r_{ijk}^S + p_{ijlk}^{'E} A_{lm}^{-1} B_m \tag{3.15}$$

and differs considerably from the expression

$$r_{ijk}^T \equiv r_{ijk}^S + p_{ijlm}^E d_{klm}^T \tag{3.16}$$

for the unclamped electro-optic tensor r_{ijk}^T calculated in analogy to (3.11) by starting from (3.13) and assuming a homogeneous electric field [1]. Due to the symmetry breaking brought about by the periodic field in direction $\widehat{K}$ and the resulting mechanical response, the tensor r_{ijk}^{eff} may possess a lower symmetry than r_{ijk}^S, which is in full analogy with the above discussion of Eq. (3.10) for the effective dielectric constant. It will be shown in the examples below that the elastic, piezoelectric and elasto-optic contributions contained in the second term on the right-hand side of (3.15) can have a dramatic influence on the photorefractive nonlinearity in several circumstances.

Finally we want to give an expression for the scalar electro-optic coefficient r_{eff} which is active in a specific photorefractive geometry. This scalar coefficient enters the expressions describing light diffraction and two-wave mixing that will be presented in Chapt. 4 and 5. Let us consider a grating directed along the vector $\widehat{K}$ and the interaction of a pump wave P polarized along the unit vector $\widehat{d^P}$ (corresponding to the direction of the optical electric displacement vector) with a signal wave S polarized along $\widehat{d^S}$. The scalar effective electro-optic coefficient is then expressed by

---

[1]In this case the tensor $p_{ijlk}^{'E}$ is replaced by the conventional elasto-optic (Pockels) tensor $p_{ijlk}^E = p_{ijkl}^E$ because for an homogeneous field roto-optic contributions do not lead to a change in refractive index in a free crystal.

$$r_{eff} \equiv \widehat{d_i^S} \left(r_{ijk}^{eff} \widehat{K_k} \right) \widehat{d_j^P}. \tag{3.17}$$

Note that the expression in the brackets is often summarized into an effective (photorefractive) second-rank electro-optic tensor, $r_{ij}^{eff} \equiv r_{ijk}^{eff} \widehat{K_k}$ [88].
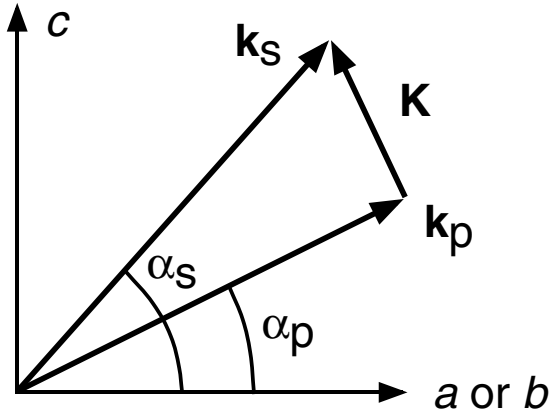

Figure 3.2: Angle convention used for representing the contour plots in this chapter and in Chapt. 5. All angles are in the $ac-$ (BaTiO$_3$) or $bc-$crystal plane (KNbO$_3$) and are internal to the crystal.

3.4   Examples

As it appears evident from Eqs. (3.8)-(3.10) and (3.15) a large number of material constants must be known in order to calculate the active value of ε_{eff} and r_{eff}. For the materials KNbO$_3$ and BaTiO$_3$ the whole set of dielectric, elastic, electro-optic, piezoelectric and elasto-optic constant has been determined [88, 89]. These two ferroelectric crystals are among the most important and best performing photorefractive crystals because they possess large electro-optic coefficients. Therefore we choose KNbO$_3$ and BaTiO$_3$ as examples for visualizing the above expressions [2]. In these two materials the maximum photorefractive nonlinearity is observed for two-beam interaction in the bc-plane (KNbO$_3$), resp. ac-plane (BaTiO$_3$). Therefore we choose a representation allowing us to describe all possible two-wave interaction geometries with the beams propagating in these optimum incidence plane. Let us first specify a convention for the angles of interaction (Figure 3.2). The angles α_S (α_P) are internal to the crystal and represent the angle between the wave-vector $\vec{k}$ of the signal (pump) wave and the crystallographic a-axis (BaTiO$_3$) or b-axis (KNbO$_3$). Since the largest electro-optic coefficients are accessed only for p-polarization of the waves, we consider here only this situation. The case of s-polarization is much less interesting and gives significantly smaller photorefractive coupling constants in the two crystals.

We start first by representing the effective scalar electro-optic coefficient r_{eff}. Figure 3.3 shows a contour plot of this quantity for the bc-plane interaction in KNbO$_3$ as calculated from Eqs.(3.8),(3.9),(3.15) and (3.17). The values are calculated for the wavelength $\lambda = 515$ nm using the material data given in [90]. The thick lines connect points for which the effective electro-optic coefficient vanishes while the positions of the peak values are indicated by triangles. Solid contour lines connect points with a positive value of the represented quantity, while dashed contour lines indicate negative values. The shadowed areas indicate angular regions which, as a result of Snellius law, cannot

---

[2]These materials will be used as examples also in Chapt. 5 where two-wave mixing and its optimization will be treated.
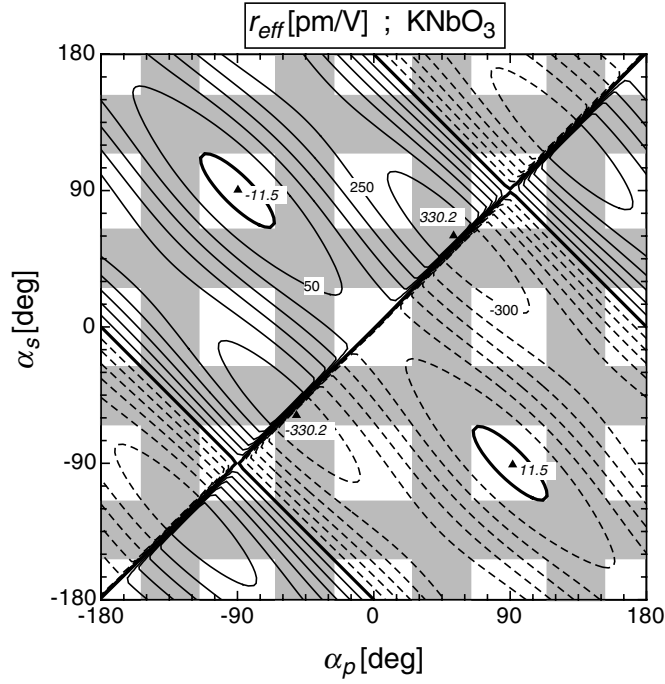
Figure 3.3: Contour plot of the scalar effective electro-optic coefficient r_{eff} (Eq.(3.17)) for each possible two-wave interaction geometry (α_p, α_s) in the bc-plane of KNbO$_3$. Shadowed regions correspond to internal angles which are not accessible from air with a conventional crystal cut along the three crystallographic axes. Contour line distance = 50 pm/V, dashed lines represent negative values and the thick solid line connects points with $r_{eff} = 0$. Triangles denote the position of local or global maxima or minima (italic values).

be directly accessed from air in a crystal with the surfaces cut perpendicular to the crystallographic b- and c-axes. However, these regions may be accessed for other crystal cuts or by using external wedges. For instance, by cutting a crystal sample under 45° with respect to the crystallographic axes the whole shadowed area is accessible.

From Fig. 3.3 it appears evident that a few symmetry operations apply to such a diagram. The first symmetry operation is

- Invariance upon point symmetry on each of the four points $(\alpha_P, \alpha_S) = (-90°, -90°)$, $(90°, -90°)$, $(-90°, 90°)$ or $(90°, 90°)$.

Executing these point symmetry operations corresponds in the laboratory frame to a rotation of the crystal by 180° around the crystallographic c-axis (exchange of b with $-b$), which leaves the effects unchanged. The other symmetry operation is

- Inversion of all values upon point symmetry on the central point $(\alpha_P, \alpha_S) = (0°, 0°)$.

This symmetry operation corresponds to a rotation of the crystal by 180° around the b-axis (a-axis for BaTiO$_3$), i.e. to a switch of the direction of the polar c-axis which reverses the sign of the optical nonlinearity. Note that the inversion with respect to mirroring at the main diagonal seen in Fig.3.3 (exchange of angles between pump and signal wave) is not a general symmetry operation and does not hold for all quantities that will be discussed in this work.

By making use of the symmetries discussed above all redundant information can be eliminated and the size of the diagram of Fig.3.3 can be reduced by a factor of 4. As an
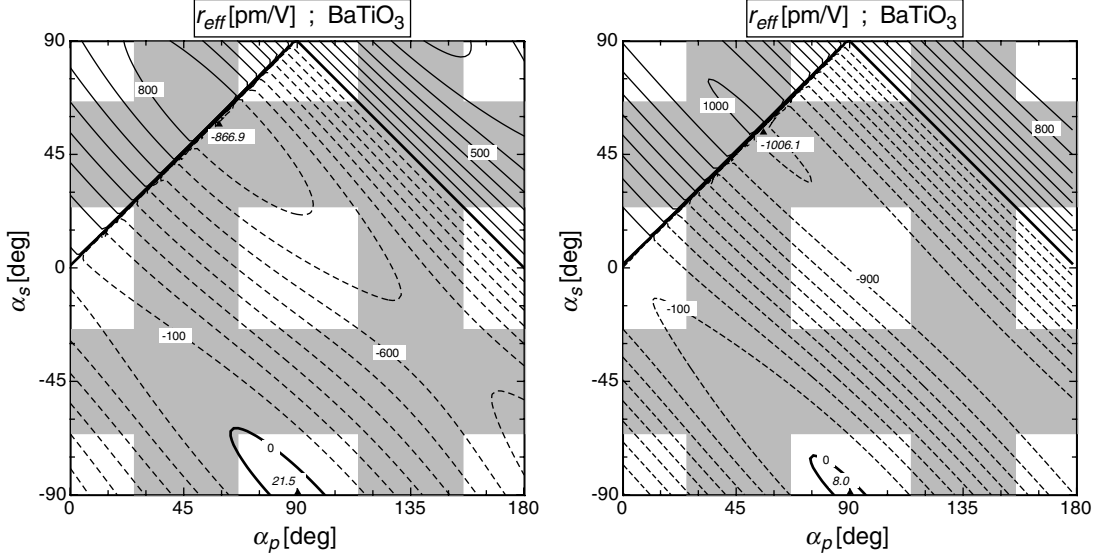
Figure 3.4: Contour plot of the scalar effective electro-optic coefficient r_{eff} [Eq.(3.17)] for each possible two-wave interaction geometry (α_p, α_s) in the ac-plane of BaTiO$_3$. Reduced representation containing all non-redundant information (see text). Contour line distance $= 100$ pm/V. (a) Correct values obtained by considering mechanical coupling according to Eq.(3.15). (b) Incorrect values obtained by using Eq.(3.17) with the unclamped electro-optic tensor r_{ijk}^T.

example, Fig.3.4(a) shows the reduced contour plot diagram for r_{eff}, this time for the ac-plane of BaTiO$_3$. A scalar electro-optic coefficient of the order of 800 pm/V can be accessed even for conventional crystal cuts. In Fig. 3.4 the angles α_p and α_S have been chosen to vary in the intervals $[0°, 180°]$ and $[-90°, 90°]$, respectively. This choice will be maintained for the rest of this work. We may identify some special lines in this kind of representation.

- All conventional geometries for which the grating vector $\overrightarrow{K}$ is parallel to the c-axis are found along the diagonal connecting the points $(90°, -90°)$ and $(0°, 0°)$.

- All geometries with the two beams exactly counterpropagating are found along the diagonal connecting the points $(90°, -90°)$ and $(180°, 0°)$, with the grating vector turning from the c- to the a- (or b-) axis while proceeding along the line.

- Along the diagonal connecting the points $(180°, 0°)$ and $(90°, 90°)$ the grating vector points along the $a(b)-$axis and no electro-optic coupling exists.

- Finally, along the last side diagonal $((0°, 0°)$ to $(90°, 90°))$ the grating vector always vanishes and so does the effective scalar electro-optic coefficient.

Fig.3.4(b) shows the magnitude of r_{eff} if the electro-optic response is incorrectly calculated using the unclamped electro-optic tensor r_{ijk}^T (3.16) to insert in (3.17). As seen by comparison with Fig. 3.4(a), the contour lines shape differ significantly from the case where the mechanical coupling is correctly considered. By using the correct expressions, for most of the geometries the effective electro-optic coefficient is somehow smaller with respect to what would expected on the base of r_{ijk}^T.

In BaTiO$_3$ the discrepancy between r_{ijk}^{eff} and r_{ijk}^T is even stronger if one considers wave interactions outside the ac crystallographic plane. Fig.3.5 shows a photograph of the far field light fanning distribution as observed on the backside of a BaTiO$_3$ crystal
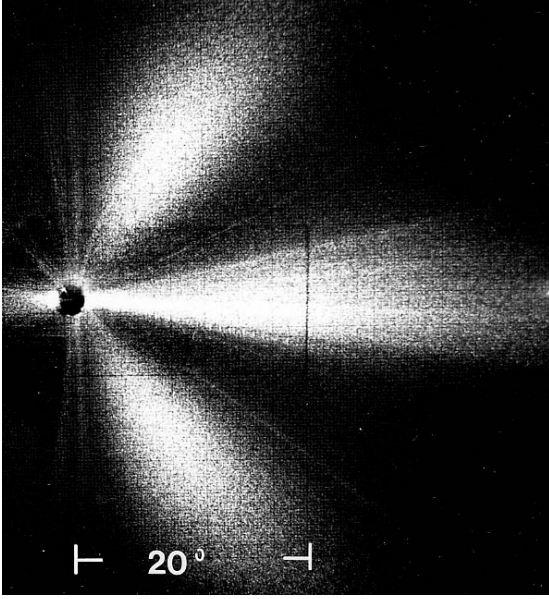
Figure 3.5: Experimentally observed far field distribution of amplified scattered light (fanning) for a pump beam ($\lambda = 514$ nm) propagating along the a-axis of BaTiO$_3$. Both the pump and the fanning have extraordinary polarization. The crystal c axis points to the right. After the crystal the pump beam is blocked by the dark spot in the middle [91].
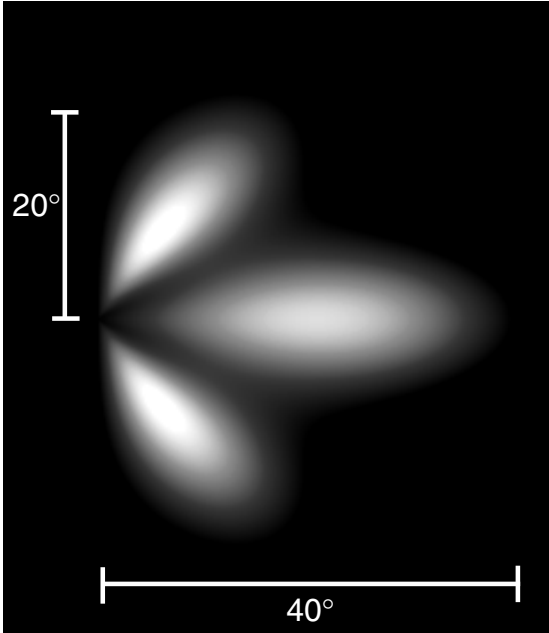

Figure 3.6: Theoretical far-field light fanning distribution induced by an extraordinary polarized wave propagating along the a-axis of BaTiO$_3$. The c-axis points to the right. The angles are outside the crystal and the initial noise is assumed to have a Gaussian distribution in wavevector space with a characteristic divergence of 24°.

illuminated with a single c-polarized laser beam ($\lambda = 514$ nm) propagating parallel to the crystal a-axis. Fanning can be viewed as photorefractively amplified broadband light scattering. Therefore its distribution depends on the symmetry of the electro-optic tensor. The fanning distribution of Fig.3.5 has remained very enigmatic for a long time because the upper and lower fanning lobes cannot be understood on the base of the conventional electro-optic tensor r_{ijk}^T. Only after understanding the details of the mechanical coupling and determination of the tensor r_{ijk}^{eff} the existence of the two additional lobes was explained successfully [91]. Fig. 3.6 shows the expected far field intensity distribution using (3.17) and the wave mixing expressions of Chapt. 5. A Gaussian initial scattering noise distribution is assumed. By using the expression based on r_{ijk}^T only the central horizontal lobe pointing towards the c-axis is expected.

Finally, we visualize the dependence of the effective dielectric constant ε_{eff} on the interaction geometry. As seen in Eq. (3.10) ε_{eff} depends only on the direction of the grating vector $\widehat{K}$, and not on the individual polarization vectors of the two interacting

waves. Therefore, in a diagram such as the one of Fig.3.4, besides for small corrections due to birefringence, the contour lines for ε_{eff} are all essentially parallel to the diagonal going from top-left to bottom-right. Keeping that in mind we choose to plot the values of ε_{eff} in a conventional diagram while we move solely along the main diagonal (from left-bottom to top-right) in Fig.3.4. This is shown in Fig. 3.7 for both crystals under consideration. An extremely strong dependence of the dielectric constant on the interaction geometry as well as the deviation of ε_{eff} from both ε^T and ε^S are evident. Note that for completeness the top axes in Fig.3.7 give also the angular direction θ of the corresponding grating vector $\widehat{K}$ for the two crystals, these axes are slightly nonlinear with respect to the bottom one as a result of the material birefringence.
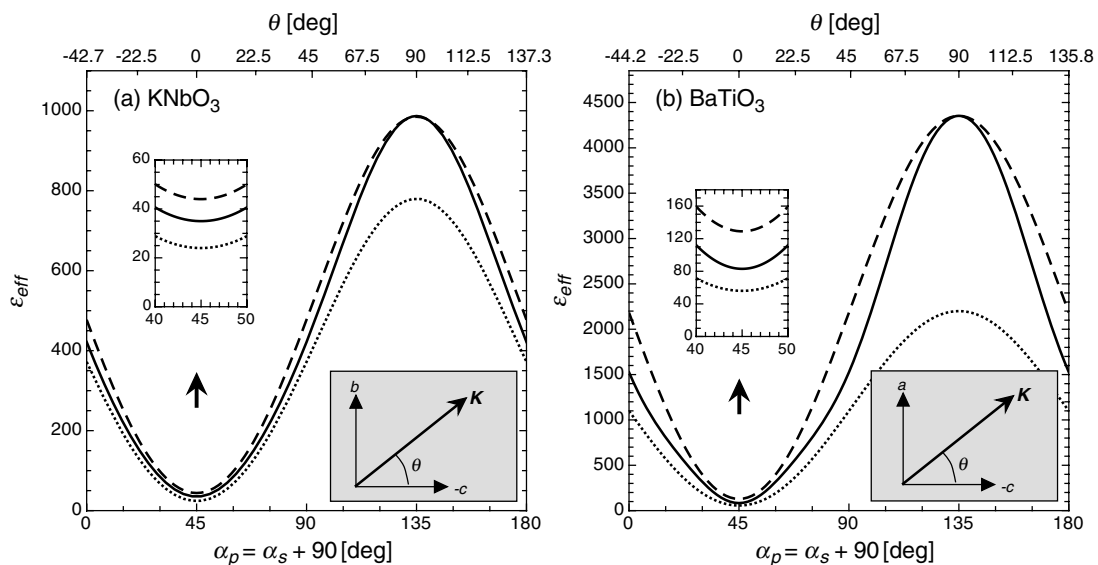

Figure 3.7: Effective dielectric constant ε_{eff} (solid curves, Eq. (3.10) along the main diagonal (bottom-left to top-right) of a diagram such as the one of Fig. 3.4 for KNbO$_3$ (a) and BaTiO$_3$ (b). In comparison, the dashed and dotted curves give the behaviour of $\widehat{K}_i \varepsilon_{ij}^T \widehat{K}_j$ and $\widehat{K}_i \varepsilon_{ij}^S \widehat{K}_j$, respectively. The values of ε_{eff} remain essentially constant by moving away from the main diagonal in normal direction (i.e. $\varepsilon_{eff}(\alpha_p \pm \beta, \alpha_s \mp \beta) \simeq \varepsilon_{eff}(\alpha_p, \alpha_s)$). The top axis shows the grating angle θ defined in the inset.

3.5   Summary

In this chapter we discussed the dielectric response to a modulated charge modulation in a crystal as well as the electro-optic response to the resulting modulated electric field. The expressions for the effective dielectric constant and effective electro-optic coefficient acting in a specific experiment differ from the simple ones found for homogeneous field and homogeneous crystal strain. This is due to the complicated interrelation between piezoelectric effect, crystal elasticity and photoelastic effect which leads to partial crystal clamping in several geometrical arrangements. It was proved that the enigmatic fanning pattern observed in BaTiO$_3$ for a beam propagating perpendicular to the polar axis is a direct consequence of these effects. Special contour plot diagrams facilitating the determination of the optimum two-wave interaction geometry among all possible ones in the plane of maximum photorefractive nonlinearity were introduced in this chapter and will be used extensively also in Chapt. 5.

Chapter 4

Light diffraction at volume gratings in anisotropic media

The modulated photorefractive space-charge electric field discussed in Chapt. 2 leads to a modulated refractive index grating by means of the electro-optic effect discussed in Chapt. 3. If the material is sufficiently thick and the grating modulation is large enough, such a grating can efficiently diffract a light wave provided that its direction satisfies Bragg phase matching. The theoretical efforts to understand light diffraction in thick media have culminated in the coupled wave theory of Kogelnik [12], which applies to isotropic materials. Despite of the fact that a large fraction of the materials used for volume holography are optically anisotropic, only limited effort has been made to theoretically analyze the diffraction of light in this kind of media [92–96]. Kojima [92] analyzed the problem of diffraction of light at phase gratings in absorptionless anisotropic materials finding solutions in the Raman-Nath diffraction regime using a phase function method, and in the Bragg diffraction regime using Born approximation in the undepleted pump limit. Rokushima and Yamakita [93] developed a matrix formalism to solve the same kind of problems and Johnson and Tanguay [94] analyzed phase gratings using a numerical beam propagation method. Glytsis and Gaylord [95] presented a three-dimensional coupled wave diffraction theory for the study of cascaded anisotropic gratings and waveguide geometries. Vachss and Hesselink [96] considered the case of optically active anisotropic photorefractive media. They found solutions for the Bragg diffraction efficiency in the undepleted pump limit. Dielectric and absorption gratings with a common phase and some special crystal cuts were assumed.

The advent of materials with strong birefringence, such as liquid crystals, ordered polymers or organic crystals [97–100] in the field of volume holography asks for a novel consideration of the anisotropy effects. In these materials, not only anisotropic [101] , but also isotropic Bragg diffraction is strongly affected by the optical anisotropy. The main reason lies in the difference between the energy propagation direction and the wavefront normal. Many materials also show an anisotropic absorption constant, that is, absorption depends strongly on the direction of light polarization. A complete analysis of dielectric and absorption gratings in anisotropic materials should include also this effect.

In this chapter we present a complete formalism extending the coupled wave theory of Kogelnik [12] to moderately absorbing non-optically active anisotropic thick media. Dielectric and absorption modulation with common grating vector and of arbitrary relative phase shift is considered. The model is valid in the framework of the slowly varying amplitude approximation for every direction of the grating wavevector in three

dimensions. The entrance and exit surfaces of the medium are parallel to each other and may have an arbitrary orientation with respect to the main axis of the optical indicatrix. We treat the cases of transmission and reflection gratings, the former being characterized by a diffracted beam exiting the medium through the same surface as the transmitted incident beam, the latter being characterized by a diffracted beam back-reflected through the incidence surface. The coupled wave equations are solved for both grating types to give the diffraction efficiency and the angle-mismatch sensitivity. The special case of photorefractive phase gratings is discussed in a separate section.

4.1   Basic equations

Let us consider a medium containing a phase (refractive index) and/or an absorption grating. There are several physical mechanisms being able to generate such gratings, i.e. photochemistry, photorefractive effects, acousto-optics and others. The particular way in which the grating was created is of no importance at this point. Let us consider further the case of thick holograms only. An exact definition of a thick grating has been given by Gaylord and Moharam [102] and the conditions to be fulfilled are

$$Q \equiv \frac{K^2 \lambda d}{2\pi n} > 1 \tag{4.1}$$

and

$$\rho \equiv \frac{\lambda^2}{\Lambda^2 n \sigma} \geq 10, \tag{4.2}$$

where $\sigma = \Delta n$ for dielectric gratings and $\sigma = \Delta\alpha\lambda/2\pi$ for absorption gratings. In our case of anisotropic materials the refractive index change Δn and the absorption modulation $\Delta\alpha$ are defined later in connection with Eqs. (4.47) and (4.51), respectively. The other quantities in the two above conditions are the medium thickness d, the vacuum wavelength λ, the average refractive index n, the grating spacing Λ and the grating wave vector $K = 2\pi/\Lambda$. We notice that if the two conditions above are not strictly fulfilled the diffraction may be described by a mixture of Bragg and Raman-Nath regime. In such an intermediate regime the theory presented in this work gives only approximate results and the diffraction would be calculated more precisely by a rigorous coupled wave analysis similar to the one presented earlier for the isotropic case [103].

As shown by Kogelnik [12], for thick gratings it is sufficient to consider the propagation of only two plane waves P and S. Since we consider the general case of anisotropic materials the waves P and S should represent eigenwaves of the medium. The total electric field amplitude is given by

$$\vec{\mathcal{E}}\left(\vec{r}, t\right) = \left[\vec{E}_s\left(\vec{r}\right) e^{i\vec{k}_s \cdot \vec{r}} + \vec{E}_p\left(\vec{r}\right) e^{i\vec{k}_p \cdot \vec{r}}\right] e^{-i\omega t} + cc. \tag{4.3}$$

where $\vec{E}_s$ and $\vec{E}_p$ are complex amplitudes cleaned of the absorption contribution. This means that they are always constant in absence of nonlinear effects, as explained later. In absorbing crystals the wave vectors $\vec{k}_s$ and $\vec{k}_p$ are complex with the imaginary part which possibly has a different direction than the real part [104]

$$\vec{k}_s = \vec{k}_{s,r} + i\vec{k}_{s,i} \tag{4.4a}$$

$$\vec{k}_p = \vec{k}_{p,r} + i\vec{k}_{p,i}. \tag{4.4b}$$

The real part, as usual, is related to the wavefront propagation direction for an eigen-polarization in the crystal, while the imaginary part is related to the linear absorption experienced by the waves and is calculated as derived in Appendix A. The wave of Eq. (4.3) has to fulfill the time independent vector wave equation

$$\vec{\nabla} \times \left(\vec{\nabla} \times \vec{\mathcal{E}} \right) - k_o^2 \overleftrightarrow{\varepsilon} \cdot \vec{\mathcal{E}} = 0, \tag{4.5}$$

where $\overleftrightarrow{\varepsilon} = \overleftrightarrow{\varepsilon}_r + i \overleftrightarrow{\varepsilon}_i$ is the complex second rank dielectric tensor which includes the effects of the material refractive index and absorption [105], and $k_0 = \omega/c$ is the free space wavenumber. From now on the explicit time dependence $\exp(-i\omega t)$ will be always dropped. We consider a medium containing a phase and/or an amplitude plane holographic grating. The complex dielectric tensor $\overleftrightarrow{\varepsilon}$ can then be expressed as

$$
\begin{aligned}
\overleftrightarrow{\varepsilon} &= \left[\overleftrightarrow{\varepsilon}_r^0 + \overleftrightarrow{\varepsilon}_r^1 \cos \left(\vec{K} \cdot \vec{r} \right) \right] + i \left[\overleftrightarrow{\varepsilon}_i^0 + \overleftrightarrow{\varepsilon}_i^1 \cos \left(\vec{K} \cdot \vec{r} + \phi \right) \right] \\
&= \left[\overleftrightarrow{\varepsilon}_r^0 + \frac{1}{2} \overleftrightarrow{\varepsilon}_r^1 \left(e^{i\vec{K}\cdot\vec{r}} + e^{-i\vec{K}\cdot\vec{r}} \right) \right] \\
&\quad + i \left[\overleftrightarrow{\varepsilon}_i^0 + \frac{1}{2} \overleftrightarrow{\varepsilon}_i^1 \left(e^{i\left(\vec{K}\cdot\vec{r}+\phi\right)} + e^{-i\left(\vec{K}\cdot\vec{r}+\phi\right)} \right) \right]
\end{aligned}
\tag{4.6}
$$

where the superscripts 0 and 1 denote the constant and the amplitude of the modulated component, respectively. The grating vector $\vec{K}$ in Eq. (4.6) is assumed to have an arbitrary direction with respect to the geometrical or crystallographic axis of the anisotropic medium. The absorption grating (modulated term in the imaginary part of Eq. (4.6)) may be phase-shifted by a phase ϕ with respect to the refractive index grating. We may choose our coordinate system to coincide with the main axes of the optical indicatrix so that the tensor $\overleftrightarrow{\varepsilon}_r^0$ contains only diagonal elements. In contrast, the modulated part $\overleftrightarrow{\varepsilon}_r^1$ of the real dielectric tensor is generally nondiagonal. That is

$$
\overleftrightarrow{\varepsilon}_r^0 = \begin{pmatrix} \varepsilon_{r,11}^0 & 0 & 0 \\ 0 & \varepsilon_{r,22}^0 & 0 \\ 0 & 0 & \varepsilon_{r,33}^0 \end{pmatrix}, \tag{4.7}
$$

$$
\overleftrightarrow{\varepsilon}_r^1 = \begin{pmatrix} \varepsilon_{r,11}^1 & \varepsilon_{r,12}^1 & \varepsilon_{r,13}^1 \\ \varepsilon_{r,12}^1 & \varepsilon_{r,22}^1 & \varepsilon_{r,23}^1 \\ \varepsilon_{r,13}^1 & \varepsilon_{r,23}^1 & \varepsilon_{r,33}^1 \end{pmatrix}. \tag{4.8}
$$

For example, nondiagonal elements can be produced by shear acoustic waves and by space-charge induced electro-optic effects. For crystalline materials with orthorhombic or higher symmetry the main axes of the imaginary dielectric tensor coincide with those of the real one [105]. For these materials also $\overleftrightarrow{\varepsilon}_i^0$ and $\overleftrightarrow{\varepsilon}_i^1$ are diagonal tensors,

$$
\overleftrightarrow{\varepsilon}_i^0 = \begin{pmatrix} \varepsilon_{i,11}^0 & 0 & 0 \\ 0 & \varepsilon_{i,22}^0 & 0 \\ 0 & 0 & \varepsilon_{i,33}^0 \end{pmatrix}, \tag{4.9}
$$

$$
\overleftrightarrow{\varepsilon}_i^1 = \begin{pmatrix} \varepsilon_{i,11}^1 & 0 & 0 \\ 0 & \varepsilon_{i,22}^1 & 0 \\ 0 & 0 & \varepsilon_{i,33}^1 \end{pmatrix}. \tag{4.10}
$$

For crystals with lower symmetry the main axes of the absorption ellipsoid may differ from those of the refractive index ellipsoid [106] and the tensors $\overleftrightarrow{\varepsilon}_i^0$ and $\overleftrightarrow{\varepsilon}_i^1$ may contain

also nondiagonal elements in our coordinate system. In the case where only materials with positive absorption (no gain) are considered, there are some additional constraints on the elements of the tensors $\vec{\varepsilon}_i^0$ and $\vec{\varepsilon}_i^1$,

$$\varepsilon_{i,kl}^0 \geq \varepsilon_{i,kl}^1 \geq 0. \tag{4.11}$$

However, in general this assumption is not necessary and the formalism presented here can be used to describe the behaviour in gain media as well, as long as the system remains in a non-oscillating regime.

Let us proceed by analyzing the coupled wave equations by inserting Eqs. (4.6) and (4.3) into the wave equation (4.5). We notice that the first term of Eq. (4.5) can be represented in the following form,

$$\vec{\nabla} \times \left(\vec{\nabla} \times \vec{\mathcal{E}} \right) = e^{i\vec{k}_s \cdot \vec{r}} \left\{ \vec{\nabla} \times \vec{\nabla} \times \vec{E}_s - i \left[\left(\vec{\nabla} \times \vec{E}_s \right) \times \vec{k}_s + \vec{\nabla} \times \left(\vec{E}_s \times \vec{k}_s \right) \right] \right.$$
$$\left. - \left(\vec{E}_s \times \vec{k}_s \right) \times \vec{k}_s \right\} + e^{i\vec{k}_p \cdot \vec{r}} \left\{ \ldots \right\}, \tag{4.12}$$

where we have listed only the terms proportional to $\exp\left[i\vec{k}_s \cdot \vec{r} \right]$ and the second curly bracket contains analogous terms in $\vec{E}_p$ and $\vec{k}_p$. The first term on the right-hand side of Eq. (4.12) contains only second order derivatives of the wave amplitude and can be neglected in the framework of the slowly varying amplitude approximation. The last term together with the second term of Eq. (4.5) that contains the contribution of the non-modulated dielectric tensors describe the linear propagation of the wave as discussed in Appendix A. For the S-wave the equality among the latter described terms reads

$$- \left[\left(\vec{E}_s \times \vec{k}_s \right) \times \vec{k}_s \right] e^{i\vec{k}_s \cdot \vec{r}} = k_o^2 \left[\vec{\varepsilon}_r^0 + i\vec{\varepsilon}_i^0 \right] \cdot \vec{E}_s e^{i\vec{k}_s \cdot \vec{r}}, \tag{4.13}$$

and an analogous expression holds for the P-wave. The remaining terms, the second and third ones on the right-hand side of (4.12), are the most interesting ones. They describe the coupling of the waves due to the modulation expressed by $\vec{\varepsilon}_r^1$ and $\vec{\varepsilon}_i^1$. The
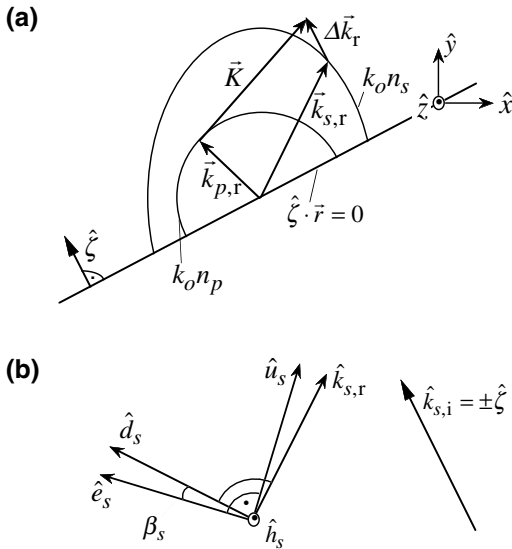

Figure 4.1: (a) Projection of the wavevector diagram for the holographic interaction. The coordinate axes are parallel to the main axes of the optical indicatrix. The input surface plane $\hat{\zeta} \cdot \vec{r} = 0$ does not necessarily contain the axis $\hat{z}$. The vectors $\vec{k}_{s,r}$, $\vec{k}_{p,r}$, $\vec{K}$ and $\Delta\vec{k}_r$ do not need to be all coplanar. (b) Unit vectors in direction of the electric field ($\hat{e}_s$), the dielectric displacement ($\hat{d}_s$), the magnetic field ($\hat{h}_s$), the energy propagation ($\hat{u}_s$), the real and imaginary component of the propagation vector ($\hat{k}_{s,r}$, $\hat{k}_{s,i}$) for the wave S, and the input surface normal ($\hat{\zeta}$). It holds $\hat{e}_s \perp \hat{u}_s \perp \hat{h}_s$, $\hat{d}_s \perp \hat{k}_{s,r} \perp \hat{h}_s$, and $\hat{e}_s \cdot \hat{d}_s = \hat{u}_s \cdot \hat{k}_{s,r} = \cos\beta_s$.

problem being analyzed here is interesting for perfect phase matching and for small

phase mismatch (Figure 4.1(a)). In this case we write the momentum conservation equation as

$$\vec{k}_p + \vec{K} = \vec{k}_s + \Delta\vec{k}$$
$$\Delta\vec{k} \equiv \Delta\vec{k}_r + i\Delta\vec{k}_i = \left(\vec{k}_{p,r} - \vec{k}_{s,r} + \vec{K}\right) + i\left(\vec{k}_{p,i} - \vec{k}_{s,i}\right). \tag{4.14}$$

Using the above arguments Eq. (4.5) transforms in the two coupled wave equations

$$e^{i\vec{k}_s\cdot\vec{r}}\left[\left(\vec{\nabla} \times \vec{E}_s\right) \times \vec{k}_s + \vec{\nabla} \times \left(\vec{E}_s \times \vec{k}_s\right)\right]$$
$$= \frac{k_0^2}{2}\left[i\overleftrightarrow{\varepsilon}_r^1 \cdot \vec{E}_p - \overleftrightarrow{\varepsilon}_i^1 \cdot \vec{E}_p e^{i\phi}\right]e^{i\vec{k}_s\cdot\vec{r}}e^{i\Delta\vec{k}\cdot\vec{r}}, \tag{4.15}$$

and

$$e^{i\vec{k}_p\cdot\vec{r}}\left[\left(\vec{\nabla} \times \vec{E}_p\right) \times \vec{k}_p + \vec{\nabla} \times \left(\vec{E}_p \times \vec{k}_p\right)\right]$$
$$= \frac{k_0^2}{2}\left[i\overleftrightarrow{\varepsilon}_r^1 \cdot \vec{E}_s - \overleftrightarrow{\varepsilon}_i^1 \cdot \vec{E}_s e^{-i\phi}\right]e^{i\vec{k}_p\cdot\vec{r}}e^{-i\Delta\vec{k}\cdot\vec{r}}. \tag{4.16}$$

By using some vector algebra the terms on the left-hand side of Eq. (4.15) can be rewritten as

$$\left(\vec{\nabla} \times \vec{E}_s\right) \times \vec{k}_s = \left|\vec{k}_{s,r}\right|\left\{\left(\hat{k}_{s,r} \cdot \frac{\partial E_s}{\partial\vec{r}}\right)\hat{e}_s - \left(\hat{e}_s \cdot \hat{k}_{s,r}\right)\frac{\partial E_s}{\partial\vec{r}}\right\}$$
$$+ i\left|\vec{k}_{s,i}\right|\left\{\left(\hat{k}_{s,i} \cdot \frac{\partial E_s}{\partial\vec{r}}\right)\hat{e}_s - \left(\hat{e}_s \cdot \hat{k}_{s,i}\right)\frac{\partial E_s}{\partial\vec{r}}\right\}, \tag{4.17}$$

and

$$\vec{\nabla} \times \left(\vec{E}_s \times \vec{k}_s\right) = \left|\vec{k}_{s,r}\right|\left\{\left(\hat{k}_{s,r} \cdot \frac{\partial E_s}{\partial\vec{r}}\right)\hat{e}_s - \left(\hat{e}_s \cdot \frac{\partial E_s}{\partial\vec{r}}\right)\hat{k}_{s,r}\right\}$$
$$+ i\left|\vec{k}_{s,i}\right|\left\{\left(\hat{k}_{s,i} \cdot \frac{\partial E_s}{\partial\vec{r}}\right)\hat{e}_s - \left(\hat{e}_s \cdot \frac{\partial E_s}{\partial\vec{r}}\right)\hat{k}_{s,i}\right\}, \tag{4.18}$$

where the complex scalar amplitude E_s is defined by

$$\vec{E}_s = E_s\hat{e}_s \tag{4.19}$$

and $\hat{e}_s$, $\hat{k}_{s,r}$ and $\hat{k}_{s,i}$ are real unit vectors directed along the electric field vector and the real and imaginary wavevectors of the wave S, as shown in Figure 4.1(b). $\partial E_s/\partial\vec{r} \equiv \vec{\nabla}E_s$ is the gradient of the scalar complex wave amplitude E_s. Similar expressions to (4.17) and (4.18) hold for the wave P and the left-hand side of Eq. (4.16).

In the present treatment we consider only waves which are sufficiently far from the absorption resonance of the medium. In this limit one has only moderate absorption, that is $\left|\vec{k}_{s,i}\right| \ll \left|\vec{k}_{s,r}\right|$ and $\left|\vec{k}_{p,i}\right| \ll \left|\vec{k}_{p,r}\right|$. We can therefore neglect the terms involving $\left|\vec{k}_{s,i}\right|$ in Eqs. (4.17) and (4.18). All relationships derived in this work are valid in this limit. Summing (4.17) and (4.18) and multiplying both sides of Eq. (4.15) with the unit vector $\hat{e}_s$ one obtains

$$2\left|\vec{k}_{s,r}\right|\left\{\frac{\partial E_s}{\partial\vec{r}} \cdot \left[\hat{k}_{s,r} - \hat{e}_s\left(\hat{e}_s \cdot \hat{k}_{s,r}\right)\right]\right\}$$
$$= \frac{k_0^2}{2}\left[i\,\hat{e}_s \cdot \overleftrightarrow{\varepsilon}_r^1 \cdot \hat{e}_p - \hat{e}_s \cdot \overleftrightarrow{\varepsilon}_i^1 \cdot \hat{e}_p e^{i\phi}\right]E_p e^{i\Delta\vec{k}\cdot\vec{r}}, \tag{4.20}$$

where the transpose sign has been omitted in all terms of the kind $\hat{e}_s^T \cdot \overleftrightarrow{\varepsilon}_r^1 \cdot \hat{e}_p$ in order to simplify the notation. The left-hand side vector expression in the square brackets gives a vector which is parallel to the energy propagation direction (Poynting vector) of the wave S [105]. One can write

$$\hat{k}_{s,r} - \hat{e}_s \left(\hat{e}_s \cdot \hat{k}_{s,r} \right) = g_s \hat{u}_s \tag{4.21}$$

with $\hat{u}_s$ being the unit vector along the Poynting vector (Figure 4.1 (b)). The proportionality constant g_s can be determined by making use of the crystal optic wave propagation properties, that is $\hat{k}_{s,r} \cdot \hat{u}_s = \hat{e}_s \cdot \hat{d}_s = \cos \beta_s$ and $\hat{k}_{s,r} \cdot \hat{d}_s = \hat{e}_s \cdot \hat{u}_s = 0$, which leads to

$$g_s = \hat{e}_s \cdot \hat{d}_s = \cos \beta_s. \tag{4.22}$$

The unit vector $\hat{d}_s$ points in the direction of the electric displacement vector for the wave S. By introducing the unperturbed refractive indices n_s and n_p seen by the signal and pump wave respectively, and with $\left| \vec{k}_{s,r} \right| = k_0 \, n_s$ and $\left| \vec{k}_{p,r} \right| = k_0 \, n_p$, the coupled wave equations (4.15) and (4.16) are rewritten as

$$\frac{\partial E_s}{\partial \vec{r}} \cdot \hat{u}_s = \frac{k_0}{4 n_s g_s} \left[i \, \hat{e}_s \cdot \overleftrightarrow{\varepsilon}_r^1 \cdot \hat{e}_p - \hat{e}_s \cdot \overleftrightarrow{\varepsilon}_i^1 \cdot \hat{e}_p e^{i\phi} \right] E_p e^{i\Delta \vec{k} \cdot \vec{r}}, \tag{4.23a}$$

$$\frac{\partial E_p}{\partial \vec{r}} \cdot \hat{u}_p = \frac{k_0}{4 n_p g_p} \left[i \, \hat{e}_p \cdot \overleftrightarrow{\varepsilon}_r^1 \cdot \hat{e}_s - \hat{e}_p \cdot \overleftrightarrow{\varepsilon}_i^1 \cdot \hat{e}_s e^{-i\phi} \right] E_s e^{-i\Delta \vec{k} \cdot \vec{r}}, \tag{4.23b}$$

where $g_p = \hat{e}_p \cdot \hat{d}_p$ in analogy to (4.22). Equations (4.23a) and (4.23b) describe the coupling of two plane waves in any general geometry in anisotropic media containing phase and/or absorption gratings. It is important to notice that the coupling terms must describe the projection of the amplitude gradients along the Poynting vector direction $\hat{u}$ of the corresponding wave. The original theory of Kogelnik [12], in contrast, contains projections along the wavevector direction $\hat{k}$, which is correct for the isotropic materials treated in Kogelnik's model, but is incorrect if applied to the more general case of optically anisotropic materials.

Given the geometry of a medium containing a phase and/or absorption grating and the waves boundary conditions, Eqs. (4.23a) and (4.23b) can be used as the base for the determination of the diffraction properties. For finite media with a general form one has often to rely on numerical integration. Fortunately, in the most common case of a medium with two parallel surfaces, if one assumes an infinite lateral extent the diffraction properties can be obtained analytically. Depending on the grating orientation one can then distinguish between two main grating types, i.e. transmission and reflection type gratings, as depicted in Figure 4.2. In the former case incident and diffracted wave exit the medium through the same surface, in the latter case the two waves leave the sample through opposite surfaces [1]. In the following we derive the analytic expressions describing diffraction at transmission and reflection gratings in a plate with parallel surfaces of infinite extent.

---

[1]Note that it is possible for a given grating being fixed in a medium to assume transmission character for certain read-out wavelengths and reflection character for others.
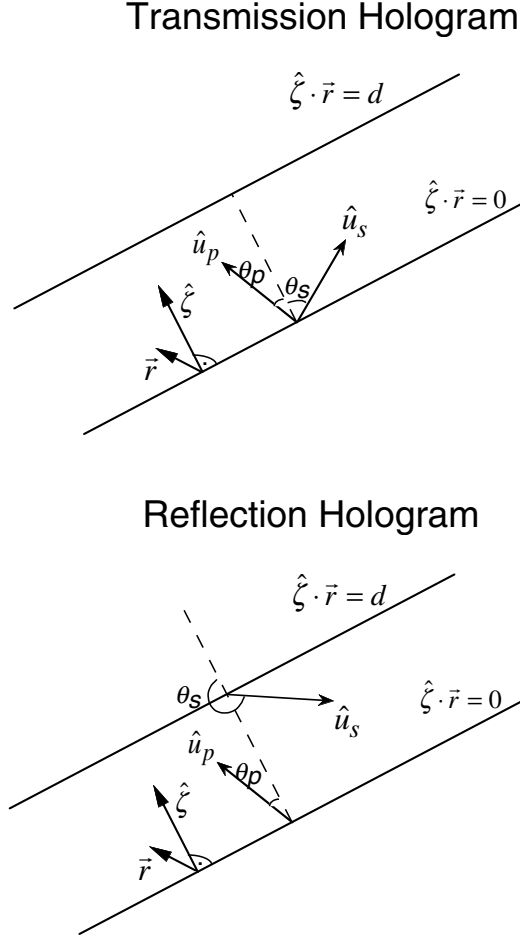
Transmission Hologram

Reflection Hologram

Figure 4.2: Wave propagation directions for transmission and reflection holograms.

4.2 Transmission gratings

4.2.1 Mixed transmission gratings

Let us consider first transmission gratings, as mentioned above in this case both beams S and P leave the material through the same surface. More precisely, this geometry is characterized mathematically by the condition $\left(\hat{u}_p \cdot \hat{\zeta}\right)\left(\hat{u}_s \cdot \hat{\zeta}\right) \equiv \cos\theta_p \cos\theta_s > 0$, where $\hat{\zeta}$ is the unit vector in the direction of the normal to the entrance surface of the wave P in the holographic medium (Figure 4.2).

We look for a general expression for the holographic diffraction efficiency under pump depletion conditions. To find the spatial evolution of the signal wave S we extract E_p from Eq. (4.23a) and insert it into Eq. (4.23b) to get the second order differential equation

$$\left(\frac{\partial^2 E_s}{\partial \vec{r}^2} \cdot \hat{u}_s\right) \cdot \hat{u}_p - i\left(\frac{\partial E_s}{\partial \vec{r}} \cdot \hat{u}_s\right)\left(\Delta\vec{k} \cdot \hat{u}_p\right)$$

$$+\frac{k_0^2}{16 n_s n_p g_s g_p} E_s\left[A_r^2 - A_i^2 + 2i A_r A_i \cos\phi\right] = 0, \tag{4.24}$$

where $\partial^2/\partial\vec{r}^2 \equiv \vec{\nabla} \otimes \vec{\nabla}$ and $\otimes$ indicates outer product. The coupling constants A_r and A_i are defined as

$$A_r \equiv \hat{e}_s \cdot \ddot{\vec{\varepsilon}}_r^1 \cdot \hat{e}_p = \hat{e}_p \cdot \ddot{\vec{\varepsilon}}_r^1 \cdot \hat{e}_s, \tag{4.25}$$

$$A_i \equiv \hat{e}_s \cdot \ddot{\vec{\varepsilon}}_i^1 \cdot \hat{e}_p = \hat{e}_p \cdot \ddot{\vec{\varepsilon}}_i^1 \cdot \hat{e}_s, \tag{4.26}$$

where the second equalities are valid because the tensors $\ddot{\vec{\varepsilon}}_r^1$ and $\ddot{\vec{\varepsilon}}_i^1$ are symmetric. The boundary conditions for diffraction from a transmission grating are

$$E_s\left(\hat{\zeta} \cdot \vec{r} = 0\right) = 0 \tag{4.27}$$

and

$$\frac{\partial E_s}{\partial \vec{r}} \cdot \hat{u}_s \left(\hat{\zeta} \cdot \vec{r} = 0\right) = \frac{k_0}{4 n_s g_s}\left[i\, A_r - A_i e^{i\phi}\right] E_{p0} e^{i\Delta\vec{k}\cdot\vec{r}}, \tag{4.28}$$

where $E_{p0} = E_p\left(\hat{\zeta} \cdot \vec{r} = 0\right)$ is the pump wave amplitude at the entrance face of the anisotropic holographic medium. The general solution of the differential equation (4.24) has the form

$$E_s = E_{s1}\exp\left(\vec{\gamma}_1 \cdot \vec{r}\right) + E_{s2}\exp\left(\vec{\gamma}_2 \cdot \vec{r}\right), \tag{4.29}$$

where E_{s1} and E_{s2} are complex constants. The direction of the vectors $\vec{\gamma}_1$ and $\vec{\gamma}_2$ is not strictly defined because by inserting Eq. (4.29) into Eq. (4.24) one obtains constraints only on the scalar products $\vec{\gamma} \cdot \hat{u}_s$ and $\vec{\gamma} \cdot \hat{u}_p$. In view of the boundary conditions given by Eqs. (4.27) and (4.28) it is useful to choose $\vec{\gamma}_1$ and $\vec{\gamma}_2$ parallel to the surface normal $\hat{\zeta}$, which gives

$$\vec{\gamma}_{1,2} = \left(i\frac{\Delta\vec{k} \cdot \hat{u}_p}{2\cos\theta_p} \pm iW\right)\hat{\zeta}, \tag{4.30}$$

where $W = \sqrt{W^2}$ is a complex quantity with

$$W^2 = \left(\frac{\Delta\vec{k} \cdot \hat{u}_p}{2\cos\theta_p}\right)^2 + \frac{k_o^2}{16 n_s n_p g_s g_p \cos\theta_s \cos\theta_p}$$
$$\times \left(A_r^2 - A_i^2 + 2i A_r A_i \cos\phi\right) \tag{4.31}$$

and

$$\cos\theta_s = \hat{\zeta} \cdot \hat{u}_s, \quad \cos\theta_p = \hat{\zeta} \cdot \hat{u}_p. \tag{4.32}$$

It is important to note that all projection cosines in Eq. (4.31) are taken with respect to the Poynting vector direction and not with respect to the wavevector direction. The constants E_{s1} and E_{s2} are obtained by using the boundary conditions (4.27) and (4.28) and one finds

$$E_{s1} = -E_{s2} = \frac{k_0}{8 n_s g_s \cos\theta_s} e^{i\Delta\vec{k}\cdot\vec{r}_\parallel} \frac{A_r + i A_i e^{i\phi}}{W} E_{p0}, \tag{4.33}$$

where $\vec{r}_\parallel$ is a position vector on the entrance surface defined by $\hat{\zeta}\cdot\vec{r} = 0$. The constant E_{s1} is $\vec{r}$-independent and the general solution (4.29) fulfills the differential equation (4.24) only if $\Delta\vec{k}\cdot\vec{r}_\parallel = 0$ for all $\vec{r}_\parallel$, thus constraining the real and imaginary part of the vector $\Delta\vec{k}$ to be parallel to the normal to the surface $\hat{\zeta}$, as shown in Fig. 4.1(a). This property

is a direct consequence of the fact that waves and gratings have infinite extent in the transversal directions. The wavefront propagation direction $\vec{k}_s$ of the wave S is now well defined and is obtained using (4.14) and the linear crystal-optic properties of the sample. By inserting the complex amplitudes (4.33) and the complex gain constants (4.30) into (4.29) one finds the general solution for the evolution of the signal wave amplitude

$$E_s\left(\vec{r}\right) = \frac{k_0}{8n_sg_s\cos\theta_s}\frac{A_r + iA_ie^{i\phi}}{W}\,e^{i\left(\frac{\Delta k_r + i\Delta k_i}{2}\right)\hat{\zeta}\cdot\vec{r}}$$
$$\times\left[e^{iW\left(\hat{\zeta}\cdot\vec{r}\right)} - e^{-iW\left(\hat{\zeta}\cdot\vec{r}\right)}\right]E_{p0}, \tag{4.34}$$

where the real scalar mismatch quantities Δk_r and Δk_i have been defined by $\Delta\vec{k}_r = \Delta k_r\hat{\zeta}$ and $\Delta\vec{k}_i = \Delta k_i\hat{\zeta}$. In analogy, one can also find the wave amplitude of the transmitted pump wave, which is

$$E_p\left(\vec{r}\right) = e^{-i\left(\frac{\Delta k_r + i\Delta k_i}{2}\right)\hat{\zeta}\cdot\vec{r}}\left[\frac{2W + (\Delta k_r + i\Delta k_i)}{4W}e^{iW\left(\hat{\zeta}\cdot\vec{r}\right)}\right.$$
$$\left. + \frac{2W - (\Delta k_r + i\Delta k_i)}{4W}e^{-iW\left(\hat{\zeta}\cdot\vec{r}\right)}\right]E_{p0}. \tag{4.35}$$

One can now calculate the diffraction efficiency defined as the ratio of the output signal intensity to the incident pump intensity

$$\eta \equiv \frac{I_s\left(\hat{\zeta}\cdot\vec{r}=d\right)}{I_p\left(\hat{\zeta}\cdot\vec{r}=0\right)} = \frac{E_sE_s^*n_sg_s}{E_{p0}E_{p0}^*n_pg_p}\frac{\cos\theta_s}{\cos\theta_p}e^{-2\vec{k}_{s,i}\cdot\vec{r}}. \tag{4.36}$$

The factor $\cos\theta_s/\cos\theta_p$ is an obliquity term which assures consistent results in a general case when we are interested in the optical energy flow through the input and output surfaces of the medium. The existence of the term n_sg_s/n_pg_p has been often overlooked in the literature. Neglecting this term is allowed only in isotropic materials or in anisotropic materials in the case of a configuration fully symmetric with respect to the axis $\hat{\zeta}$ and the optical indicatrix. By using the definition for the diffraction efficiency (4.36) and the solution for the evolution of the signal wave amplitude (4.34) one obtains the general expression for the diffraction efficiency of a mixed transmission grating

$$\eta\left(\hat{\zeta}\cdot\vec{r}=d\right) = \frac{k_0^2}{16n_sn_pg_sg_p\cos\theta_s\cos\theta_p}\frac{A_r^2 + A_i^2 - 2A_rA_i\sin\phi}{|W^2|}$$
$$\times\left\{\sin^2\left(\text{Re}\left[W\right]d\right) + \sinh^2\left(\text{Im}\left[W\right]d\right)\right\}e^{-(\alpha_s+\alpha_p)d}. \tag{4.37}$$

The quantities $\alpha_s = |\vec{k}_{s,i}|$ and $\alpha_p = |\vec{k}_{p,i}|$ are the effective amplitude absorption constants experienced by the signal wave S and pump wave P in direction of the surface normal $\hat{\zeta}$, respectively. They are expressed by

$$\alpha_s = \frac{k_0\left(\hat{e}_s\cdot\vec{\varepsilon}_i^0\cdot\hat{e}_s\right)}{2n_sg_s\left|\cos\theta_s\right|} \quad , \qquad \alpha_p = \frac{k_0\left(\hat{e}_p\cdot\vec{\varepsilon}_i^0\cdot\hat{e}_p\right)}{2n_pg_p\left|\cos\theta_p\right|}, \tag{4.38}$$

as derived in Appendix A (Eq. A.9). It should be noticed that the effective absorption constants for the waves S and P can differ from each other even in the case where the tensor $\vec{\varepsilon}_i^0$ is isotropic. This is the case when the directions of propagation are not
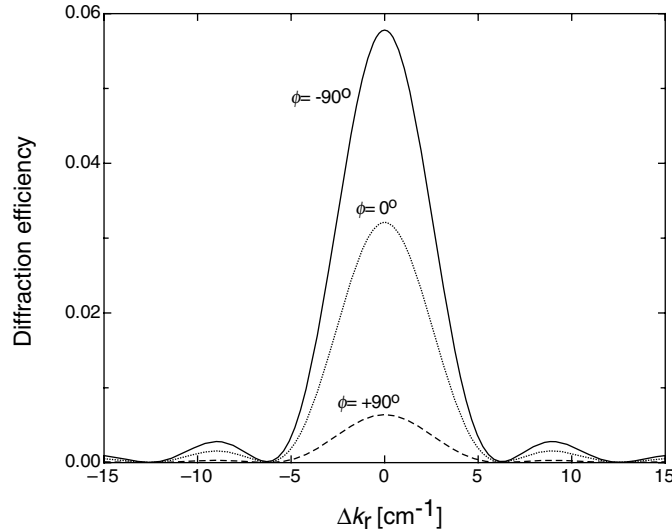
Figure 4.3: Mixed transmission grating. Diffraction efficiency vs. the real grating mismatch parameter Δk_r for three values of the phase-shift angle ϕ between phase and absorption grating. Parameters: $A_r = 2 \times 10^{-5}$, $A_i = 2 \times 10^{-5}$, $\lambda = 633$ nm, $d = 1$ cm, $\alpha_s = 0.4$ cm^{-1}, $\alpha_p = 0.7$ cm^{-1}, $n_s = 2.2$, $n_p = 2.0$, $g_s = 1.0$, $g_p = 0.95$, $\theta_s = 10°$, and $\theta_p = -40°$.

symmetric with respect to the surface normal due to a different propagation distance of the two waves inside the absorbing medium.

Equation (4.37) describes completely the diffraction at a mixed phase and absorption transmission grating in anisotropic media. As an example, Fig. 4.3 shows that the total diffraction efficiency strongly depends on the phase-shift ϕ between phase and absorption grating, which is in agreement with previous analysis of mixed phase and absorption gratings in isotropic media [107]. This behaviour is easily explained by the interference of the waves scattered off the phase and absorption grating, respectively, and leads to a nonreciprocal behaviour of the light-diffraction [108].

4.2.2   Transmission gratings with refractive index modulation only

Let us consider now the case where the grating consists only of a refractive index modulation. In absence of absorption modulation we have $A_i = 0$ and the quantity W^2 can be simplified and rewritten as

$$W^2 = \frac{1}{d^2} \left(\nu^2 + \xi^2 + i\chi^2 \right), \tag{4.39}$$

where the real quantities ν^2, ξ^2 and χ^2 are defined as

$$\nu^2 = \frac{k_0^2 A_r^2}{16 n_s n_p g_s g_p \cos\theta_s \cos\theta_p} d^2, \tag{4.40}$$

$$\xi^2 = \frac{\Delta k_r^2 - \Delta k_i^2}{4} d^2 = \left[\frac{\Delta k_r^2}{4} - \frac{(\alpha_p - \alpha_s)^2}{4} \right] d^2, \tag{4.41}$$

$$\chi^2 = \frac{\Delta \vec{k}_r \cdot \Delta \vec{k}_i}{2} d^2 = \left[\frac{\Delta k_r (\alpha_p - \alpha_s)}{2} \right] d^2. \tag{4.42}$$

The diffraction efficiency of Eq. (4.37) reads then

$$\eta\left(d\right) = \frac{\nu^2}{\sqrt{\left(\nu^2+\xi^2\right)^2+\chi^4}} \left\{ \sin^2 \sqrt{\frac{\left(\nu^2+\xi^2\right)+\sqrt{\left(\nu^2+\xi^2\right)^2+\chi^4}}{2}} \right.$$

$$\left. + \sinh^2 \sqrt{\frac{-\left(\nu^2+\xi^2\right)+\sqrt{\left(\nu^2+\xi^2\right)^2+\chi^4}}{2}} \right\} e^{-(\alpha_s+\alpha_p)d}. \tag{4.43}$$

Note that the arguments of the $\sin^2$ and $\sinh^2$ functions are always real although ξ^2 and χ^2 can be negative numbers. We notice also that the $\sinh^2$ term (second term in the curly bracket of (4.37)) survived even though there is no longer an absorption modulation. This term takes accurately into account the effect on the diffraction efficiency of a different absorption constant for the pump and signal waves. It vanishes if the effective absorption constant seen by the two waves is the same ($\alpha_s = \alpha_p = \alpha$, $\chi^2 = 0$), in which case Eq. (4.43) simplifies further to

$$\eta\left(d\right) = \frac{\sin^2\sqrt{\nu^2+\xi^2}}{\left(1+\xi^2/\nu^2\right)} e^{-2\alpha d}. \tag{4.44}$$

This equation has exactly the same form as Eq. (43) of Kogelnik [12]. However the quantities ν^2, ξ^2 and α are defined differently. The quantity ξ^2 in this case reduces to

$$\xi^2 = \frac{\Delta k_r^2}{4}d^2, \tag{4.45}$$

ν^2 is redefined according to Eq. (4.40) with the projection cosines given by Eq. (4.32), and the effective amplitude absorption constant α is given by (4.38).

A further simplification is obtained in the case of perfect Bragg matching, that is $\Delta\vec{k}_r = 0$, $\xi^2 = 0$. In this case (4.44) becomes

$$\eta\left(d\right) = \sin^2 \left(\frac{\pi A_r \, d}{2\lambda \left(n_s n_p g_s g_p \cos\theta_s \cos\theta_p\right)^{1/2}} \right) e^{-2\alpha d}, \tag{4.46}$$

where λ is the vacuum wavelength. The argument of the sin-function is of the form $(\pi\Delta n d/\lambda\cos\theta)$ in analogy with the well known Eq.(45) of Ref. [12]. Here the effective refractive index change Δn takes the form

$$\Delta n = \frac{A_r}{2\sqrt{n_s n_p g_s g_p}} \tag{4.47}$$

and $\cos\theta = (\cos\theta_s \cos\theta_p)^{1/2}$. In non absorbing materials the maximum possible diffraction efficiency is exactly 100% for phase-only gratings, regardless of the fact whether isotropic or anisotropic diffraction processes are considered.

The effect of the background absorption α_s and α_p on the Bragg-angle selectivity of a phase only grating is shown in Figure 4.4 (Eq. (4.43)). The main effect of absorption is to reduce the maximum diffraction efficiency. In addition, a certain broadening of the Bragg selectivity curve is observed if signal and pump are absorbed differently ($\alpha_s \neq \alpha_p$). For a given total absorption ($\alpha_s + \alpha_p$) the more favorable diffraction efficiency is found when the absorption difference between signal and pump is maximum. A strong difference in the effective absorption for the two waves may be observed in a number of crystals
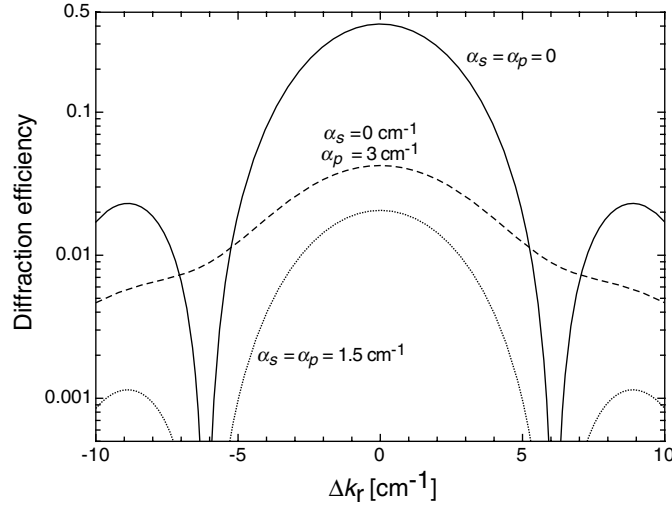
Figure 4.4: Effect of absorption on the diffraction efficiency and phase mismatch selectivity for diffraction at a grating with refractive index modulation only. Parameters: $A_r = 5 \times 10^{-5}$, $A_i = 0$, $\lambda = 633$ nm, $d = 1$ cm, $n_s = 2.2$, $n_p = 2.0$, $g_s = 1.0$, $g_p = 0.95$, $\theta_s = 10°$, and $\theta_p = -40°$.

under anisotropic Bragg diffraction geometries. It should be noticed that, despite for the fact that the mismatch term ξ^2 in Eq. (4.41) contains the term $(\alpha_p - \alpha_s)$, there is no shift in the Bragg angle for $\alpha_s \neq \alpha_p$, i.e. the maximum diffraction efficiency is still obtained for $\Delta k_r = 0$. The absorption characteristics can introduce a significant shift in the direction for which one observes the maximum diffraction efficiency only when the grating strength ν exceeds $\pi/2$. However, for absorbing materials it is usually convenient to reduce the thickness of the material and avoid this regime.

In order to visualize the essential features brought about by the material anisotropy we compare in a concrete example the theoretical expressions derived above for anisotropic media with the standard coupled wave theory for isotropic materials by Kogelnik. We choose the example of the organic material 4-N,N-Dimethylamino-4'-N-methyl-stilbazolium tosylate (DAST) [109] which has a very strong birefringence. At $\lambda = 860$ nm, $n_1 = 2.315$, $n_2 = 1.660$, $n_3 = 1.604$ [110]. For a crystal cut along the dielectric principal axes (x_1, x_2, x_3) and pump and scattered signal beams with $\vec{k}$-vectors in the 1,3-plane and directed at $\pm 25°$ to the x_3-axis one obtains $n_p = n_s = 2.119$. The energy propagation vectors $\hat{u}_p$ and $\hat{u}_s$ are then directed at $\pm 44.2°$ to the x_3-axis, giving a big walk-off angle of the order of $20°$ and $g_s = g_p = 0.945$. Figure 4.5 compares the dependence of the diffraction efficiency on refractive index change Δn as obtained from Eqs. (4.46) and (4.47) with the dependence predicted by Eq. (45) in Ref. [12]. It becomes clear that in such highly birefringent materials the use of Kogelnik's expressions leads to large errors even in such fully symmetric beam geometries.
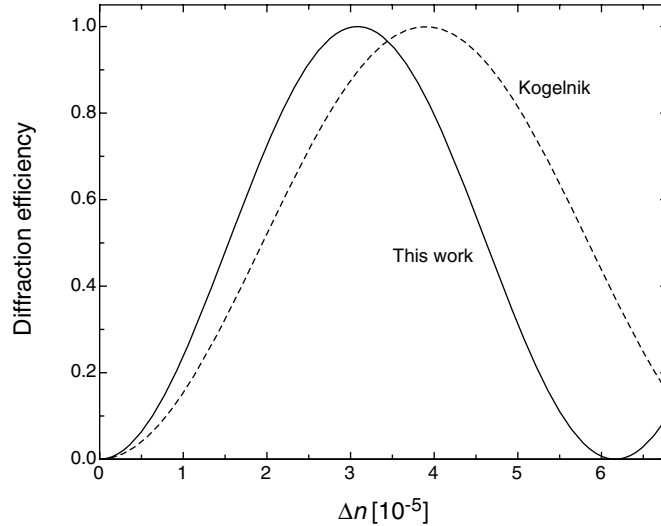
Figure 4.5: Diffraction efficiency vs. refractive index change Δn (4.47) predicted by the coupled wave theory for anisotropic materials presented here (solid line) and the isotropic coupled wave theory of Kogelnik [12] (dashed line). The diffraction is modeled for the organic crystal 4-N,N-Dimethylamino-4'-N-methyl-stilbazolium tosylate (DAST) with symmetric p-polarized signal and pump wave propagating in the 1,3-plane ($\widehat{\zeta} = \widehat{x}_3$) and the grating wavevector parallel to the 1-axis. Parameters: $A_i = 0$, $\lambda = 860$ nm, $d = 1$ cm, $\alpha_s = \alpha_p = 0$, and $\angle(\widehat{k}_s, \widehat{x}_3) = -\angle(\widehat{k}_p, \widehat{x}_3) = 25°$, which gives $n_s = n_p = 2.119$, $g_s = g_p = 0.945$, and $\theta_s = -\theta_p = 44.2°$.

4.2.3 Transmission gratings with absorption and gain modulation only

In absence of refractive index modulation one has $A_r = 0$. The expression for the diffraction efficiency differs from Eq. (4.43) only by a $(-)$ sign

$$\eta(d) = \frac{-\nu^2}{\sqrt{(\nu^2 + \xi^2)^2 + \chi^4}} \left\{ \sin^2 \sqrt{\frac{(\nu^2 + \xi^2) + \sqrt{(\nu^2 + \xi^2)^2 + \chi^4}}{2}} \right.$$

$$\left. + \sinh^2 \sqrt{\frac{-(\nu^2 + \xi^2) + \sqrt{(\nu^2 + \xi^2)^2 + \chi^4}}{2}} \right\} e^{-(\alpha_s + \alpha_p)d}. \tag{4.48}$$

The parameter ν^2 is defined here as

$$\nu^2 = \frac{-k_0^2 A_i^2}{16 n_s n_p g_s g_p \cos\theta_s \cos\theta_p} d^2 \tag{4.49}$$

and is a negative number, while ξ^2 and χ^2 are still given by Eqs. (4.41) and (4.42), respectively. In the limit of Bragg condition fulfillment and no absorption difference between the two waves ($\xi^2 = 0, \chi^2 = 0$) Eq. (4.48) reduces to

$$\eta(d) = \sinh^2 \left(\frac{\pi A_i d}{2\lambda (n_s n_p g_s g_p \cos\theta_s \cos\theta_p)^{1/2}} \right) e^{-2\alpha d}. \tag{4.50}$$

In analogy with Ref. [12] the argument of the sinh-function is of the form $\Delta\alpha d / (2\cos\theta)$ with

$$\Delta\alpha = \frac{\pi A_i}{\lambda\sqrt{n_s n_p g_s g_p}} \tag{4.51}$$

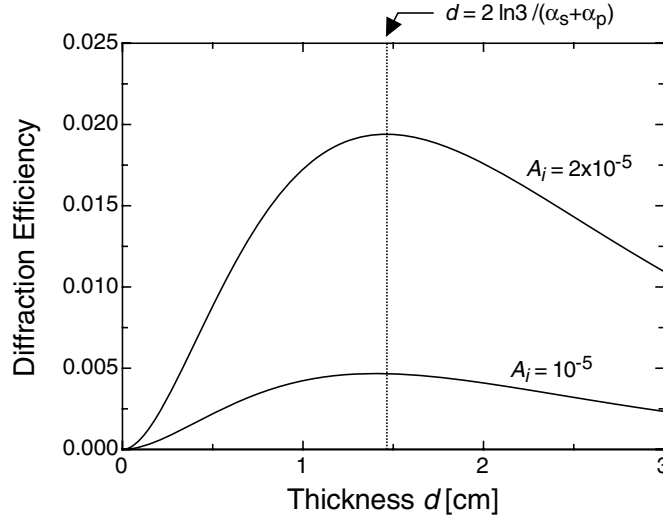and $\cos\theta = (\cos\theta_s \cos\theta_p)^{1/2}$.

Figure 4.6: Diffraction efficiency vs. grating thickness d for transmission grating with absorption modulation only. The curves are obtained using Eq.(4.48) by assuming perfect Bragg-matching ($k_r = 0$). Parameters: $A_r = 0$, $\lambda = 633$ nm, $n_s = 2.2$, n_p 2.0, $g_s = 0.98$, $g_p = 0.95$, $\alpha_s = 0.5$ cm^{-1}, $\alpha_p = 1.0$ cm^{-1}, $\theta_s = 20°$, and $\theta_p = -30°$. The vertical line indicates the optimum thickness for maximum diffraction efficiency.

As already pointed out by Kogelnik the diffraction efficiency of a pure absorption grating in transmission cannot exceed $\eta_{\max} = 1/27 = 3.7\%$. This is still true also by inclusion of absorption and dielectric anisotropies and is a direct consequence of the assumed inequality (4.11) which states that there are no positions with local gain for the optical waves [2]. Therefore an absorption modulation is always connected to a certain background average absorption which leads to the reduction of the diffraction efficiency. The optimum value of 3.7% is reached when $(\alpha_s + \alpha_p)d = 2\ln 3$ if at the same time the condition

$$\frac{k_0 A_i}{\sqrt{n_s n_p g_s g_p \cos\theta_s \cos\theta_p}} = \alpha_s + \alpha_p \tag{4.52}$$

is fulfilled. Note that under the validity of (4.11) the left-hand side of (4.52) is always smaller or equal to the right-hand side. Figure 4.6 shows the dependence of the diffraction efficiency on the grating thickness d for two values of the coupling constant A_i. Perfect Bragg matching is assumed. The occurrence of an optimum thickness can be easily recognized.

4.3 Reflection gratings

4.3.1 Mixed reflection gratings

Reflection gratings are characterized by the conditions $\hat{u}_p \cdot \hat{\zeta} = \cos\theta_p > 0$ and $\hat{u}_s \cdot \hat{\zeta} = \cos\theta_s < 0$. As shown in Fig.4.2, we assume the medium to be a plane parallel plate of thickness d with surfaces oriented in arbitrary directions with respect to the optical

---

[2]Note that in the derivation of Eqs.(4.48) and (4.50) the condition (4.11) was not used. Therefore Eqs.(4.48) and (4.50) are valid also for the description of gain gratings with negative absorption constants, in this case the diffraction efficiency can largely exceed 1.

main axes and of infinite lateral dimensions. Let the pump wave P enter the holographic medium from the face defined by $\hat{\zeta} \cdot \vec{r} = 0$. The boundary conditions valid for reflection gratings are then

$$E_s \left(\hat{\zeta} \cdot \vec{r} = d \right) = 0 \tag{4.53}$$

and

$$\frac{\partial E_s}{\partial \vec{r}} \cdot \hat{u}_s \left(\hat{\zeta} \cdot \vec{r} = 0 \right) = \frac{k_0}{4 n_s g_s} \left[i \, A_r - A_i e^{i\phi} \right] E_{p0} e^{i \Delta \vec{k} \cdot \vec{r}}, \tag{4.54}$$

where $E_{p0} = E_p \left(\hat{\zeta} \cdot \vec{r} = 0 \right)$. Proceeding in the same way as for transmission holograms we insert $E_s = E_{s1} \exp \left(\vec{\gamma}_1 \cdot \vec{r} \right) + E_{s2} \exp \left(\vec{\gamma}_2 \cdot \vec{r} \right)$ into the second order differential equation (4.24) and use the above boundary conditions to obtain the general solution for the evolution of the signal wave amplitude

$$E_s \left(\vec{r} \right) = \frac{k_0}{4 n_s g_s \cos \theta_s} \frac{A_r + i A_i e^{i\phi}}{\left(\frac{\Delta k_r + i \Delta k_i}{2} \right) \left[e^{iWd} - e^{-iWd} \right] + W \left[e^{iWd} + e^{-iWd} \right]}$$
$$\times e^{i \frac{\Delta k_r + i \Delta k_i}{2} \hat{\zeta} \cdot \vec{r}} \left[e^{iW \left(\hat{\zeta} \cdot \vec{r} - d \right)} - e^{-iW \left(\hat{\zeta} \cdot \vec{r} - d \right)} \right] E_{p0}, \tag{4.55}$$

where the property that the vector $\Delta \vec{k}$ is constrained to be parallel to $\hat{\zeta}$, so that $\Delta \vec{k}_r = \Delta k_r \hat{\zeta}$ and $\Delta \vec{k}_i = \Delta k_i \hat{\zeta}$ was used again. The quantity $W = \sqrt{W^2}$ is the same as given in Eq. (4.31), for reflection gratings it can be rewritten as

$$W^2 = \left(\frac{\Delta k_r + i \left(\alpha_s + \alpha_p \right)}{2} \right)^2 + \frac{k_0^2 \left(A_r^2 - A_i^2 + 2 i A_r A_i \cos \phi \right)}{16 n_s n_p g_s g_p \cos \theta_s \cos \theta_p}, \tag{4.56}$$

where we have used Eqs. (4.1) and (4.14) as well as $\vec{k}_{s,i} = -\alpha_s \hat{\zeta}$, $\vec{k}_{p,i} = +\alpha_p \hat{\zeta}$. In analogy to (4.35), the evolution of the pump wave amplitude is obtained as

$$E_p \left(\vec{r} \right) = \left[\frac{\left[2W + \Delta k \right] e^{iW \left(\hat{\zeta} \cdot \vec{r} - d \right)} + \left[2W - \Delta k \right] e^{-iW \left(\hat{\zeta} \cdot \vec{r} - d \right)}}{\left[2W + \Delta k \right] e^{-iWd} + \left[2W - \Delta k \right] e^{iWd}} \right] e^{-i \left(\frac{\Delta k}{2} \right) \hat{\zeta} \cdot \vec{r}} E_{p0}, \tag{4.57}$$

where $\Delta k = \Delta k_r + i \Delta k_i$. The diffraction efficiency of a reflection hologram is defined as

$$\eta = \frac{I_s \left(\hat{\zeta} \cdot \vec{r} = 0 \right)}{I_p \left(\hat{\zeta} \cdot \vec{r} = 0 \right)} = \frac{E_s E_s^* n_s g_s}{E_{p0} E_{p0}^* n_p g_p} \left| \frac{\cos \theta_s}{\cos \theta_p} \right|, \tag{4.58}$$

where again an obliquity factor is introduced in the definition. Inserting the complex signal wave amplitude (4.55) into (4.58) one obtains the general expression for the diffraction efficiency of a mixed phase and absorption reflection grating in anisotropic media with absorption anisotropy

$$\eta = \frac{-k_0^2 \left(A_r^2 + A_i^2 - 2 A_r A_i \sin \phi \right)}{16 n_s n_p g_s g_p \cos \theta_s \cos \theta_p} \frac{1}{R} \left\{ \sin^2 \left(\text{Re} \left[W \right] d \right) + \sinh^2 \left(\text{Im} \left[W \right] d \right) \right\}, \tag{4.59}$$

where the quantity R is given as

$$R = \left[\frac{(\Delta k_r)^2}{4} + \frac{(\alpha_s + \alpha_p)^2}{4} \right] \left\{ \sinh^2 \left(\operatorname{Im} [W] \, d \right) + \sin^2 \left(\operatorname{Re} [W] \, d \right) \right\}$$

$$+ \left| W^2 \right| \left\{ \cosh^2 \left(\operatorname{Im} [W] \, d \right) - \sin^2 \left(\operatorname{Re} [W] \, d \right) \right\}$$

$$+ \operatorname{Re} [W] \left[\frac{(\alpha_s + \alpha_p)}{2} \sin \left(2 \operatorname{Re} [W] \, d \right) + \frac{\Delta k_r}{2} \sinh \left(2 \operatorname{Im} [W] \, d \right) \right]$$

$$+ \operatorname{Im} [W] \left[\frac{(\alpha_s + \alpha_p)}{2} \sinh \left(2 \operatorname{Im} [W] \, d \right) - \frac{\Delta k_r}{2} \sin \left(2 \operatorname{Re} [W] \, d \right) \right]. \tag{4.60}$$
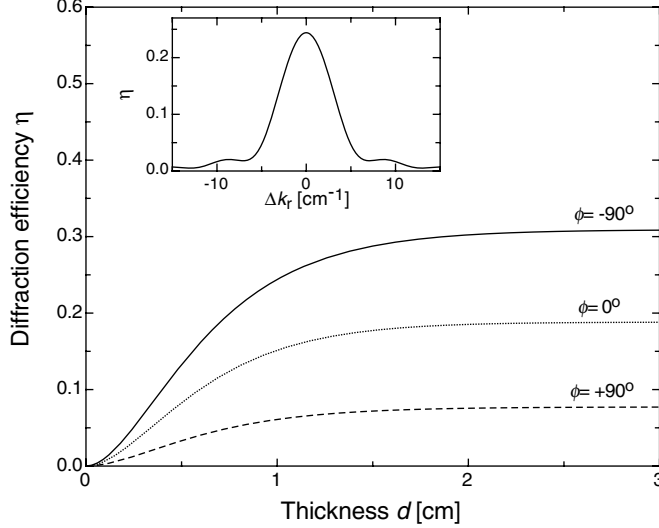
Figure 4.7: Mixed reflection grating. Diffraction efficiency vs. thickness d for three values of the phase-shift angle ϕ between phase and absorption grating. Parameters: $A_r = 6 \times 10^{-5}$, $A_i = 2 \times 10^{-5}$, $\lambda = 633$ nm, $\Delta k_r = 0$, $\alpha_s = 0.7$ cm^{-1}, $\alpha_p = 1.0$ cm^{-1}, $n_s = 2.2$, $n_p = 2.0$, $g_s = 1.0$, $g_p = 0.95$, $\theta_s = -170°$, $\theta_p = -40°$. The inset shows the dependence of the diffraction efficiency on the phase mismatch Δk_r for $d = 1$ cm, $\phi = -90°$, and the other parameters as above.

The overall diffraction efficiency of mixed reflection gratings depends again on the phase-shift ϕ between phase and absorption grating components, as shown in Fig. 4.7 where η is plotted versus the material thickness. This leads again to non-reciprocal transmission as in the case of transmission gratings discussed above. It is clearly recognized in Fig. 4.7 that after reaching saturation, a further increase in thickness does not lead to a larger diffraction efficiency. Physically, this is easily understood by the fact that the pump wave intensity I_p does strongly decrease with increasing depth due to the combined effects of back diffraction and absorption. An example of angular mismatch characteristics for reflection gratings is plotted as an inset in Fig. 4.7.

4.3.2   Reflection gratings with refractive index modulation only

In analogy with section 4.2.2 one can write $W^2 = \left(\nu^2 + \xi^2 + i \chi^2 \right) / d^2$, with ν^2 given by Eq. (4.40) being now a negative real number,

$$\xi^2 = \left[\frac{(\Delta k_r)^2 - (\alpha_s + \alpha_p)^2}{4} \right] d^2, \tag{4.61}$$

and

$$\chi^2 = -\left[\frac{\Delta k_r\,(\alpha_s + \alpha_p)}{2}\right] d^2. \tag{4.62}$$

The diffraction efficiency is found from Eq. (4.59) as

$$\eta = \frac{-\nu^2}{d^2 R}\left\{\sin^2\left(\mathrm{Re}\,[W]\,d\right) + \sinh^2\left(\mathrm{Im}\,[W]\,d\right)\right\}, \tag{4.63}$$

where R is given by (4.60) and the real and imaginary components of the coupling quantity W are

$$\mathrm{Re}\,[W] = \pm\frac{1}{d}\sqrt{\frac{(\nu^2 + \xi^2) + \sqrt{(\nu^2 + \xi^2)^2 + \chi^4}}{2}}, \tag{4.64}$$

$$\mathrm{Im}\,[W] = \pm\frac{1}{d}\sqrt{\frac{-(\nu^2 + \xi^2) + \sqrt{(\nu^2 + \xi^2)^2 + \chi^4}}{2}}. \tag{4.65}$$

In the two above equations the signs $(+)$ or $(-)$ have to be selected in order to be consistent with the quadrant of the complex quantity W^2. For the practically most interesting case of perfect phase matching and no loss Eq. (4.63) reduces to

$$\eta = \tanh^2\sqrt{-\nu^2} = \tanh^2\left(\frac{\pi A_r\, d}{2\lambda\,(n_s n_p g_s g_p\,|\cos\theta_s|\,\cos\theta_p)^{1/2}}\right), \tag{4.66}$$

which, with the use of (4.47) corresponds to the well known expression for isotropic dielectric reflection holograms (Eq. (59) in [12]).

Dielectric reflection gratings are interesting for applications as sharp wavelength filters, it is therefore useful to look a little more in detail at the Bragg selectivity of such gratings. In Fig. 4.8 we show the reflectivity of a grating as a function of the wavevector mismatch Δk_r [3] for different values of the coupling constant A_r and of the grating thickness d. For fixed d, besides the increase of the peak diffraction efficiency there is also a broadening of the Bragg selectivity with increasing coupling constant A_r (Fig. 4.8(a)). Ultimately, for large enough values of A_r this leads to the formation of a stop band with reflectivity equal to 1 for a broad range of wavelengths around the perfectly phase matched one. One can speak about one-dimensional photonic band-gap structures in this context. The broadening of the selectivity curve for larger A_r is physically due to a shorter average distance traveled by the pump wave inside the grating structure (smaller effective thickness). The effect of the thickness on the Bragg selectivity can be seen explicitly on Fig. 4.8 (b). Evidently, thicker gratings lead to sharper reflection filters, however, this is true only as far as the refractive index change ($\propto A_r$) is not too large. Therefore, the simultaneous optimization of the grating reflectivity and minimization of the reflected bandwidth requires a careful balance between the grating thickness and the amplitude of the refractive index modulation.

In Fig. 4.9 the maximum diffraction efficiency and the full-width-at-half-maximum (FWHM) of the Bragg selectivity are plotted as a function of the coupling constant A_r (a) and of the grating thickness d (b). The FWHM is described both in terms of the wavevector mismatch parameter Δk_r and in terms of the wavelength deviation $\Delta\lambda$ from the Bragg wavelength at the technologically very important telecommunication

---

[3]If the wavevector mismatch Δk_r is due uniquely by a mismatch $\Delta\lambda$ in the read-out wavelength λ, the relation between these two quantities is given as $\Delta\lambda \cong \Delta k_r \lambda^2/(4\pi n)$.
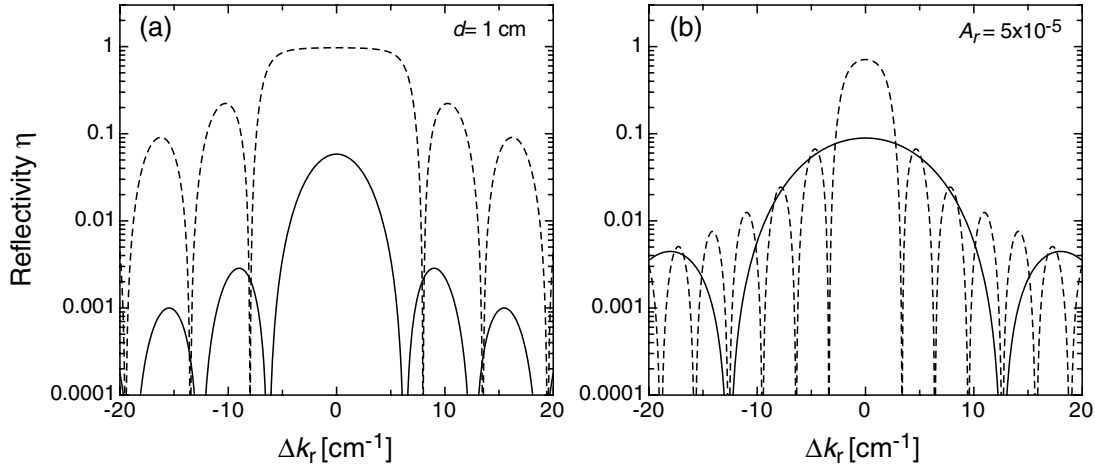
Figure 4.8: Diffraction efficiency (reflectivity) of a phase-only reflection grating as a function of the phase mismatch parameter Δk_r as obtained by Eq.(4.63). (a) $d = 1$ cm, $A_r = 2 \times 10^{-5}$ (solid curve), $A_r = 2 \times 10^{-4}$ (dashed curve); (b) $A_r = 5 \times 10^{-5}$, $d = 0.5$ cm (solid curve), $d = 2$ cm (dashed curve); The other parameters are: $\lambda = 633$ nm, $\alpha_s = \alpha_p = 0$, $n_s = 2.2$, $n_p = 2.0$, $g_s = 1.0$, $g_p = 0.95$, $\theta_s = 10°$, $\theta_p = 170°$.

wavelength of 1.55 μm. Again, the broadening of the spectral reflectivity band for larger A_r can be easily recognized. As seen in Fig. 4.8(a) this effect is also accompanied by a strong rise of the side lobes. In contrast, increase of d always leads to a decrease of the spectral reflectivity bandwidth. Note however, that once saturation of the diffraction efficiency is reached, the narrowing is practically stopped because virtually no light reaches the deepest regions of the grating. At this point smaller FWHM can only be obtained by simultaneous increase in thickness and decrease in grating strength A_r.
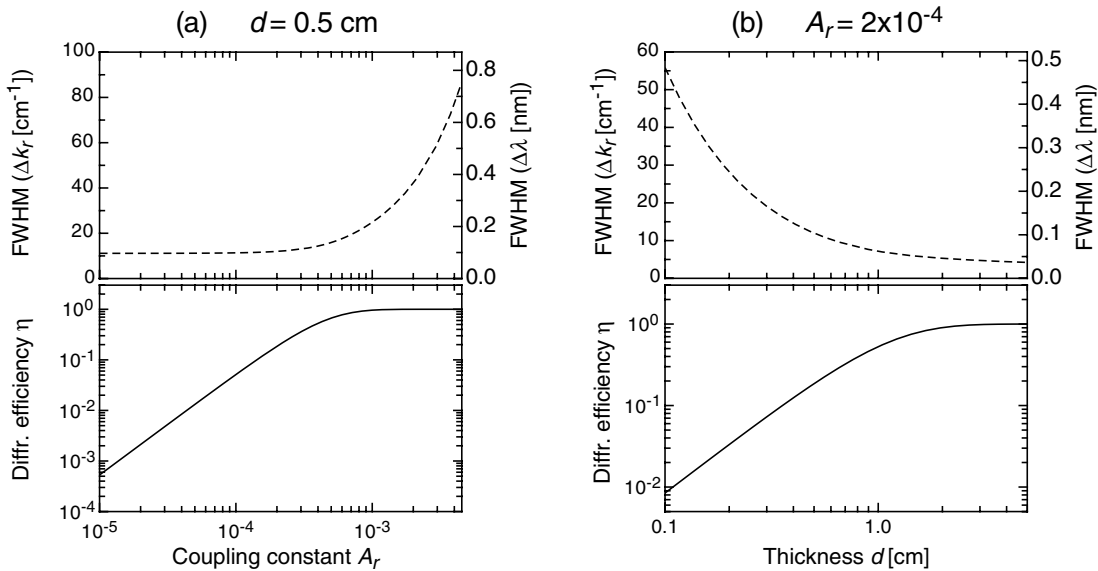
Figure 4.9: Maximum diffraction efficiency (lower graphs) and FWHM (upper graphs) as a function of the coupling constant A_r (a) and of the grating thickness d (b) as obtained by Eq.(4.63). (a) $d = 0.5$ cm; (b) $A_r = 2 \times 10^{-4}$; The other parameters are: $\lambda = 1.55$ μm, $\alpha_s = \alpha_p = 0$, $n_s = n_p = 2.2$, $g_s = g_p = 1.0$, $\theta_s = 0°$, $\theta_p = 180°$.

4.3.3 Reflection gratings with absorption modulation only

For $\overleftrightarrow{\varepsilon}_r^1 = \overleftrightarrow{0}$ the quantity ν^2 is given by Eq.(4.49) and is now a positive real number. The diffraction efficiency is then expressed as

$$\eta = \frac{\nu^2}{d^2 R} \left\{ \sin^2(\mathrm{Re}\,[W]) + \sinh^2(\mathrm{Im}\,[W]) \right\}, \tag{4.67}$$

with R, ξ^2, χ^2, $\mathrm{Re}\,[W]$ and $\mathrm{Im}\,[W]$ obtained from (4.60), (4.61), (4.62), (4.64) and (4.65), respectively. Under Bragg incidence one has $\Delta \vec{k}_r = 0$ and thus $\chi^2 = 0$. It holds further that $\Delta \alpha \leq \alpha_s$, which implies $\nu^2 + \xi^2 < 0$, Eq. (4.67) transforms then for Bragg incidence into

$$\eta = \nu^2 \left[-\xi^2 + \sqrt{-(\nu^2 + \xi^2)}\,(\alpha_s + \alpha_p)\,d \coth \sqrt{-(\nu^2 + \xi^2)} \right.$$
$$\left. - \left(\nu^2 + \xi^2\right) \coth^2 \sqrt{-(\nu^2 + \xi^2)} \right]^{-1}. \tag{4.68}$$

In the case where solely positive absorption is considered (no gain), the inequality (4.11) implies $k_0 A_i / \sqrt{n_s n_p g_s g_p \cos\theta_s \cos\theta_p} \leq \alpha_s + \alpha_p$ in analogy with (4.52). In the case when the equal sign holds one has $\xi^2 = -4\nu^2 < 0$. By inserting it into (4.68) in the limit $\xi^2 \to -\infty$ (large absorption) one finds the maximum possible diffraction efficiency achievable by a reflection grating with absorption modulation only, that is $\eta = 1/(7 + 4\sqrt{3}) = 7.2\%$.

The above expressions in this section are valid for the case of positive absorption. In the opposite case of optical gain (negative absorption constants) the solutions (4.67) and (4.68) are no longer valid. In fact a modulated gain in a reflection geometry leads to laser oscillation. This process does not obey the boundary conditions (4.53) and (4.54) and therefore the corresponding solutions cannot be applied to the description of the oscillation. We recall that this limitation is not present for transmission gratings, where only amplification but no oscillation can occur. As pointed out above (see footnote on page 52) the solutions for positive absorption are valid also for the case of gain.

4.4 Photorefractive phase gratings

In terms of light diffraction, plane wave photorefractive phase holograms can be treated by inserting the refractive index change induced by the photorefractive effect in the equations derived above [4]. Therefore we are left with the task of determining the value of the coupling constant A_r for the photorefractive case. We have first to relate the change of the inverse dielectric constant $\Delta \overleftrightarrow{\varepsilon}_r^{-1} \equiv \Delta \left(1/n^2\right)_{ij}$ calculated in Chapter 3 (Eq. (3.14)) with the change of the (direct) dielectric constant $\Delta \overleftrightarrow{\varepsilon}_r \equiv \overleftrightarrow{\varepsilon}_r^1$ contained in the defining expression (4.25) for the quantity A_r. This relationship is given by

$$\Delta \overleftrightarrow{\varepsilon}_r = \overleftrightarrow{\varepsilon}_r^1 = - \left(\overleftrightarrow{\varepsilon}_r \cdot \Delta \overleftrightarrow{\varepsilon}_r^{-1} \cdot \overleftrightarrow{\varepsilon}_r \right) \cong - \left(\overleftrightarrow{\varepsilon}_r^0 \cdot \Delta \overleftrightarrow{\varepsilon}_r^{-1} \cdot \overleftrightarrow{\varepsilon}_r^0 \right), \tag{4.69}$$

where the last equality is valid because we assumed $\left\| \overleftrightarrow{\varepsilon}_r^1 \right\| \ll \left\| \overleftrightarrow{\varepsilon}_r^0 \right\|$, which is usually fulfilled in photorefractive experiments. By combining the above equation (4.69) with

---

[4]This is strictly correct only as far as the pump and signal wave do not modify the grating during its read-out, otherwise the feedback of the waves onto the grating has to be taken into account in a self-consistent manner.

Eqs. (4.25) and (3.14) one obtains

$$A_r = -\hat{e}_s \cdot \vec{\varepsilon}_r^0 \cdot \left(\vec{r}^{eff} \cdot \hat{K} \right) \cdot \vec{\varepsilon}_r^0 \cdot \hat{e}_p \; E_1, \tag{4.70}$$

where the tensor $\vec{r}^{eff}$ is the third-rank effective electro-optic tensor defined in (3.15) and takes into account all mechanical coupling effects. Performing the tensor multiplications in the above expression leads to

$$A_r = -n_s^2 n_p^2 g_s g_p r_{eff} \; E_{sc}, \tag{4.71}$$

where n_s and n_p are the refractive indices seen by the signal and pump wave, respectively, and r_{eff} is the scalar effective electro-optic coefficient defined in Eq. (3.17).

The expression (4.71) can now be inserted into Eqs. (4.43) and (4.63) to obtain the diffraction efficiency η of photorefractive transmission and reflection gratings. We give here only the special cases valid for phase-matched Bragg-diffraction in non absorbing materials. For transmission gratings in a medium of thickness d one gets

$$\eta = \sin^2 \left(\frac{\pi}{2\lambda} \left(\frac{g_s g_p}{\cos\theta_s \cos\theta_p} \right)^{1/2} (n_s n_p)^{3/2} \, r_{eff} E_{sc} d \right), \tag{4.72}$$

while for reflection gratings the result is

$$\eta = \tanh^2 \left(\frac{\pi}{2\lambda} \left(\frac{g_s g_p}{\cos\theta_s \cos\theta_p} \right)^{1/2} (n_s n_p)^{3/2} \, r_{eff} E_{sc} d \right). \tag{4.73}$$

4.5 Summary

In this chapter we have given a detailed treatment of light diffraction at volume transmission or reflection gratings by extending the well known Kogelnik's coupled wave theory to the case of anisotropic media. The new expressions given here are valid for general interaction geometries in parallel plate media cut in arbitrary directions with respect to the crystallographic axes. They consider explicitely a combination of refractive index and absorption or gain gratings with arbitrary relative phase relationship. The correct expressions describing light diffraction in anisotropic non optically active photorefractive crystals in the framework of the coupled waves analysis were given as a special case in the last section.

Chapter 5

Two-wave mixing

In the case of light diffraction treated above in Chapter 4 the signal wave S has a vanishing amplitude at the entrance surface into the holographic medium. In contrast, for the case of two-wave mixing the signal wave is injected and has a nonzero amplitude at the entrance surface. Therefore the two situations differ solely by the boundary conditions and can be treated using the same coupled wave equations derived in Chapter 4. Two-wave mixing (TWM) leads in general to energy and/or phase transfer between the waves, therefore (TWM) is often simply called two-beam coupling. The kind and magnitude of the coupling depends on the phase relationship between the waves and the grating. In this chapter we will treat principally the case of photorefractive two-wave mixing, in which case the grating at which the two waves couple is dynamically created by the waves themselves. However, before doing that we want to consider shortly the case when two waves couple at a prerecorded fixed grating.

5.1 Two-wave mixing at fixed grating

To treat the case of two-wave mixing at a fixed grating we refer to the formalism developed in Chapter 4. In the case of light diffraction discussed above the phase of the diffracted signal wave is determined solely by the phase position of the grating. In contrast, for two wave mixing there are two absolute reference phases, one given by the grating position (for instance the positions of the refractive index maxima) and the other given by the position of the interference fringes created by the signal and the pump wave. Both are defined from outside. Different relative shifts between the two reference phases lead to a different coupling between pump and signal.

    Let us suppose we want to know the amplitude of the signal wave S after coupling with the pump wave P at a fixed transmission grating. This amplitude is a coherent superposition of the transmitted amplitude of S when the wave P is absent and the amplitude diffracted from P in direction of S, when the latter has zero amplitude at the entrance face. Therefore one first calculates the transmitted amplitude $E_{s,t}\left(\hat{\zeta} \cdot \vec{r} = d\right)$ using Eq. (4.35) letting S take the role of the pump wave. Secondly, the amplitude $E_{s,d}\left(\hat{\zeta} \cdot \vec{r} = d\right)$ scattered from P into the general direction of S is calculated using Eq. (4.34) by extracting the correct wave propagation direction $\vec{k}_{s,d}$ from Eq. (4.14). Finally the two waves are added and combined with the phase factors as $E_{s,t} \exp\left(i\vec{k}_s \cdot \vec{r}\right) + E_{s,d} \exp\left(i\vec{k}_{s,d} \cdot \vec{r}\right)$ to obtain the electric field amplitude of the wave S at the exit of the grating region. In analogy, in the case of a fixed reflection holograms

the same procedure outlined above is followed. One uses Eqs. (4.57) and (4.55) instead of Eqs. (4.35) and (4.34) to obtain the transmitted and in-diffracted amplitudes.

Before treating the most interesting case of perfect phase matching $(\vec{k}_{s,d} \equiv \vec{k}_s)$, where the transmitted and in-diffracted wave are not distinguishable, it is useful to consider one aspect of Bragg diffraction that was not mentioned in Chapter 4. Our interest should go first at the phase relationship between the refractive index or absorption grating and the fringes formed by the interference of the transmitted read-out wave P (determined from (4.35)) with the diffracted wave S (determined from (4.34)). For perfect Bragg matching these fringes (calculated from the modulation of the local optical energy density) must have the same periodicity $\vec{K}$ of the grating. This is clearly seen in Fig. 5.1 which shows the phase relationship between the optical energy density $(\propto |\vec{E}_s + \vec{E}_p|^2)$ and a refractive index (a) or an absorption grating (b) of the transmission type. The refractive index grating modulation is characterized by the function $g(\vec{r})$ corresponding to the cosine term in the first square bracket of Eq. (4.6). Similarly, the absorption grating in (b) is described by a corresponding function $f(\vec{r})$ which is assumed to have positive values for positive absorption changes. The fringes and grating modulation are plotted in Fig. 5.1 along the exit surface $\hat{\zeta} \cdot \vec{r} = d$ (see Fig. 4.2) with $\vec{r}_{\parallel}$ being a vector inside this surface. It can be easily proved that in the case of a pure phase grating, as shown in Fig. 4.2(a), the light fringes induced by the Bragg diffraction process are out of phase by $\pi/2$ with respect to the grating. It will be shown in the next section that this $\pi/2$ phase shift give the optimum energy transfer from the pump to the diffracted signal wave. In other words, the phase of the initially vanishing diffracted wave adjusts itself in order for this wave to be optimally amplified. In contrast, in the case of a pure absorption grating (Fig. 4.2(b)) the fringes are found to be out of phase with the absorption maxima, i.e. the fringe maxima establish themselves at the places where the modulated absorption is minimum. One could take a pseudo-philosophical conclusion out of these facts: light chooses its phase in order to produce the maximum possible diffracted power. This is valid for both refractive index, absorption or mixed gratings.

Let us now go back and treat in more detail the case of perfect phase matching $(\Delta k_r = 0,$ that is $\vec{k}_{s,d} \equiv \vec{k}_s)$. We consider a grating of the kind (4.6). Its relative orientation with respect to the signal and pump wave shall be such that it acts as transmission type grating. The scalar complex amplitudes of the two waves at the entrance surface are E_{s0} and E_{p0}, respectively. If the waves are perfectly phase matched to the grating an analogous calculation as the one described in Chapt. 4 leads to the expression

$$E_s\left(\vec{r}\right) = e^{-\left(\frac{\alpha_p - \alpha_s}{2}\right)\hat{\zeta}\cdot\vec{r}} \left\{ E_{p0} \frac{k_0 \left(A_r + iA_i e^{i\phi}\right)}{8n_s g_s \cos\theta_s} \frac{e^{iW(\hat{\zeta}\cdot\vec{r})} - e^{-iW(\hat{\zeta}\cdot\vec{r})}}{W} \right.$$

$$\left. + E_{s0}\left[\frac{2W - i\left(\alpha_p - \alpha_s\right)}{4W}e^{iW(\hat{\zeta}\cdot\vec{r})} + \frac{2W + i\left(\alpha_p - \alpha_s\right)}{4W}e^{-iW(\hat{\zeta}\cdot\vec{r})}\right]\right\}, \qquad (5.1)$$

which describes the evolution of the signal wave amplitude. We recall that the amplitude E_s contained in the above formula is cleaned of the absorption contribution (see Eq. (4.3)). If one considers only pure refractive index gratings ($A_i = 0$) and one assumes that the absorption constant is the same for the two waves ($\alpha_p - \alpha_s = 0$) the above expression simplifies to
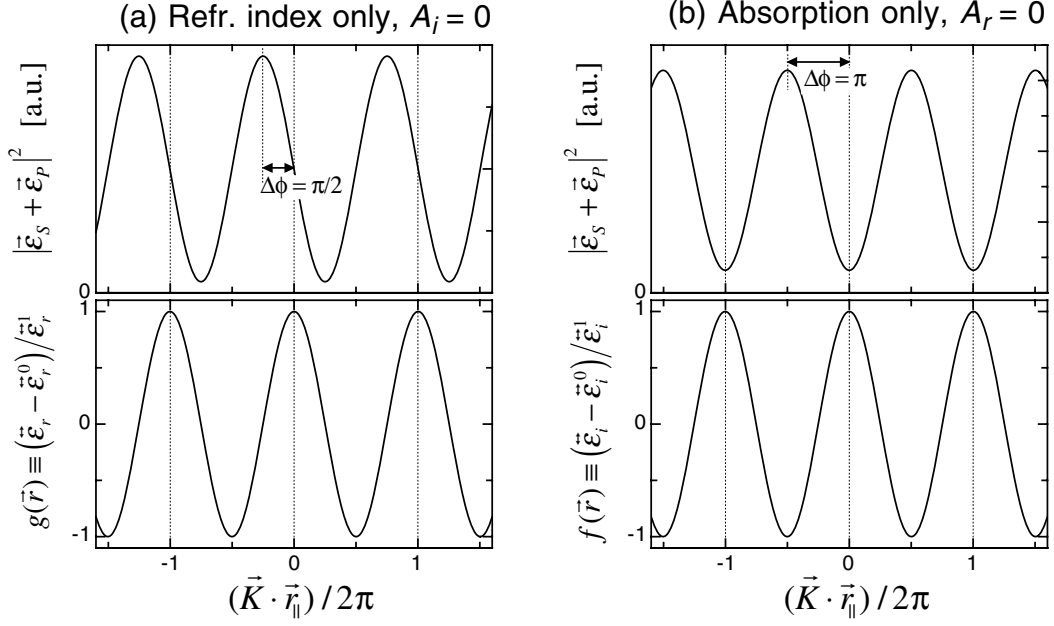
Figure 5.1: Phase relationship between modulated energy density $\propto |\vec{E}_s + \vec{E}_p|^2$ (upper graphs) and a refractive index (a) or an absorption grating (b) (lower graphs). In (b) the absorption change is positive if the function $f(\vec{r})$ is positive.

$$E_s\left(\vec{r}\right) = iE_{p0}\sqrt{\frac{n_p g_p \cos\theta_p}{n_s g_s \cos\theta_s}}\sin(\gamma\hat{\zeta}\cdot\vec{r}) + E_{s0}\cos(\gamma\hat{\zeta}\cdot\vec{r}), \tag{5.2}$$

where the coupling constant γ is given as

$$\gamma = k_0 A_r \big/ 4\sqrt{n_s n_p g_s g_p \cos\theta_s \cos\theta_p}. \tag{5.3}$$

Figure 5.2 shows the spatial evolution of the signal wave intensity ($\propto E_s E_s^*$) for three values of the phase shift δ between the input light fringes and the grating. A pure phase grating ($A_i = 0$) is assumed in a fully symmetric configuration. It can be recognized how the optimum phase shift of $\pi/2$ leads to the fastest amplification of the signal. As seen by considering Fig. 5.1 the diffracted wave from P into S carries a phase-shift of $\pi/2$, therefore if the input signal wave is shifted by the same amount the two components add constructively. In the opposite case in which the input wave is shifted by $-\pi/2$ the signal wave amplitude first decreases to 0 as a result of destructive interference with the diffracted pump wave. Later it increases again, however with an opposite phase with respect to the input wave. Finally, in the case where the input light fringes are exactly in phase with the grating ($\delta = 0$), the signal wave experiences a transfer of phase and its initial intensity does not contribute to increase the amplified signal. The optimum phase shift of $\delta = \pi/2$ becomes evident also by considering the upper graph in Fig. 5.2 that shows the dependence of the amplified signal on δ for $d = 0.5$ cm. If the exact grating phase position is not known, measurements of these oscillations for both waves can provide this information. Methods valid in the regime of small grating diffraction efficiency are described for instance in Refs. [111, 112].
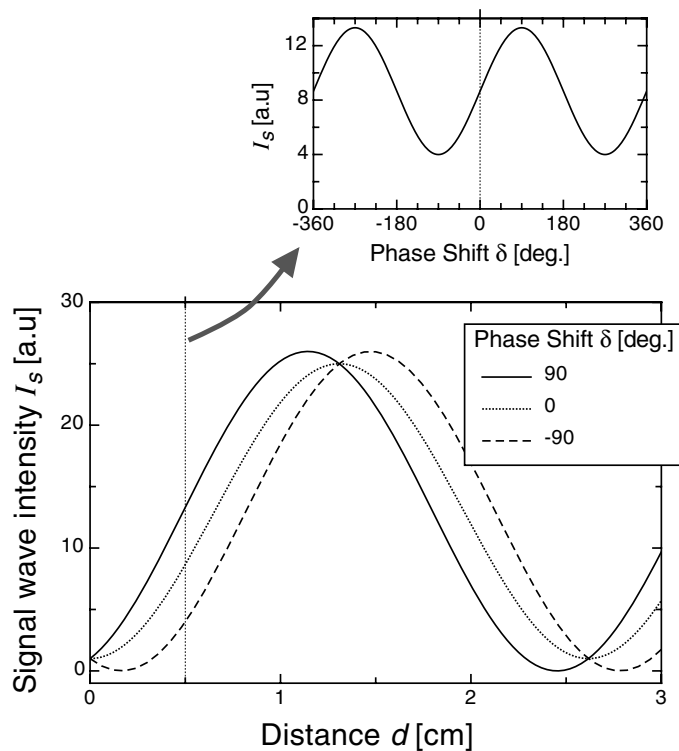
Figure 5.2: Amplification of signal wave by two-wave mixing at a fixed phase only grating. The grating strength is $A_r = 10^{-4}$ and the input pump-signal intensity and amplitude ratios are $I_{p0}/I_{s0} = 25$ and $E_{p0}/E_{s0} = 5\exp(-i\delta)$, respectively. The evolution is shown for three values of the phase shift δ between input light fringes and refractive index grating. The upper graph shows the dependence of the amplified signal on δ for $d = 0.5$ cm.

It is very interesting to compare the amplification obtained by a fixed refractive index grating of given strength with the amplification obtained by self-induced dynamic photorefractive two-wave mixing, where the grating is induced by the interacting beams themselves. This case will be treated in detail in the next section. Let us consider a material with a maximum refractive index grating strength corresponding to a coupling constant $A_r = 10^{-4}$. In absence of anisotropy enhancement a material with this optical nonlinearity can give an exponential gain coefficient of $\Gamma \approx 4.8$ cm^{-1} (see next section for definition). Figure 5.3 compares the two cases. Clearly, if amplification is the only criterion, fixed gratings lead to much better performance than dynamic self-induced gratings. For instance, in the specific example given here the point where half of the pump energy is transferred to the signal wave is reached after about 6 mm of interaction for the fixed grating and after about 14 mm for the dynamic one. The reason for the absence of oscillations in the latter case is related to the fact that the grating modulation depth becomes small both for short and large distances and will become clear in the next section.

5.2 Photorefractive two-wave mixing

In this section we treat specifically the case of photorefractive two-wave mixing. Here the dynamic gratings responsible for the coupling are recorded by the two interacting waves themselves. With respect to the case of two-wave mixing treated in the last section,
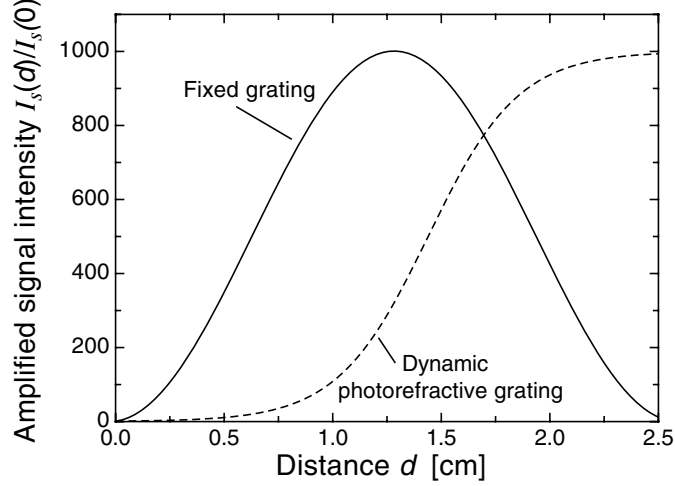
Figure 5.3: Comparison of the signal wave amplification for two-wave mixing at a fixed phase only grating (solid curve) and for two-wave mixing at a dynamic photorefractive grating (dashed curve). The optical nonlinearity is the same in the two cases ($A_r = 10^{-4}$). The input intensity ratio is $I_{p0}/I_{s0} = 1000$ and $\delta = \pi/2$.

dynamic two-wave mixing has the enormous advantage that the grating can adapt in real time to modifications in the shape and phases of the input waves. This feature is paid by a somewhat smaller optical nonlinearity because, as mentioned above, the grating modulation depth is not constant along the propagation path. With some little modifications, the treatment presented below can be extended to describe the coupling of two waves recording a grating with mechanisms other than the photorefractive effect.

The present treatment bases on the photorefractive equations discussed in Chapter 2 and on the coupled wave equations derived in Chapter 4. It considers the electro-optic and dielectric anisotropies discussed in Chapter 3. A very interesting new finding is the extremely strong influence of the photoexcitation anisotropy on the photorefractive two-wave mixing gain. This can lead to a strong enhancement of the gain under proper choice of the interaction geometry. Another interesting finding is derived for the pump depletion regime. Even for a fixed value of the photorefractive gain coefficient, an asymmetric interaction geometry or the photoexcitation anisotropy influence significantly the spatial evolution of the signal and pump intensities.

We consider the coupled wave equations (4.1) derived in Chapter 4 in the slowly varying amplitude approximation. By considering the fact that for photorefractive two-wave mixing phase matching is automatically fulfilled ($\Delta k_r = 0$) and using Eq. (4.71) describing the coupling constant $A_r \equiv \hat{e}_s \cdot \overset{\leftrightarrow}{\varepsilon}{}^1_r \cdot \hat{e}_p$ for the photorefractive case, one obtains

$$\vec{\nabla} E_s \cdot \hat{u}_s \;=\; \frac{k_0}{4 n_s g_s} \left[-iRm E_p \widetilde{E}_{sc} e^{(\alpha_s - \alpha_p)\widehat{\zeta}\cdot\vec{r}} \right], \tag{5.4a}$$

$$\vec{\nabla} E_p \cdot \hat{u}_p \;=\; \frac{k_0}{4 n_p g_p} \left[-iRm^* E_s \widetilde{E}_{sc}^* e^{(\alpha_p - \alpha_s)\widehat{\zeta}\cdot\vec{r}} \right], \tag{5.4b}$$

where $R \equiv n_s^2 n_p^2 g_s g_p r_{eff}$, and r_{eff} is given by Eq. (3.17). We recall that $\hat{u}_s$ and $\hat{u}_p$ are unit vectors in direction of the Poynting vectors of the waves S and P, respectively. The quantity

$$\widetilde{E}_{sc} \equiv E_1/m \equiv \widetilde{E}_{sc,r} + i\widetilde{E}_{sc,i} \tag{5.5}$$

is the complex amplitude of the first Fourier component of the internal space-charge field normalized by the modulation m. Its real part $\widetilde{E}_{sc,r}$ corresponds to the component of the space-charge field being in phase with the energy density distribution (2.5), while the imaginary part $\widetilde{E}_{sc,i}$ is the $\pi/2$ out-of-phase component as discussed in Section 2.1.1.

5.2.1 Undepleted pump approximation

Let us first consider the situation in which the pump is not significantly depleted by the interaction. In this regime the energy of the pump wave is always much larger than the one of the signal wave everywhere in the crystal, i.e. $|E_p|^2 [\hat{e}_p \cdot \overleftrightarrow{\kappa} \cdot \hat{e}_p] \exp(-2\alpha_p \hat{\zeta} \cdot \vec{r}) \gg |E_s|^2 [\hat{e}_s \cdot \overleftrightarrow{\kappa} \cdot \hat{e}_s] \exp(-2\alpha_s \hat{\zeta} \cdot \vec{r})$. In this case equations (5.4a) describing the evolution of the signal wave amplitude transforms to

$$\vec{\nabla} E_s \cdot \hat{u}_s = \frac{k_0 R}{2 n_s g_s} \frac{\hat{e}_s \cdot \overleftrightarrow{\kappa} \cdot \hat{e}_p}{\hat{e}_p \cdot \overleftrightarrow{\kappa} \cdot \hat{e}_p} \left[\widetilde{E}_{sc,i} - i\widetilde{E}_{sc,r} \right] E_s, \tag{5.6}$$

which can be easily solved for E_s leading to

$$E_s(\hat{\zeta} \cdot \vec{r} = d) = E_{s0} e^{(\Gamma/2)d} e^{i\delta d}. \tag{5.7}$$

With (2.4a) this corresponds to

$$|\vec{\mathcal{E}}_s|(\hat{\zeta} \cdot \vec{r} = d) = |\vec{\mathcal{E}}_{s0}| e^{(\Gamma/2 - \alpha_s)d}, \tag{5.8}$$

where E_{s0} and $\vec{\mathcal{E}}_{s0}$ are the corresponding incident amplitudes at the position $\hat{\zeta} \cdot \vec{r} = 0$. Here it is assumed that the entrance surface (surface where the wave S starts interacting with P) contains the coordinates origin. The two-wave mixing exponential gain Γ and the phase coupling factor δ in Eq. (5.7) are given by

$$\Gamma = \frac{2\pi}{\lambda} \frac{n_s n_p^2}{\cos \theta_s} g_p \frac{\hat{e}_s \cdot \overleftrightarrow{\kappa} \cdot \hat{e}_p}{\hat{e}_p \cdot \overleftrightarrow{\kappa} \cdot \hat{e}_p} r_{eff} \widetilde{E}_{sc,i}, \tag{5.9}$$

and

$$\delta = -\frac{\pi}{\lambda} \frac{n_s n_p^2}{\cos \theta_s} g_p \frac{\hat{e}_s \cdot \overleftrightarrow{\kappa} \cdot \hat{e}_p}{\hat{e}_p \cdot \overleftrightarrow{\kappa} \cdot \hat{e}_p} r_{eff} \widetilde{E}_{sc,r}. \tag{5.10}$$

We recall that $\cos \theta_s = \hat{\zeta} \cdot \hat{u}_s$ is the cosine of the angle between the Poynting vector and the surface normal. As seen in (5.9) the exponential gain depends on the photoexcitation anisotropy through the factor $(\hat{e}_s \cdot \overleftrightarrow{\kappa} \cdot \hat{e}_p / \hat{e}_p \cdot \overleftrightarrow{\kappa} \cdot \hat{e}_p)$. If the tensor $\overleftrightarrow{\kappa}$ is sufficiently anisotropic, by choosing appropriate geometries this factor can become very large with respect to 1, thus giving an enhancement of the two-wave mixing gain. Experimental evidence for the influence of this factor will be given later in this chapter. This will also demonstrate that the 'usefully dissipated energy' and *not* the local light intensity is the quantity driving the photorefractive space-charge field formation. Using the light intensity would transform the above factor to $(\hat{e}_s \cdot \hat{e}_p)$, that is to the expression found for the isotropic case.

In order to predict the magnitude of Γ and δ in a particular geometry the knowledge of the values of $\widetilde{E}_{sc,i}$ and $\widetilde{E}_{sc,r}$ is necessary. In the undepleted pump approximation, the modulation m is always small and the space-charge field amplitude is linearly proportional to m. Therefore the normalized amplitudes $\widetilde{E}_{sc,i}$ and $\widetilde{E}_{sc,r}$ do not depend at all on m in this regime. Here we limit our considerations to the predictions of the

simplest photorefractive model presented in Sect. 2.1 that considers a single defect level and a single carrier type. According to Eq. (2.15), under the assumptions of a negligible photogalvanic effect (which is usually the case in most KNbO$_3$ and BaTiO$_3$ samples) and assuming that no external electric field is applied, the normalized space-charge field amplitude $\widetilde{E}_{sc}$ reads

$$\widetilde{E}_{sc} = \pm i \frac{E_q E_D}{E_q + E_D}, \tag{5.11}$$

and therefore $\widetilde{E}_{sc,r} = 0$ under these assumptions. In (5.11) the $+$ sign holds for hole conduction and the $-$ sign holds for electron charge transport. The trap-limited field E_q and the diffusion field E_D were defined in Sect. 2.1. Equation (5.11) predicts the space-charge field amplitude in most photorefractive materials in a satisfactory way and will be used here to visualize the geometrical dependence of the gain Γ. Refined models that describe better the space-charge formation in specific situations or in specific crystal samples have been reported in literature and several of them were mentioned in Sect. 2.3. Note that effects such as electron-hole competition or multiple defect levels usually tend to decrease the space-charge field strength and, given a trap density, (5.11) can be viewed as an upper bound for the space-charge field amplitude.

For the visualization of the dependence of the exponential gain Γ in KNbO$_3$ and BaTiO$_3$ on the geometrical arrangement and on the anisotropy of the tensor $\overset{\leftrightarrow}{\kappa}$ we use the same kind of contour plot representation introduced in Chapt. 3 (Fig. 3.4). Figures 5.4 and 5.5 show the contour plot diagrams of the TWM gain Γ in the planes of maximum nonlinearity for the crystals KNbO$_3$ and BaTiO$_3$. They are obtained using Eqs. (5.9) and (5.11) for isotropic ($\kappa_{22}/\kappa_{33} = 1$) as well as anisotropic photoexcitation. In each case the effective number of traps is chosen to be $N_{eff} = 10^{17} cm^{-3}$ and hole conduction is assumed. The gain plotted here is given per unit length along the Poynting vector direction, that is it corresponds to $\Gamma \cos\theta_s$ (see (5.9)), in this way the representation becomes independent from a specific crystal cut. It appears evident that the gain landscape is dramatically modified by the anisotropy of the photoexcitation constant. The position of the maximum gain in the diagram moves by changing the parameter κ_{22}/κ_{33}, some of the mountains grow, while others decrease in height. For $\kappa_{22}/\kappa_{33} \gg 1$ the optimum condition is found for a pump beam propagating under an angle α_p close to $0°$, that is nearly perpendicular to the c-axis. In contrast, for $\kappa_{22}/\kappa_{33} \ll 1$ the optimum is for a pump beam nearly parallel to c.

Obviously, by assuming an initial light scattering distribution, the representations of Figs. 5.4 and 5.5 can be used to qualitatively predict the structure of light fanning as well as optimum configurations for various phase conjugation schemes. For a rigorous treatment, however, the knowledge of the two-wave mixing gain alone is not sufficient because grating competition effects have to be taken into account.

It is also interesting to look at the evolution of the maximum possible gain in any geometry as a function of the anisotropy parameter κ_{22}/κ_{33}. This is depicted in Fig. 5.6 for both crystals and two different values for the trap density. It is evident that the isotropic case represents a kind of worst-case situation, the maximum gain can be enhanced dramatically both by decreasing or increasing the ratio κ_{22}/κ_{33} away from 1. Note that each point in Fig. 5.6 corresponds to a different position of the maximum in the landscape diagram. It is also worth noting that, despite the fact that BaTiO$_3$ has a maximum scalar electro-optic coefficient almost three times larger than KNbO$_3$
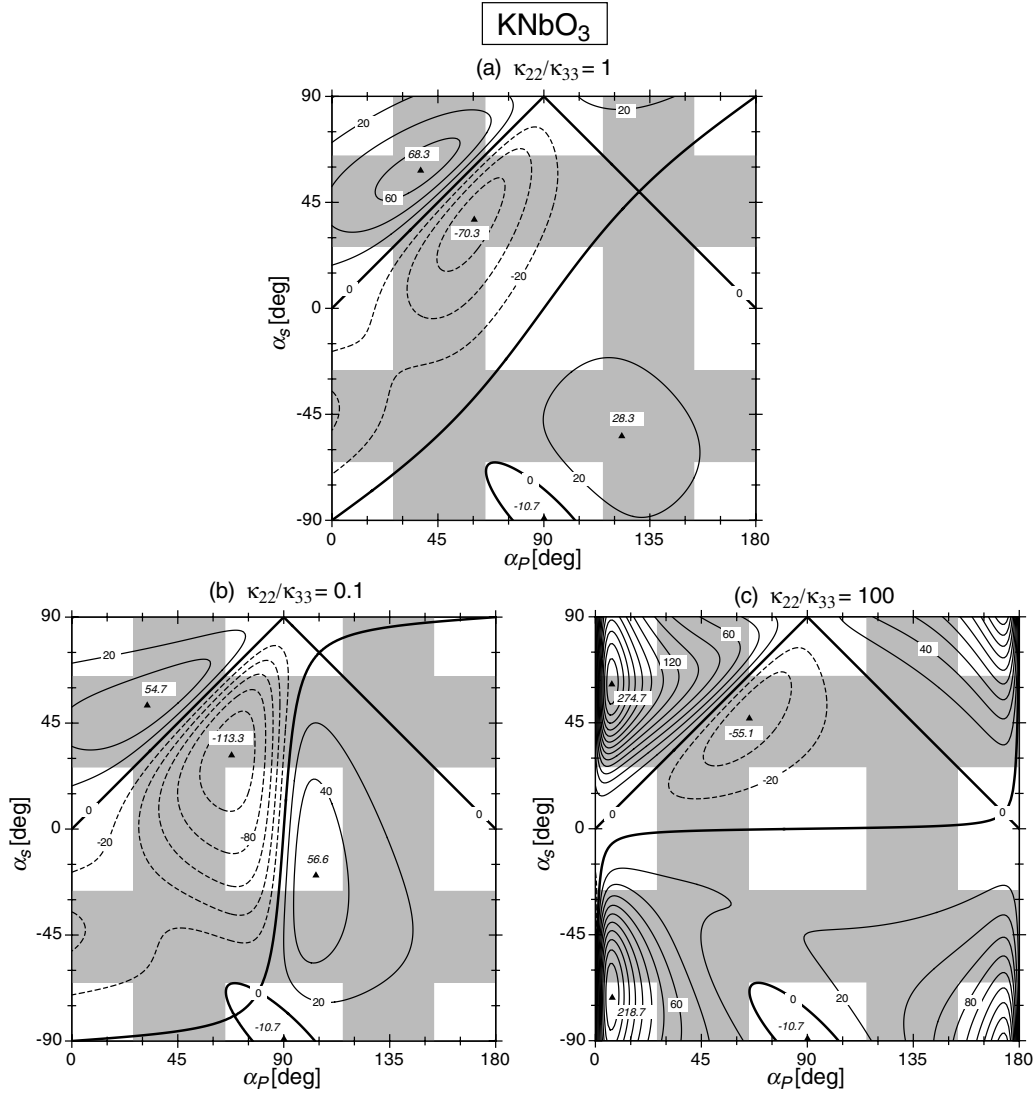
$$\boxed{\text{KNbO}_3}$$

(a) $\kappa_{22}/\kappa_{33} = 1$

(b) $\kappa_{22}/\kappa_{33} = 0.1$

(c) $\kappa_{22}/\kappa_{33} = 100$
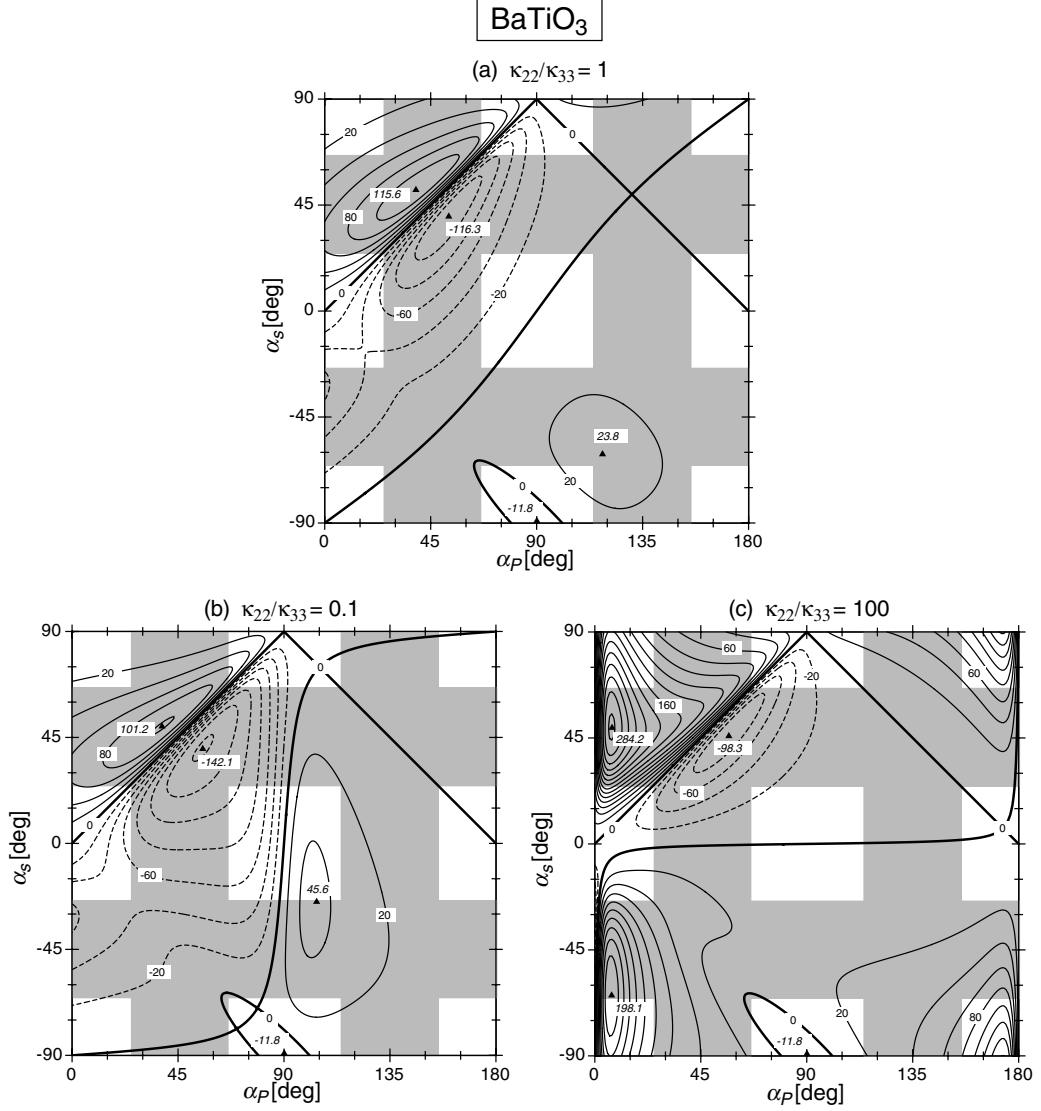
Figure 5.4: Contour plot of the exponential gain $\Gamma \cos\theta_s$ (Eq. (5.9)) for p-polarized beams in the bc-plane of KNbO$_3$. (a) Isotropic photoexcitation, $\kappa_{22}/\kappa_{33} = 1$; (b) anisotropic photoexcitation $\kappa_{22}/\kappa_{33} = 0.1$; (c) $\kappa_{22}/\kappa_{33} = 100$. Contour line distance = 20 cm^{-1}. Effective density of traps $N_{eff} = 10^{17}$cm^{-3}. For the meaning of shadows and special symbols see Fig. 3.3 on page 34.

(Fig. 3.3 and Fig. 3.4), the maximum gains are not significantly higher in this crystal (Fig. 5.6). This is because of the much larger dielectric constant of BaTiO$_3$ (Fig. 3.7) that prevents to reach a very high space-charge field $\widetilde{E}_{sc}$ in some of the geometries where the anisotropy factor in Eq. (5.9) is big.

For applications, one interesting regime is the one where the pump and signal wave propagate perpendicular to each other because in this regime linear scattering from the pump beam as well as detrimental beam-fanning can be minimized. This situation corresponds to the main diagonal in Fig. 5.4. Unfortunately, in absence of photoexcitation anisotropy the gain is very small in such geometries, as seen by the node line in Figs. 5.4(a) and 5.5(a) that runs essentially along the main diagonal. This node line is given by the condition $\hat{e}_s \cdot \overleftrightarrow{\kappa} \cdot \hat{e}_p = 0$ and is substantially modified if $\overleftrightarrow{\kappa}$ is anisotropic. Therefore large gains become possible also in this interesting kind of geometries. This is shown in Fig. 5.7 where the gain coefficient in KNbO$_3$ is plotted for $\vec{k}_s \perp \vec{k}_p$ in the same kind of diagram as in Fig. 3.7 for $\kappa_{22}/\kappa_{33} = 1$, 0.1, and 10. The situation for BaTiO$_3$ is fully analogous.

BaTiO$_3$

(a) $\kappa_{22}/\kappa_{33} = 1$

(b) $\kappa_{22}/\kappa_{33} = 0.1$ (c) $\kappa_{22}/\kappa_{33} = 100$

Figure 5.5: Contour plot of the exponential gain $\Gamma \cos\theta_s$ (Eq. (5.9)) for p-polarized beams in the ac-plane of BaTiO$_3$ in the case of isotropic (a) and anisotropic photoexcitation (b+c). Contour line distance = 20 cm^{-1}. Effective density of traps $N_{eff} = 10^{17}$cm^{-3}.

5.2.2 Pump depletion

If the initial intensity ratio between pump and signal wave is too low and the gain-length product Γd is large enough, the pump wave can be significantly depleted during the two-wave mixing interaction. This situation is more complex than the one found in the weak signal regime. In order to determine the spatial evolution of the signal and pump waves one has then to rely in most cases to a numerical integration of the coupled equations (5.2). An example is when the two beams enter the crystal from surfaces which are not parallel to each other, in which case the surface normal vectors $\widehat{\zeta_s} \neq \widehat{\zeta_p}$ and the waves S and P are no longer homogeneous in a direction perpendicular to the corresponding surface normal. It should also be remarked that for a general geometry the absorption constants α_s and α_p for the two waves usually differ from each other (this statement is true even in fully isotropic materials as long as the interaction geometry is not symmetric with respect to the surface normal), therefore also in this case the coupled wave equations may be integrated numerically.

For simplicity we consider here explicitly only cases where the two waves enter the
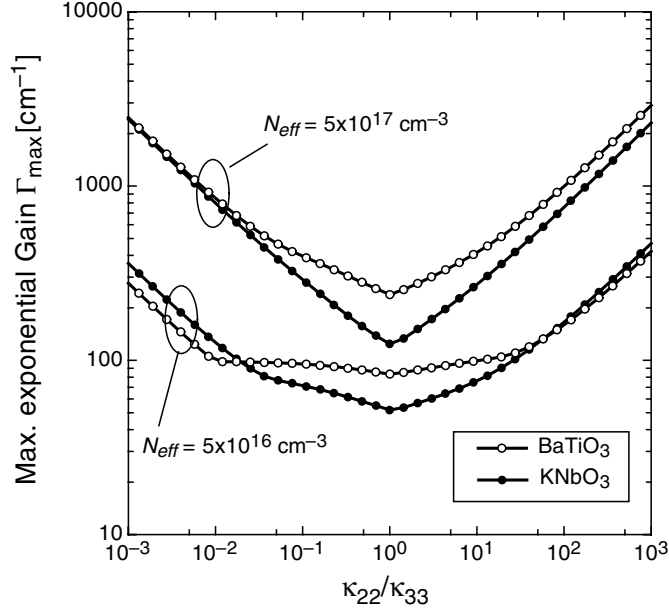
Figure 5.6: Maximum exponential gain $\Gamma \cos \theta_s$ as a function of the photoexcitation anisotropy parameter κ_{22}/κ_{33}. Each point is determined by finding the peak value over all possible two-wave mixing interaction geometries.

crystal from a common surface or from opposite parallel surfaces. The $+z$ direction is defined as being parallel to the direction of the normal to the incidence surface for the S wave ($\hat{\zeta} \equiv \hat{\zeta}_s = (0,0,1)$). Furthermore the absorption is assumed to be moderate ($\alpha_s d \approx 0$, $\alpha_p d \approx 0$ with d being the interaction length), so that we can neglect the absorption terms in the coupled wave equations (5.2).

5.2.2.1   Transmission gratings

Transmission gratings are characterized by the condition $\cos\theta_s \cos\theta_p > 0$, that is, both beams enter the crystal from the same face. By multiplying Eq. (5.4a) by $E_s^* n_s g_s$ and Eq. (5.4b) by $E_p^* n_p g_p$ and inserting the modulation ratio (2.6) one obtains

$$\frac{d}{dz}\widetilde{I}_s \;=\; \Gamma \frac{\widetilde{I}_s \widetilde{I}_p}{G\widetilde{I}_s + \widetilde{I}_p}, \tag{5.12a}$$

$$\frac{d}{dz}\widetilde{I}_p \;=\; -\Gamma \frac{\widetilde{I}_s \widetilde{I}_p}{G\widetilde{I}_s + \widetilde{I}_p}, \tag{5.12b}$$

where it was assumed that $E_{sc} = iE_{sc,i}$. Note that the quantity Γ is the same exponential gain constant as given in (5.9). We recall that the light intensities for the waves are given by $I = cEE^* ng$ with c being the speed of light. The intensities $\widetilde{I}_s \equiv I_s \cos\theta_s$ and $\widetilde{I}_p \equiv I_p \cos\theta_p$ appearing in (5.12a) and (5.12b) correspond to the projections of the Poynting vectors along the surface normal $\hat{\zeta}$ and give the energy flow per unit area through a surface parallel to the input surface. The constant G depends on the geometry of interaction and is defined as

$$G = \frac{n_p g_p \cos\theta_p \left(\hat{e}_s \cdot \overleftrightarrow{\kappa} \cdot \hat{e}_s\right)}{n_s g_s \cos\theta_s \left(\hat{e}_p \cdot \overleftrightarrow{\kappa} \cdot \hat{e}_p\right)}. \tag{5.13}$$
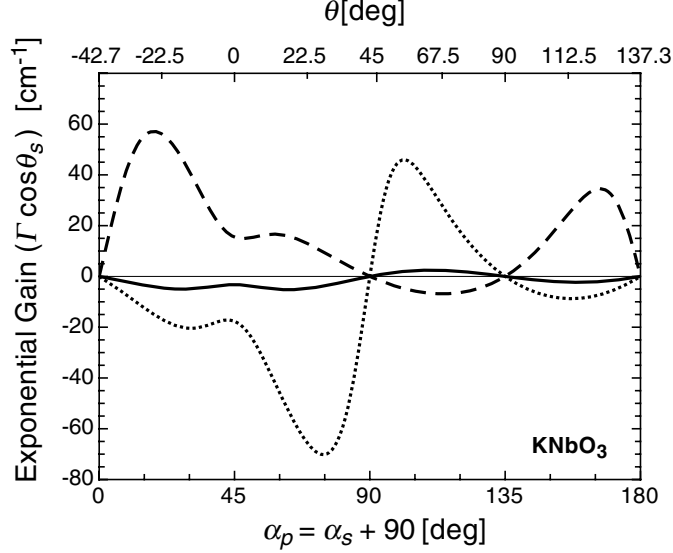
Figure 5.7: Exponential gain $\Gamma \cos \theta_s$ in KNbO$_3$ for geometries for which $\vec{k}_s \perp \vec{k}_p$. Dotted curves are for $\kappa_{22}/\kappa_{33} = 0.1$, solid curves are for $\kappa_{22}/\kappa_{33} = 1$ (isotropic case) and dashed curves are for $\kappa_{22}/\kappa_{33} = 10$. $N_{eff} = 10^{17}$ cm^{-3}.

By summing (5.12a) and (5.12b) one recognizes that the total projected energy flow is conserved, that is $\tilde{I}_s + \tilde{I}_p \equiv \tilde{I}_0$ is a constant. Therefore we have $d\tilde{I}_s/\tilde{I}_s + [G/(\tilde{I}_0 - \tilde{I}_s)]d\tilde{I}_s = \Gamma dz$. Integration of this equation with the boundary conditions $\tilde{I}_s(z = 0) = \tilde{I}_{s0}$, $\tilde{I}_p(z = 0) = \tilde{I}_{p0}$ proper of the transmission grating geometry leads to the solution

$$\chi(z) = \chi_0 \exp(\Gamma z), \tag{5.14}$$

where

$$\chi(z) \equiv \frac{\tilde{I}_s(z)}{\left[\tilde{I}_p(z)\right]^G} \equiv \beta(z) \left[\tilde{I}_p(z)\right]^{1-G}, \tag{5.15}$$

and $\chi_0 = \chi(z = 0) = \left(\tilde{I}_{s0}/\tilde{I}_{p0}\right) \tilde{I}_{p0}^{1-G} \equiv \beta_0 \tilde{I}_{p0}^{1-G}$. Therefore χ is a modified intensity ratio which for $G = 1$ reduces to the conventional intensity ratio $\beta = \tilde{I}_s/\tilde{I}_p$. The evolution of the signal and pump wave intensities can thus be expressed as

$$\tilde{I}_s(z) = \tilde{I}_{s0} \frac{1 + \beta_0^{-1}}{1 + \beta_0^{-1} \left(\tilde{I}_p/\tilde{I}_{p0}\right)^{1-G} \exp(-\Gamma z)}, \tag{5.16}$$

and

$$\tilde{I}_p(z) = \tilde{I}_{p0} \frac{1 + \beta_0}{1 + \beta_0 \left(\tilde{I}_p/\tilde{I}_{p0}\right)^{G-1} \exp(\Gamma z)}. \tag{5.17}$$

Note that, in contrast to the case of two-wave mixing at fixed gratings treated in Sect. 5.1, the above equations do not lead to an oscillation of the light power between the pump and signal waves as a function of propagation distance. Here the energy is always transferred unidirectionally from one wave to the other. A run-over is not possible because in the strong depletion regime the amplified wave dominates and, as a consequence, the photorefractive grating (and therefore the coupling term) becomes very weak due to a small modulation amplitude (2.6).

In absence of photoexcitation anisotropy and for nearly symmetric incidence of signal and pump beams the factor G is always very close to 1, in this case Eqs. (5.16) and
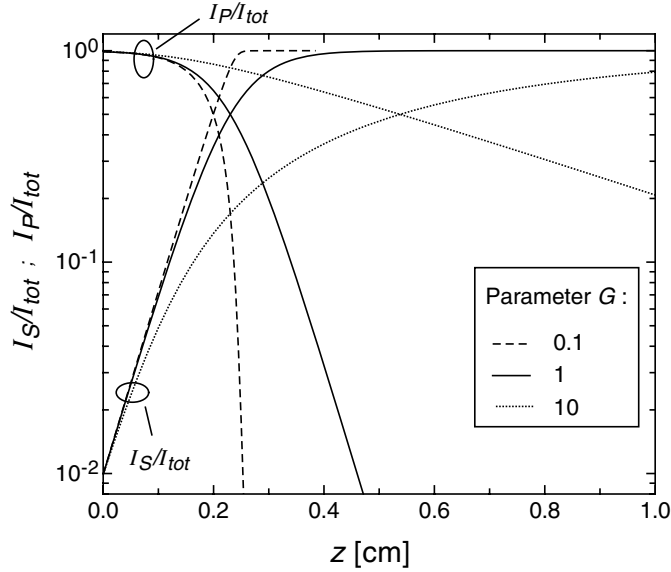
Figure 5.8: Signal wave amplification and pump wave depletion as a function of the propagation distance z in transmission geometry. The normalized intensities $\tilde{I}_s(z)/(\tilde{I}_{s0}+\tilde{I}_{p0})$ and $\tilde{I}_p(z)/(\tilde{I}_{s0}+\tilde{I}_{p0})$ are plotted according to Eqs.(5.16) and (5.17) for $\Gamma = 20$ cm^{-1} and three values of the factor G (Eq. (5.13)).

(5.17) reduce to the well known conventional expressions derived for the isotropic case in symmetric configurations [20]. Note that for the case of transmission gratings considered here the factor G is bound to be positive because the tensor $\overleftrightarrow{\kappa}$ contains only positive elements. We note also that, although for strong anisotropies the factor G may depart significantly from 1, in the above equations the influence of the term $(\tilde{I}_p/\tilde{I}_{p0})^{\pm(1-G)}$ on the beam intensities is still weaker than the one given by the exponential term. However, the corrections brought about by this term are not negligible. The saturation of the amplified signal beam to its maximum value is slower for $G > 1$, and faster for $G < 1$ than for the case $G = 1$. This can be seen in Fig. 5.8 where $\tilde{I}_s(z)/(\tilde{I}_{s0} + \tilde{I}_{p0})$ and $\tilde{I}_p(z)/(\tilde{I}_{s0} + \tilde{I}_{p0})$ are plotted for different values of G and for a common value of the gain Γ. It is worth noticing that in the saturation region the depleted pump wave intensity decreases as $\tilde{I}_p(z + \Delta z) = \tilde{I}_p(z) \exp(-\Gamma \Delta z/G)$, as can be clearly recognized in Fig. 5.8. To get an impression of the possible range for the quantity G in a typical transmission geometry we may take first the example of a BaTiO$_3$ cut along the crystallographic axes and with both interacting beams entering the sample from air through the a-face of the crystal. Considering all possible two-beams interaction geometries in such a configuration we have $0.936 < G < 1.07$ for $\kappa_{22}/\kappa_{33} = 1$, $0.944 < G < 1.06$ for $\kappa_{22}/\kappa_{33} = 0.1$, and $0.43 < G < 2.30$ for $\kappa_{22}/\kappa_{33} = 10$. The ranges for KNbO$_3$ in the same kind of geometry are very similar. For crystals cut under 45 degrees to the crystallographic axes, G varies between $G_{\min} \approx 0.25$ and $G_{\max} \approx 4$ for both $\kappa_{22}/\kappa_{33} = 0.1$ and $\kappa_{22}/\kappa_{33} = 10$.

5.2.2.2   Reflection gratings

In this case the signal and pump wave enter from opposite surfaces and one has $\cos\theta_s \cos\theta_p < 0$. The coupled wave equations (5.4a) and (5.4a) can be brought again exactly in the form of Eqs. (5.12a) and (5.12b) if one allows one of the two projected intensities to take negative values. If we choose the signal wave to propagate towards

positive z and the pump wave to propagate towards the negative z axis, then $\tilde{I}_s(z) > 0$ and $\tilde{I}_p(z) < 0$. Such a negative intensity value reflects the fact that the energy flow for the pump wave is in a direction which is opposite with respect to the considered surface orientation (vector $\hat{\zeta}$). Therefore, as in the above case of transmission gratings, the conserved quantity is still the sum of the (this time signed) intensities and the solution of the coupled equations (5.12a) and (5.12b) is still of the form given by Eqs. (5.14) and (5.15). However, the exponent G (still defined by (5.13)), is now bound to be a negative number. For a plate of thickness L the boundary values are now given at $z = 0$ for the signal wave, and at $z = L$ for the pump wave. Using these boundary values in (5.14) and (5.15) and reintroducing a positive intensity $|\tilde{I}_p(z)| = -\tilde{I}_p(z)$ for the pump wave one can easily find the expressions for the transmitted intensities $\tilde{I}_s(z = L)$ and $|\tilde{I}_p(z = 0)|$, that is

$$\tilde{I}_s(L) = \tilde{I}_s(0)\frac{1 + |\beta_0|^{-1}}{1 + |\beta_0|^{-1}|\tilde{I}_p(0)/\tilde{I}_p(L)|^{1-|G|}\exp(-\Gamma L)}, \qquad (5.18)$$

and

$$\tilde{I}_p(0) = \tilde{I}_p(L)\frac{1 + |\beta_0|}{1 + |\beta_0||\tilde{I}_p(0)/\tilde{I}_p(L)|^{|G|-1}\exp(\Gamma L)}, \qquad (5.19)$$

which are in full analogy to (5.16) and (5.17). The intensity ratio $|\beta_0|$ is defined here as $|\beta_0| \equiv \tilde{I}_s(0)/|\tilde{I}_p|(L)$ and differs from the definition used for transmission gratings. For samples cut along the dielectric axes, symmetric interaction geometries and in absence of photoexcitation anisotropy we have $G = -1$. In this case the two above expressions reduce to the well known conventional relationships [113]. The new correcting factor $|\tilde{I}_p(0)/\tilde{I}_p(L)|^{\pm(1-|G|)}$ brings about a similar influence on the output intensities as in the case of transmission gratings discussed above. Fig. 5.9 shows an example of the G-dependence of the signal and pump output intensities as obtained by solving the above transcendent equations. For fixed gain coefficient Γ an exponent G closer to 0 leads again to faster saturation.

5.2.3   Response time and sensitivity

The photorefractive response time depends on several intrinsic and extrinsic material parameters and on the average photoconductivity of the material. The latter is a function of the power of the interacting beams and of the tensor $\overleftrightarrow{\kappa}$ describing the photoexcitation. In the simplest band transport model and in absence of applied electric fields the response time τ is expressed as

$$\tau = \frac{\varepsilon_0 \varepsilon_{eff}}{e\mu n_0}\frac{1 + K^2/K_e^2}{1 + K^2/K_0^2}, \qquad (5.20)$$

which is Eq. (2.29) combined with (2.27). All the quantities contained in the above equation were defined in Sect. 2.1.2. According to (2.9) and (2.7) the average density of free carriers n_0 can be written as a function of the amplitudes of the two interacting waves, in the case where the pump wave is not depleted we have $n_0 \propto |E_P|^2 (\hat{e}_P \cdot \overleftrightarrow{\kappa} \cdot \hat{e}_P) \tau_R$, where the recombination time τ_R is given by $(\gamma N_{D0}^+)^{-1}$. Therefore the dielectric time $\tau_{die} \equiv (\varepsilon_0 \varepsilon_{eff}/e\mu n_0)$ does depend on the light power, on the polarization of the light waves and on the photoexcitation anisotropy through the free carrier density n_0, in
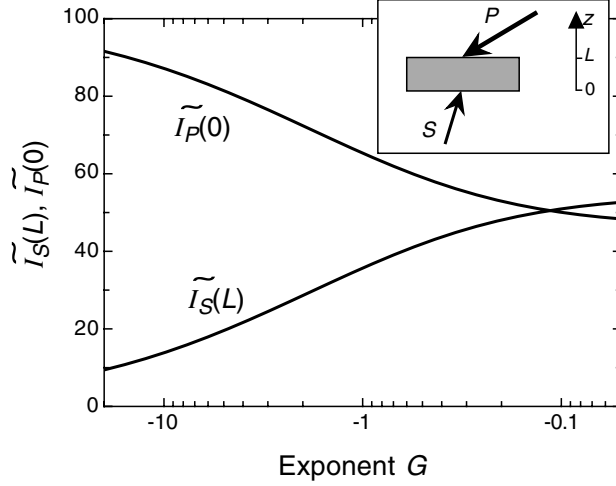
Figure 5.9: Transmitted signal $[\widetilde{I}_s(L)]$ and pump intensity $[\widetilde{I}_p(0)]$ for reflection grating two wave mixing as a function of the exponent G. A value $G = -1$ corresponds to a fully symmetric and isotropic geometry. Parameters: gain coefficient $\Gamma = 20$ cm^{-1}; sample thickness $L = 0.2$ cm; input intensities $\widetilde{I}_s(0) = 1$, $\widetilde{I}_p(L) = 100$.

addition it depends also on the direction of the grating vector $\widehat{K}$ through the effective dielectric constant ε_{eff} and the mobility μ. For the response time τ additional dependencies on the grating direction $\widehat{K}$ are brought about through the quantities K_0 and K_e.

In order to illustrate the expected dependence of the response time on the interaction geometry we take the example of hole conducting BaTiO$_3$ which is characterized by an extremely large anisotropy of the carrier mobility ($\mu_a/\mu_c \approx 20$, [114, 115]). Figure 5.10 shows contour plots for the inverse response time. The values of the dielectric and mobility anisotropies are taken from Ref. [89] and Ref. [115], respectively, while the effective number of traps and the diffusion length (for charge movement along the c-axis) are chosen as $N_{eff} = 10^{17}$ cm^{-3} and $K_e^{-1} = 10$ nm, respectively. We assume to be in the undepleted pump regime so that the photoconductivity is induced uniquely by the pump beam. Fig. 5.10(a) is for $\kappa_{11}/\kappa_{33} = 1$. The fastest response is predicted for $(\alpha_p, \alpha_s) = (180°, 0°)$. This is for two reasons. On one hand the response is faster for counterpropagating than for copropagating beam geometries because in hole conducting BaTiO$_3$ the diffusion length is short [3], and therefore $K_e > K_0$ (see (5.20)). On the other hand the position of the predicted maximum of $1/\tau$ corresponds to a counterpropagating geometry with wavevector $\widehat{K}$ parallel to the a-axis, which is favored with respect to other geometries (such as $(\alpha_P, \alpha_S) = (90°, -90°)$ with $\widehat{K} \parallel c$-axis) because the large increase in mobility for charge movement along a overcomes the disadvantage of a larger effective dielectric constant [1]. Fig. 5.10(b) is for $\kappa_{11}/\kappa_{33} = 10$. In this case the photoconductivity is larger for geometries having the pump wave polarized approximately along the a-axis ($\alpha_p \approx 90°$) and the maximum is observed for a geometry for which the pump and signal wave are propagating nearly perpendicularly. Note that in the two graphs, the absolute values of the inverse response time $1/\tau$ are normalized to the inverse dielectric

---

[1]Note however that, even though a space-charge grating can build up, this particular geometry with the wavevector $\parallel a$-axis does not lead to any photorefractive coupling because the effective electro-optic coefficient vanishes (see Figs. 3.4 and 5.5).
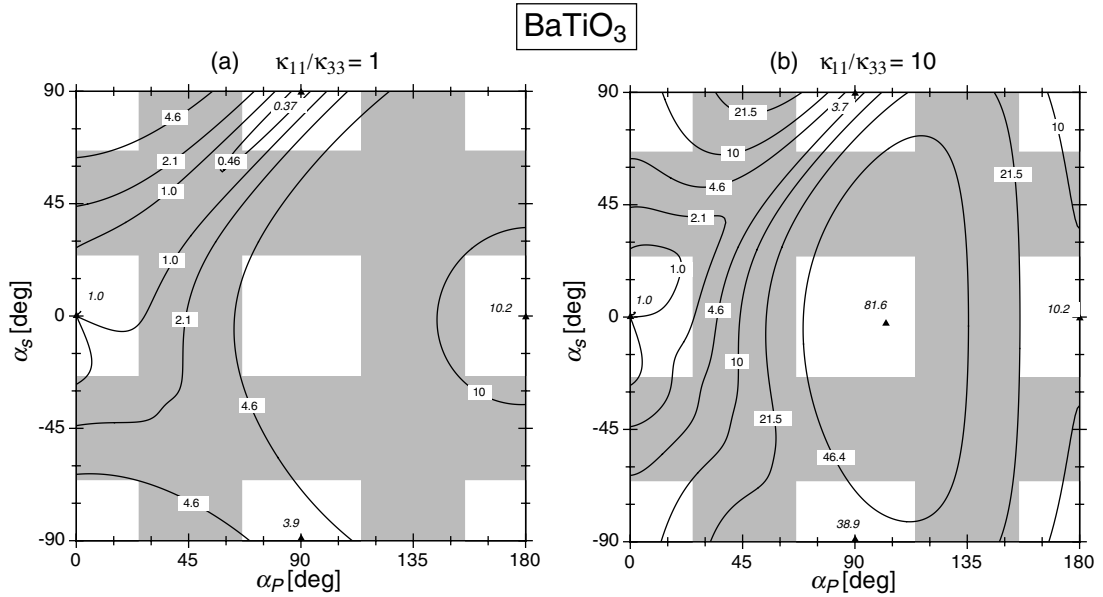
Figure 5.10: Contour plot of the inverse photorefractive response time $1/\tau$ (Eq. (5.20)) for p-polarized beams in the ac-plane of BaTiO$_3$ (undepleted pump). (a) Isotropic photoexcitation, $\kappa_{11}/\kappa_{33} = 1$; (b) anisotropic photoexcitation $\kappa_{11}/\kappa_{33} = 10$; The contour lines are at the indicated logarithmic distances. Parameters: effective density of traps $N_{eff} = 10^{17}$ cm^{-3}, inverse diffusion length in c-direction $K_e^{-1} = 10$ nm. The values of $1/\tau$ are normalized to the inverse dielectric time $1/\tau_{die}$ for a grating pointing along the c-axis ($= 1/\tau(\alpha_p = \alpha_s = 0°)$).

time $1/\tau_{die}(\widehat{K}||c)$ for a wavevector parallel to the c-axis. They are important only to judge the possible dynamic range of the response time among all possible interaction geometries. As might have been expected, the dynamic range increases in the case of anisotropic photoexcitation.

There are several possible definitions for the photorefractive sensitivity. Most of them measure the change per unit time of the refractive index (S_n) or some related quantity such as the square root of the diffraction efficiency [3]. For two-wave mixing, another quantity which is proportional to the material sensitivity is given by the ratio Γ/τ between the exponential two-wave mixing gain and the response time [116]. For crystals following the simplest band model this measure is equivalent to the sensitivity S_n, provided that the photoexcitation tensor is isotropic. In contrast, as discussed in [117] in the anisotropic case significant deviations occur due to the influences of the tensor $\overleftrightarrow{\kappa}$ on the gain and on the response time.

5.2.4 Experimental verification in dichroic KNbO$_3$

The most important new finding of this chapter is the discover of the strong influence of a photoexcitation anisotropy on the photorefractive exponential gain coefficient Γ as evidenced in Eq. (5.9). Since the gain Γ characterizes the wave evolution both in the undepleted and depleted pump regimes, it is important to provide a convincing experimental verification of Eq. (5.9).

For the experimental proof we choose Ni-doped KNbO$_3$, this doping leads to a pronounced dichroism in the absorption spectrum in the green-red spectral region as evidenced in Fig. 5.11. The sample used for the investigations described below has the dimensions $a \times b \times c = 4.6 \times 5.8 \times 6.0$ mm^3. The dopant level in the melt used to

produce the raw boule contained Ni and Nb in an atomic ratio of 3000 ppm. The orthorhombic point group symmetry $mm2$ of KNbO$_3$ allows for three different diagonal elements of the tensors $\overleftrightarrow{\varepsilon}_r^0$, $\overleftrightarrow{\varepsilon}_i^0$ and $\overleftrightarrow{\kappa}$.
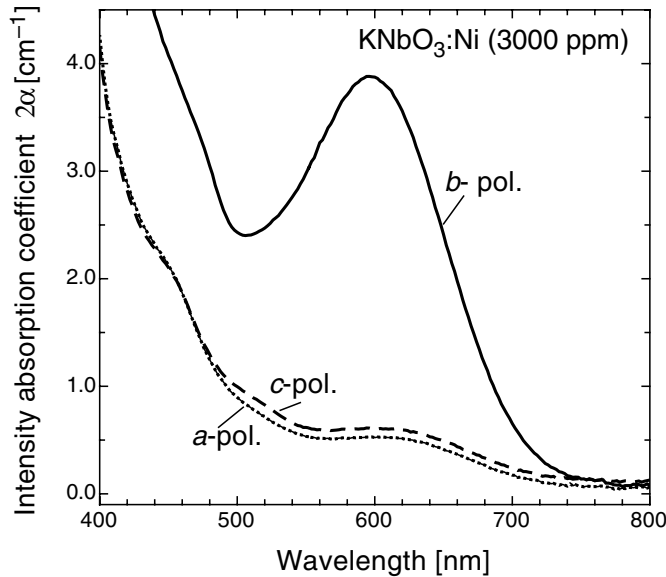

Figure 5.11: Absorption spectrum of Ni-doped KNbO$_3$ for light polarizations parallel to the three crystallographic axes. Note the pronounced dichroism in the green-red region.

The anisotropy of the imaginary part of the dielectric tensor $\overleftrightarrow{\varepsilon}_i^0$ can be determined from the absorption spectra shown in Fig. 5.11. Since the following holographic experiments were performed using Ar$^+$-laser light at the wavelength $\lambda = 514$ nm we are interested only on the absorption constants at this wavelength. These are measured to be $2\alpha_a = 0.77$ cm^{-1}, $2\alpha_b = 2.43$ cm^{-1} and $2\alpha_c = 0.89$ cm^{-1} [2]. The two-wave mixing experiments that will be described below were performed with p-polarized beams propagating in the crystal bc-plane (see Fig. 5.13). Therefore we are actually interested only in the ratio $\alpha_b/\alpha_c = 2.7$. With Eq. (4.38) derived in Appendix A this anisotropy leads to a ratio $\varepsilon_{i,22}^0/\varepsilon_{i,33}^0 = 3.0$ in the imaginary dielectric tensor.

The important quantity that one needs to know is the anisotropy of the photoexcitation tensor $\overleftrightarrow{\kappa}$ not the one of the imaginary dielectric tensor. Therefore one has to verify how these two quantities relate to each other for our crystal. The tensor element κ_{ii} is proportional to the density n_0 of mobile charges photoexcited by light polarized along the crystalline axis i. The density n_0 is directly proportional to the photoconductivity $\sigma_{\mathrm{ph}} = e\mu n_0$, with e being the elementary charge and μ being the carrier mobility. Because the photoconductivity ratio for different light polarizations can be precisely determined experimentally, we can use this ratio to determine the ratio between the diagonal elements of $\overleftrightarrow{\kappa}$. We have performed photoconduction experiments using a holographic technique. A photorefractive grating is recorded by interfering two waves propagating in the bc-plane of the crystal. After recording reaches saturation the grating is optically erased by illumination of the whole grating with a homogeneous beam entering through the polished a-surface of the crystal. The polarization of the erasing beam is adjusted

---

[2]Note that we keep here with the convention (used throughout this work) of designing the absorption constant α as the amplitude absorption constant, therefore the intensity absorption constant get a factor of 2 in their definition.
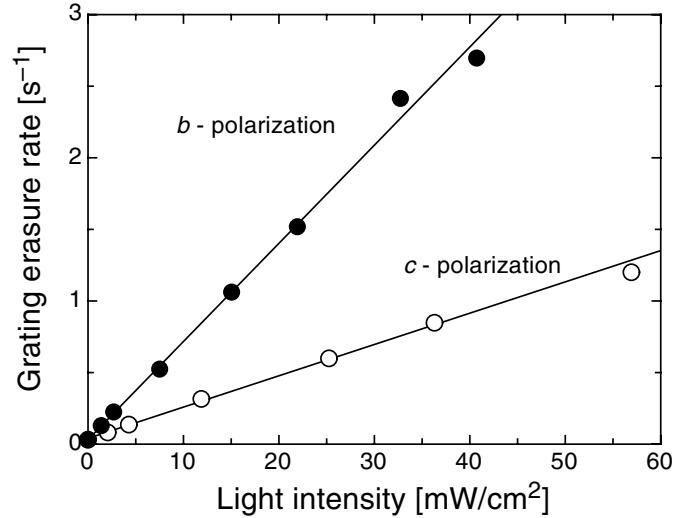
Figure 5.12: Inverse erasure time τ^{-1} vs. the local intensity I of the grating erasure beam ($\lambda = 514nm$). The two sets of experimental points correspond to b- and c-polarization of the erasure light, respectively. From the slopes of the straight lines one determines $\kappa_{22}/\kappa_{33} = 3.4 \pm 0.1$.

alternatively to be parallel to the b- or c-crystal axis. In this way one is able to determine the erasure time for the two light polarizations independently. This is achieved by monitoring the space-charge field decay through the Bragg diffraction of a sharply collimated He-Ne laser beam (λ= 633 nm) propagating parallel to the a-surface. Care was taken that in all the volume probed by the He-Ne read-out beam the erasing light intensity is the same. The decay of the space-charge grating was found to be single exponential as expected from the single carrier charge transport model (2.22). Through Eqs. (2.29) and (2.27) the exponential time constant τ is inversely proportional to the photoconductivity provided that the dark conductivity is negligible. Figure 5.12 shows the results of the grating photoerasure experiments. We find a linear dependence of the inverse erasure time τ^{-1} on light intensity. However, b-polarized light erases the grating much faster. From the two slopes the anisotropy ratio $\kappa_{22}/\kappa_{33} = 3.4 \pm 0.1$ can be extracted. This number is close to the one found above for the anisotropy of $\overleftrightarrow{\varepsilon}_i^0$ and suggests that in our sample the quantum efficiency for photoexcitation of mobile charges deviates only little from isotropy.

Figure 5.13 shows our experimental geometry for two-wave mixing. This interaction geometry is relevant from a technological point of view because it is used in important applications such as laser beam clean-up [118]. The signal beam S enters through the c surface of the crystal under an external angle α with respect to the surface normal. The pump beam enters through the b surface under an angle β. Both beams are horizontally polarized (bc-plane), corresponding to the plane of maximum photorefractive nonlinearity treated throughout the present chapter. In order to keep the wave interaction length under control and avoid unwanted influence of shadow regions at the edges of the crystal the pump beam is collimated in the horizontal direction to a width of 0.95 mm at the entrance face. Its intensity is $150\times$ the one of the signal beam.

In a first set of two-wave mixing experiments we keep the angle γ between the two beams constant and change α and β simultaneously by rotating the crystal sample. Fig. 5.14 shows the measured exponential gain Γ as a function of the angle α for $\gamma = 60°$. The dotted curve is plotted assuming that there is no anisotropy in the tensor $\overleftrightarrow{\kappa}$ in
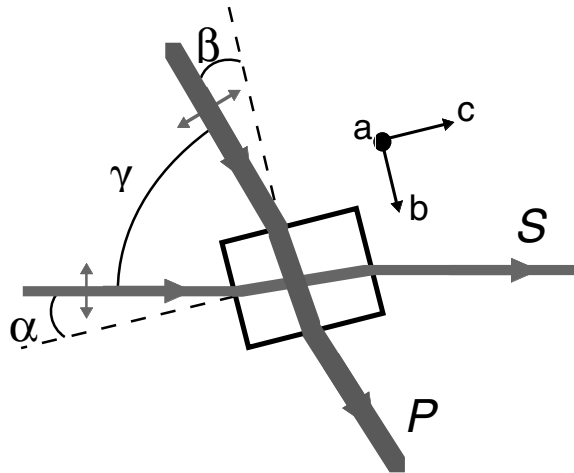
Figure 5.13: Experimental configuration for two-wave mixing in dichroic KNbO₃. The pump wave P amplifies the signal wave S. As drawn here the angles α, β and γ are taken to be all positive so that $\alpha + \beta + \gamma = 90°$.

correspondence with the predictions of the conventional photorefractive theory that takes the light intensity rather than the usefully dissipated energy as the driving quantity [19,20]. As can be clearly seen, these predictions fully disagree with the measurements. In contrast, the solid line describes the measurements very well. This curve is plotted using Eq. (5.9) and the anisotropy $\kappa_{22}/\kappa_{33} = 3.4$ determined above, and with the value of the space-charge electric field $E_{sc,i}$ calculated using the known material properties, i.e. the effective number of traps $N_{eff} = 5.3 \times 10^{16}$ cm^{-3}, determined independently for this crystal [119]. No parameters were adjusted to plot the solid curve. Our theory predicts correctly the point at which the gain crosses zero. This point is a well defined characteristics of the dichroism. While for the conventional models the crossing point should occur whenever the electric field vectors of the two waves are orthogonal (point B in Fig. 5.14), in reality we find it in accordance with Eq. (5.9) at the angle for which $(\hat{e}_s \cdot \overleftrightarrow{\kappa} \cdot \hat{e}_p) = 0$ (point A). In order to clarify this point further we have drawn schematically in the inset of Fig. 5.14) the relative orientation of the important vectors for the crystal orientations corresponding to points A and B.

In the (α_p, α_s) space the experiment described above is performed by moving along the curved trajectory represented by the arrow pointing to the bottom left in the contour diagram of Fig. 5.15. This diagram is plotted using the parameters determined independently above for this crystal [3]. We also performed experiments by following the horizontal trajectory from left to right in the center square of Fig. 5.15. Experimentally this is achieved by keeping the signal beam angle $\alpha = -30$ deg and the crystal orientation fixed while changing the pump wave angle β (see Fig. 5.13). While in the previous experiment performed by rotating the crystal the fringe spacing Λ remained approximately constant, now the grating period varies significantly. The results are shown in Fig. 5.16. Also here the measurements are described very well by the same

---

[3]With respect to the other contour plots of the present chapter, the reduced representation shown here is shifted in the coordinates α_p and α_s in such a way that the interesting accessible square appears in the center of the diagram.
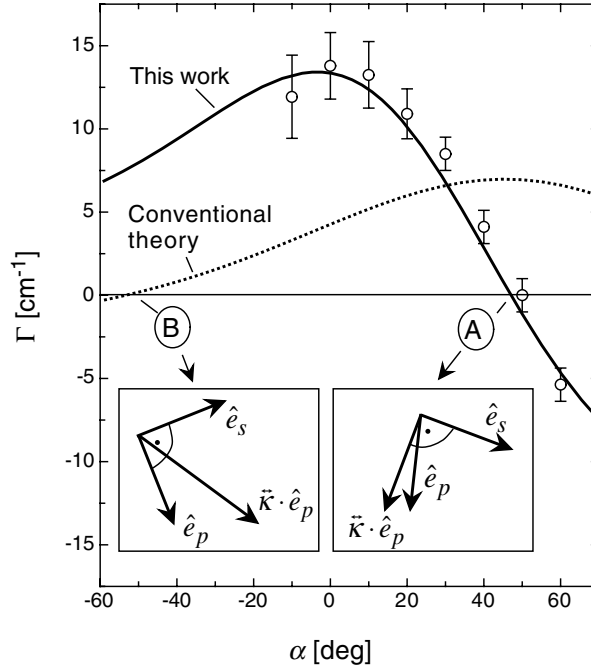
Figure 5.14: Measured two-wave mixing gain Γ (circles) as a function of the angle α for a fixed value of $\gamma = 60°$. Dotted curve: Prediction of conventional theory (Eq. (5.9) with $\kappa_{22}/\kappa_{33} = 1$). Solid curve: prediction of Eq. (5.9) with $\kappa_{22}/\kappa_{33} = 3.4$ determined from the experiment in Fig.5.12. Both curves are plotted using an effective density of traps $N_{eff} = 5.3 \times 10^{16}$ cm^{-3} determined in Ref. [119]. The insets show the orientations of the relevant vectors (all in the same plane) for the two gain zero-crossing points A and B.

parameters as above ($\kappa_{22}/\kappa_{33} = 3.4$, $N_{eff} = 5.3 \times 10^{16}$ cm^{-3}) and no adjustment of parameters is made necessary. Again, the gain expected for the conventional isotropic case (dotted line) disagrees completely with the measurements. The dashed line illustrates the predicted gain if the anisotropy was $\kappa_{22}/\kappa_{33} = 10$ which would lead to a further gain enhancement.

The geometry of Fig. 5.13 used for the above experiments is particularly interesting because, due to the large angle between pump and signal wave, scattering and fanning noise in direction of the signal wave is strongly reduced. For crystal characterization pourposes, however, one usually employs a geometry with both beams entering the sample from the same surface (transmission geometry). In this case the photoexcitation anisotropy brings about quantitative but not qualitative differences with respect to the fully isotropic case. We believe that this is a possible reason why the effects of dichroism have been overlooked until now. Let us consider the example of our crystal in a symmetric transmission geometry with interference fringes having a grating spacing of $\Lambda = 0.4$ μm for which the gain is close to a maximum. If the beams enter through the *b* crystal face, the grating vector is directed along the *c*-axis, and both beams are *p*-polarized, the gain coefficient is *reduced* by about 37% for $\kappa_{22}/\kappa_{33} = 3.4$ with respect to the isotropic case ($\kappa_{22}/\kappa_{33} = 1$). This reduction factor changes only slowly with the beam interaction angle. For this reason we believe that previous manifestations of the effects of material dichroism on two wave mixing might have been erroneously
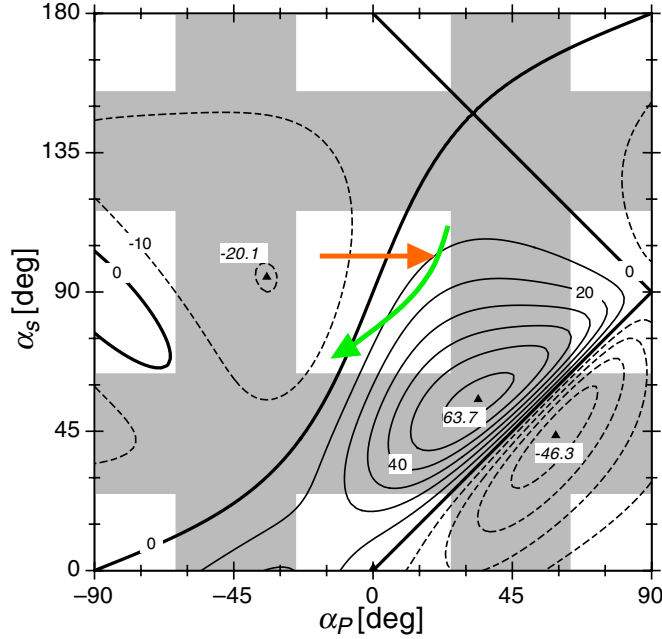
Figure 5.15: Contour plots of the exponential gain Γ for dichroic Ni-doped $KNbO_3$. The experiments of Fig. 5.14 and Fig. 5.16 correspond to the trajectories shown by the arrows pointing to the bottom down and to the right, respectively. Parameters: $\kappa_{22}/\kappa_{33} = 3.4$, $N_{eff} = 5.3 \times 10^{16}$ cm^{-3}. The angle convention is the same as given in Fig. 3.2.

interpreted in terms of electron-hole competition [51, 52], incomplete crystal poling, or partial grating erasure due to surface reflections [120]. These are all effects that can also lead to a reduction of the space-charge field amplitude (see also Chapt. 2). Most materials showing strong two-wave mixing effects, such as $BaTiO_3$ and $Sr_xBa_{1-x}Nb_2O_6$ are strongly anisotropic and are expected to show similar behaviour as shown in this work for $KNbO_3$ crystals.

5.3 Summary

In this chapter we have treated two-wave mixing interaction of plane waves. In the case of fixed transmission phase grating the signal wave shows an oscillatory behaviour as a function of propagation distance analog to what is found for Bragg diffraction. The amplitude of modulation depends on the phase shift between the grating and the modulated light distribution as well as on the input intensity ratio between signal and pump. For an equal value of material optical nonlinearity fixed gratings lead to a stronger amplification with respect to dynamic gratings recorded by the photorefractive effect because the former can be produced with a homogeneous refractive index modulation depth. The drawback is the need for an active stabilization of the interferometric set-up. In contrast, photorefractive phase gratings are self-adapting and therefore particularly interesting for several applications.

We have derived new expressions for the two wave mixing exponential gain Γ and the phase coupling factor δ for the case of anisotropic media. The important role of birefringence and specially of a photoexcitation dichroism on this quantities is clearly demonstrated. The expected gain landscapes for the two-wave mixing interaction are dramat-
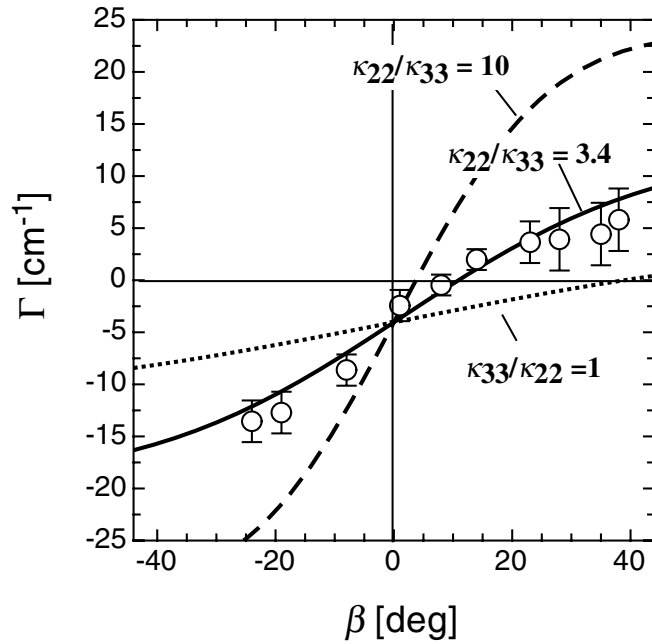
Figure 5.16: Two-wave mixing gain Γ (circles) as a function of the angle β for $\alpha = -30°$. The theoretical curves are plotted according to Eq. (5.9) with $\kappa_{22}/\kappa_{33} = 1$ (dotted line), $\kappa_{22}/\kappa_{33} = 3.4$ (solid line, determined in Fig. 5.12), and $\kappa_{22}/\kappa_{33} = 10$ (dashed line). The latter curve shows the possible gain enhancement for larger anisotropy.

ically modified by these effects as shown by the examples in $KNbO_3$ and $BaTiO_3$ and the experimental confirmation using Ni-doped $KNbO_3$. In materials with an anisotropic photoexcitation an enhancement of the maximum gain coefficient can always be achieved by a proper choice of the interaction geometry. A very interesting geometry for future applications of these phenomena is the one in which two p-polarized waves cross under an angle of nearly 90 degrees. In this case linear light scattering from the pump wave in direction of the signal wave and the related noise are particularly low. For isotropic photoexcitation the two-wave mixing gain in such a geometry nearly vanishes while a significant gain can be obtained in the presence of anisotropy. This opens interesting new perspectives for noise-free coherent image amplification [9, 121–123] and for spatial beam cleanup of high power diode lasers in the near infrared [118, 124–126]. Interestingly, provided that photoconduction still dominates over dark conduction effects, the possible gain enhancement depends only on the ratio κ_{ii}/κ_{jj} of the photoexcitation tensor components for two polarization directions and not on their magnitude. Therefore, if one of the two polarization components is absorbed only very weakly, this ratio can in principle become very large. This situation may be most easily realized in the spectral region which is far from the interband and defect absorption lines. Therefore, in order to exploit this effect for beam cleanup applications, future material research should look for crystals with large anisotropy of the tensor $\overleftrightarrow{\kappa}$ at the operation wavelength, this should be accompanied by a low enough absorption and a strong enough photoconductivity at the power levels of operation.

After describing the geometrical dependence of the two-wave mixing gain coefficient Γ in the general case, we have also analyzed the wave evolution for the case of pump depletion. New expressions valid for the case of anisotropic photoexcitation and/or asymmetric interaction geometries with respect to the surface normal were given both

for transmission and reflection type geometries.

The results presented in this chapter unambiguously demonstrate that the 'usefully dissipated energy' $w(\vec{r})$ (2.2) is the quantity driving the formation of space-charge gratings in photorefractive materials and justify therefore the original choice taken in Chapt. 2. This quantity has to be used instead of the local light intensity $I(\vec{r})$ that was believed previously to take this role.

Chapter 6

Optical processing and wave manipulation by interband photorefractive effects

In this chapter we return to the interband photorefractive effect discussed already in Chapter 2. Due to the superior speed with respect to conventional photorefraction, this effect appears very interesting for applications requiring a large processing speed in parallel or a relatively quick switching time. Three examples are demonstrated here, an optically addressed spatial light modulator (incoherent-to-coherent converter) based on interband photorefraction in $KNbO_3$, a high speed optical correlator based on interband photorefraction in the relatively new photorefractive crystal $Sn_2P_2S_6$, as well as the use of interband effects in $KNbO_3$ to induce reconfigurable light induced 1D waveguides with switching times in the 100 μs region. These three systems are preceded by a short summary on the main experimental findings on band-to-band photorefractive effects in $KNbO_3$ and $Sn_2P_2S_6$.

6.1 Interband photorefractive effects in $KNbO_3$ and $Sn_2P_2S_6$

6.1.1 $KNbO_3$

Potassium niobate has a room temperature band-gap energy of 3.3 eV, therefore near ultraviolet light in the 350 nm region leads to direct transitions between the valence band (related to the $2p$ orbitals of the oxygen ions) and the conduction band (related to the $4d$ orbitals of the Nb ions). The interband photorefractive properties of nominally pure $KNbO_3$ under illumination in the above mentioned spectral range were studied in Refs. [17, 46–49, 127, 128]. Here we mention solely the most relevant features observed under cw illumination at the wavelengths 364 and 351 nm.

- The photoconductivity deviates from a linear dependence on light intensity for intensities of the order of 1 mW/cm^2. Above this level one reaches a regime with square root dependence (see for instance Fig. 2.6), a signature of interband effects.

- The interband gratings are composed by two principal components. The modulated charges giving rise to the first one are energetically located in the two bands and in shallow trap levels with fast thermal exchange with the bands. This component dominates for local light intensities above 50 mW/cm^2 (λ= 364 nm). The second component is composed of a carrier modulation in deep trap levels. It dominates

for local light intensities below 0.1 mW/cm^2 and therefore it is the dominant component far enough from the entrance surface illuminated by the UV light. The average amplitude of the first grating component is about 5 to 10 times stronger than the one of the second one. In undoped crystals and in absence of externally applied electric fields the two components are mutually phase shifted by π. This is evidenced by direct depth resolved Bragg diffraction investigations in transverse geometry [46], by off-Bragg angle Bragg diffraction investigations in longitudinal geometry [47] and by the fact that the effective UV two-wave mixing gain coefficient has opposite signs for low and high wave intensities [47]. With the help of Fig. 6.1 we may discuss the latter point in little more detail. As seen by the fitted curves the trap-free model of Sect. 2.2 describes well the behaviour of the photorefractive gain at large light intensities, where the band grating dominates. However, this model cannot predict the observed zero crossing at low intensities. Inclusion of the charges trapped in deep levels is necessary. A highly simplified model of this kind was recently shown to predict correctly the observed transition with increasing light intensity [48].
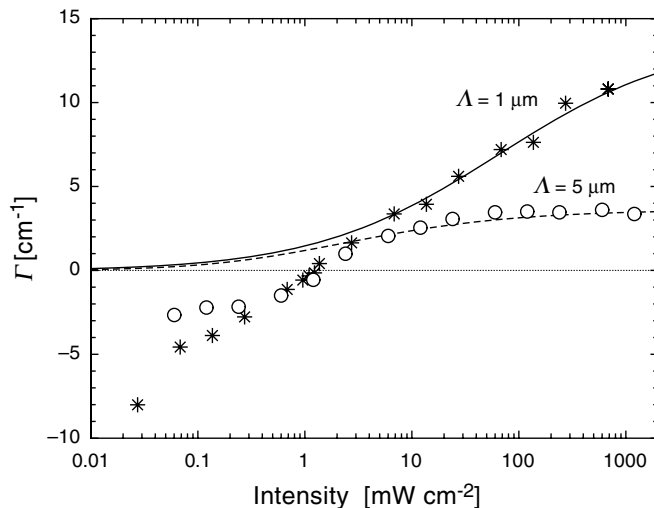
Figure 6.1: Intensity dependence of two-wave mixing gain for interband photorefraction in KNbO$_3$. The curves show the behaviour predicted by "trap-free" model of the interband photorefractive effect (Eq. (2.32)). The zero-crossing point at the intensity of about 1 mW/cm^2 is not predicted by Eq. (2.32) and is due to the fact that at low intensity a deep trap gratings being out of phase by 180 degrees with respect to the free charge grating becomes the dominant component. Electrons are the dominant charge carriers at low intensities and holes dominate at large intensities. $\lambda = 364$ nm, grating vector $\|c$-axis, wave polarization in the bc-plane, modulation index $m=0.11$.

- The average refractive index change modulation Δn obtained by the interband photorefractive effect is few times 10^{-5} and is of the same order of magnitude to what can be reached by conventional photorefractive effects in the same material.

- While the grating component stored in deep traps is affected by below band-gap visible illumination, the free carrier grating component is not. Therefore the near surface grating is extremely robust against optical erasure at wavelengths longer than those used for recording. In KNbO$_3$ we have shown that incoherent visible

light more than five orders of magnitude more intense than the ultraviolet recording beams does not affect significantly the free carrier component of the grating. Interestingly, in several situations the partial erasure of the deep trap component by intense visible light can lead to an enhancement of the measured hologram diffraction efficiency. This is a consequence of the above discussed π-phase shift between the two grating components, which leads to a partial compensation if the second component is not erased.

- At the intensity of 1 W/cm^2 the fast grating component show a build-up and decay time of about 10 μs for $\lambda = 351$ nm and b-polarized light, where the intensity absorption constant is ≈ 5500 cm^{-1}. This response time is increased by less than a factor of 4 for $\lambda = 364$ nm and c-polarized light, which are associated with a 10 times lower intensity absorption constant of 540 ± 50 cm^{-1}. As predicted by theory the response time depends inversely proportional to the square root of light intensity (see Fig. 2.8). Note that the response times for conventional photorefraction in KNbO$_3$ range typically between ≈ 1 ms and few seconds depending on doping and chemical treatment. These are about two to six order of magnitude slower than the interband photorefractive gratings, which clearly proves the interest of the latter for high-speed parallel processing.

- For most samples, at typical intensities of 100 mW/cm^2 ($\lambda = 364$ nm, c-polarization) the grating is found to extend until about 200μm below the illuminated surface, that is about 10 times the $1/2\alpha$ level. The maximum depth can be characterized by the point where the remaining non-absorbed photons are still able to create a photoconductivity larger than the material dark conductivity. Therefore, as expected, the grating depth depends on light intensity, polarization and wavelength. The position of the border between the two regions mutually dominated by the free carrier grating components and by the trapped grating component also depends on these quantities as well as on intrinsic and extrinsic properties of the sample (purity, doping level, ...) [47]. For conditions under which the trapped grating is not being erased significantly the point at which the two gratings components have the same amplitude (but opposite sign) can extend up to about 100 μm below the surface.

- In the framework of the simple model presented in Sect. 2.2 all measurements in pure samples are consistent with an effective mobility for the slowest carrier (electrons) slightly smaller than 10^{-5} cm^2/(Vs). This small value is given by a trap limiting effect due to carriers falling into shallow trap levels (mainly oxygen vacancies) in thermal equilibrium with the band. The effect of shallow traps is not explicitly included in the model of Sect. 2.2 and what is called the "band grating" is in reality a grating induced by carriers sitting in the pseudo-band formed by the true band and the nearby shallow levels [46, 50].

- In principle, due to the strong absorption of the UV light, thermal effects such as direct thermo-optic gratings [129], thermoelectric gratings [130], or gratings induced by pyroelectric space-charge fields [131, 132] could also give a contribution to the observations in diffraction experiments. However, direct experimental verification in several different geometries as well as theoretical estimations of the size of the

effects based on the known material parameters show that none of these effects gives a significant contribution at the cw intensities up to ≈ 1 W/cm^2 relevant for our investigations. Our attempts to detect a possible presence of surface gratings using a reflection type geometry show that also this effect is negligible.

6.1.2 Sn$_2$P$_2$S$_6$

With respect to KNbO$_3$, tin hypothiodiphosphate (Sn$_2$P$_2$S$_6$) is a newer and still less well known electro-optic crystal. The material is ferroelectric below T_C= 66 ^{o}C (monoclinic point group m) [133] and has a large diagonal electrooptic coefficient of ≈ 60 pm/V [134]. The conventional photorefractive properties of Sn$_2$P$_2$S$_6$ are very interesting, specifically due to the high sensitivity in the red and near infrared spectral range [135, 136]. Furthermore, Sn$_2$P$_2$S$_6$ has a lower band-gap energy (≈ 2.3 eV) than KNbO$_3$. It is therefore suitable for interband photorefraction at longer wavelengths.

Investigations of the photorefractive response under interband illumination was performed on Sn$_2$P$_2$S$_6$ crystals grown at the Uhzgorod State University (Ukraine) by the vapour transport technique. Samples of different sizes were cut along the crystallographic axes with the spontaneous polarization nearly parallel to the OX-axis. In our notation the OY-axis is perpendicular to the mirror plane as in Ref. [135]. The absorption spectrum of Sn$_2$P$_2$S$_6$ near the band edge energy and the temperature dependence of the absorption coefficient at $\lambda = 532$ nm are shown in Fig. 6.2. One sees that the absorption edge is situated around the 530 nm wavelength and that, as expected, this edge moves to longer wavelengths for increasing temperature due to a reduced band gap energy.
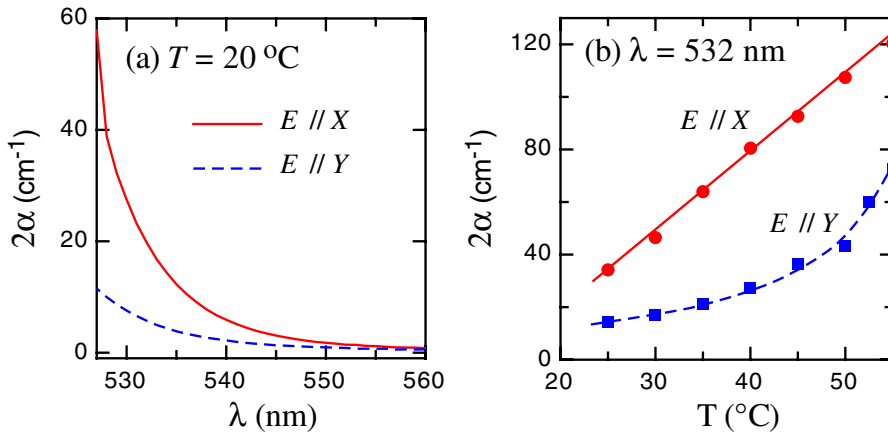
Figure 6.2: Absorption spectra (a) and temperature dependence of the intensity absorption coefficient at $\lambda = 532$ nm (b) for light polarized parallel and perpendicular to the polar X-axis in a Z-cut Sn$_2$P$_2$S$_6$ crystal.

First characterization of photorefractive effects in Sn$_2$P$_2$S$_6$ under cw photoexcitation in the blue-green spectral range ($\lambda = 488$ and 514 nm), that is well within the interband absorption region, were reported in Ref. [137]. Under illumination with plane wave interference fringes refractive index changes up to $\Delta n \approx 10^{-4}$ and response time down to $\tau_1 \approx 3$ μs are observed (p-polarized ($\|OX$) light at $\lambda = 488$ nm, intensity = 0.7 W/cm^2). The response is not single exponential though. A second, about 10 times longer, time constant related to a grating component of similar amplitude does exist. In

general, in terms of refractive index change and sensitivity the performance of $Sn_2P_2S_6$ at 488 nm approaches the one of $KNbO_3$ at 350 nm. However, the grating evolution is more complicated. All experiments point to a photorefractive charge transport nature of the photoinduced gratings [1]. However, details of the charge redistribution and of the exact role played by free and trapped charges, respectively, are not yet fully understood in this material.
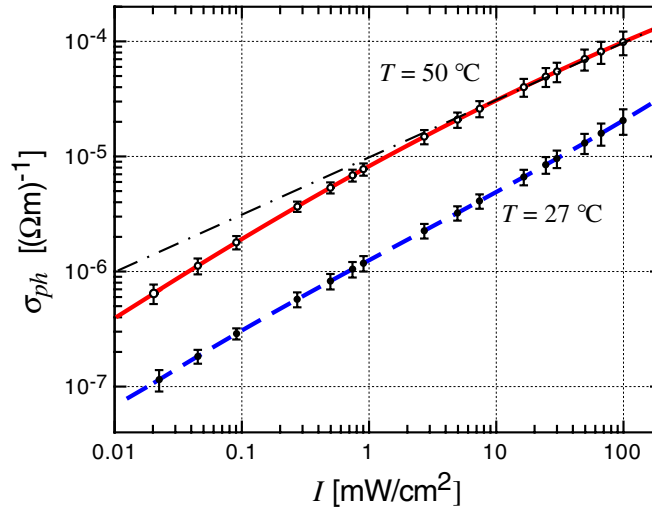

Figure 6.3: Intensity dependence of the photoconductivity σ_{ph} measured under illumination with X-polarized light at $\lambda = 532$ nm in the cw regime. Fresnel losses at the input surface are already subtracted for the value of the incident intensity I.

Due to it's use for the realization of the fast optical correlator described in Sect. 6.3, here we are more interested on the photorefractive response under photoexcitation at the wavelength of 532 nm, which is right at the band-edge of the material. The room temperature intensity absorption coefficient at this wavelength is $2\alpha = 23$ cm^{-1} for X-polarized light and $2\alpha = 7$ cm^{-1} for Y-polarization. As seen in Fig. 6.2(b) these values increase with increasing temperatures, which is expected to lead to a more pronounced interband nature of the photorefractive effect. This hypothesis is confirmed by cw photoconductivity investigations performed using a differential measuring technique described in Ref. [138]. Fig. 6.3 shows the intensity dependence of the photoconductivity for two temperatures. The measurements were performed under an electric field of 200 V/cm parallel to the OX-axis applied through silver painted electrodes and the light (X-polarized) was incident on the Z-surface. The measured photoconductivity is large and reaches about 10^{-4} $(\Omega m)^{-1}$ for an intensity of the order of 100 mW/cm^2. This confirms the efficient photoproduction of free carriers by the band-edge light. At $T = 50$ °C and for a light intensity I larger than 2 mW/cm^2 the photoconductivity σ_{ph} increases with the square root of I, a typical signature of interband effects. For the lower temperature of 27 °C, for which the absorption constant is smaller, the regime for which $\sigma_{ph} \propto I^{1/2}$ is not reached yet at the intensities used here. Therefore at room temperature the grating is expected to be formed by a combination of free and trapped charges already at the

---

[1]A possible alternative is a thermal origin [131, 132] for the observed gratings. However, such a mechanisms can be excluded by considering the size of the effects as well as their geometry and intensity dependence. This conclusion holds also for the gratings induced by nanosecond pulsed at 532 nm discussed below.

illuminated input surface. Note that the dark conductivity σ_d is strongly dependent on the illumination history. Maximum σ_d was measured after pre illumination with the green light (532 nm). In this condition we measured $\sigma_d = 7 \times 10^{-9}$ $(\Omega m)^{-1}$ at room temperature, and $\sigma_d = 9 \times 10^{-9}$ $(\Omega m)^{-1}$ for $T = 50$ ^oC. The big ratio between σ_{ph} and σ_d leads to a low value for the dark intensity (the equivalent intensity for which dark- and photoconductivity are equal) of less than 1 $\mu W/cm^2$. This is very useful because it leads to a large dynamic range for the usable intensities.
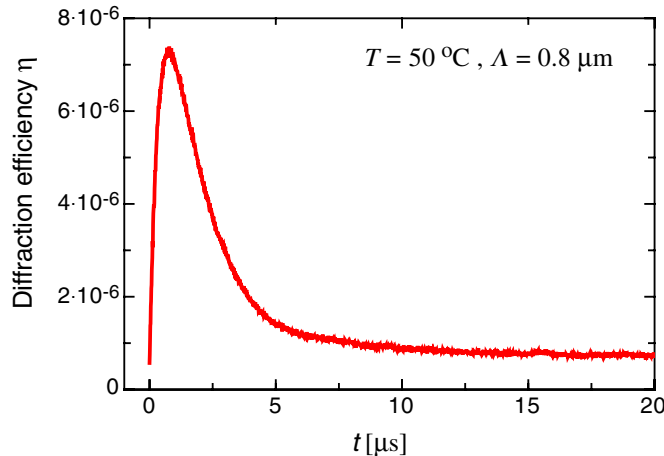
Figure 6.4: Dynamics of the diffraction efficiency in $Sn_2P_2S_6$ under pulsed grating recording at 532 nm. Pulse length = 50 ns; Fluence = 100 $\mu J/cm^2$.

In view of the high repetition rate optical processing task described in Sect. 6.3, at 532 nm we were mainly interested on the photorefractive response under nanosecond pulse excitation. The large optical intensity during the pulse leads to an initial high density of free carriers. As a consequence, at least in the transient regime, interband processes are more pronounced than for the case of cw illumination. In these experiments plane wave holograms were recorded using a Q-switched high repetition rate (up to 50 kHz) frequency doubled Nd:YAG laser ($\lambda = 532$ nm, 50 ns pulse length). The holograms were tested under the Bragg-angle by a weakly absorbed beam ($\lambda = 633$ nm). This geometry is equivalent to the correlator experiment described in Sect. 6.3 if it would be operated with two point images at the input. Figure 6.4 shows an example of the dynamic response obtained by intersecting two horizontally polarized (XZ-plane, grating vector $||OX$-axis) pulses at the temperature of 50 ^oC. The charge redistribution follows the 50 ns pulse and the diffraction efficiency reaches a maximum in a time of the order of 1 μs with a subsequent decay. The full width at half maximum of the response peak is of the order of 3 μs. This width increases only slightly (about a factor of 2) by an increase of the grating spacing by a factor of 10. At room temperature and for a fluence of 110 J/cm2 the response peak width is about 12 μs for $\Lambda = 6.6$ μm and 6 μs for $\Lambda = 0.8$ μm and is therefore slightly larger than at 50 ^oC. The reason for this behaviour is the increase of the photoexcitation cross-section for higher temperatures. This influences also the diffraction efficiency η. The efficiency decreases by about one order of magnitude between room temperature and $T = 50$ ^oC, for instance from $\eta \approx 2 \times 10^{-4}$ to $\approx 2 \times 10^{-5}$ for the grating spacing $\Lambda = 1.6$ μm. The increased absorption for higher temperatures leads to a smaller effective grating thickness and thus to a smaller diffraction efficiency in the longitudinal read-out geometry used here.
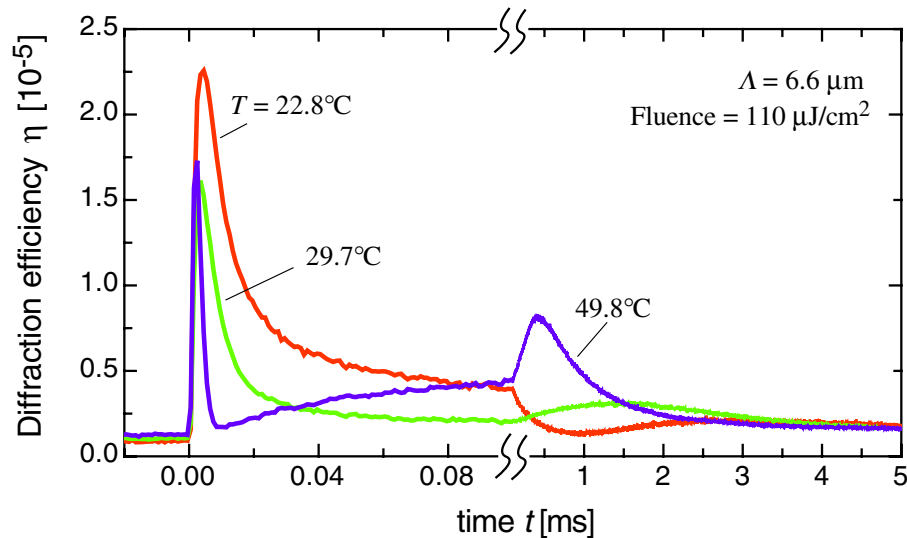
Figure 6.5: Appearance of a trap-induced second peak with slower time constant at large grating spacings. Note the change in time scale in the middle of the abscissa.

It has to be noted that in addition to the fast responding peak described above, at large grating spacing ($\Lambda > 5\mu m$) one observes a subsequent second peak appearing on a much slower time scale of the order of 1-2 ms, as seen in Fig. 6.5. The diffraction efficiency associated with this second peak is lower than for the first one and the value depends on crystal temperature. The appearance of this second peak can be explained by a modification of the model presented in Sect. 2.2 that includes a single trap level in addition to the interband photoexcited free carriers. Numerical simulations based on such a model are able to predict qualitatively the observed dynamics [138]. The fast peak results as being associated with free charges while the second one is related to trapped charges forming a grating phase shifted by 180 degrees with respect to the fast one. The above discussion shows that pulsed photoexcitation has two important advantages with respect to cw one. On one hand we get initially a stronger free carrier grating because of the larger intensity in the pulse (about 2 kW/cm² for the measurement of Fig. 6.4). On the other hand, since the grating dynamics evolution takes place completely in the dark after the pulse, separation of the effects of free and trapped charges is easier than in the cw case.

The above measurements show that pulsed interband photorefractive effects in $Sn_2P_2S_6$ are characterized by a fast response of the order of few μs. We could verify that well distinguished dynamic holograms can be recorded at a pulse rate of 10 kHz or more (see Fig. 6.6). The slower grating seen in Fig. 6.5 and the final slow decaying signal that can be recognized in Fig. 6.4 lead in this case only to a small constant background diffraction. The importance of this background diffraction could potentially be further decreased by using stronger cw read-out intensities, thus effectively erasing the trap grating between subsequent pulses. As seen in Fig. 6.6, for a 10 kHz pulse repetition rate and a pulse fluence of 10 $\mu J/cm^2$ one still measures a differential peak diffraction efficiency of 1.5×10^{-5}. The corresponding full width at half maximum of the diffraction peak dynamics is about 20 μs. These values indicate that, as will be seen in Sect. 6.3, the fast response of $Sn_2P_2S_6$ to pulsed band-edge light is well suited for applications in high rate optical parallel processing.
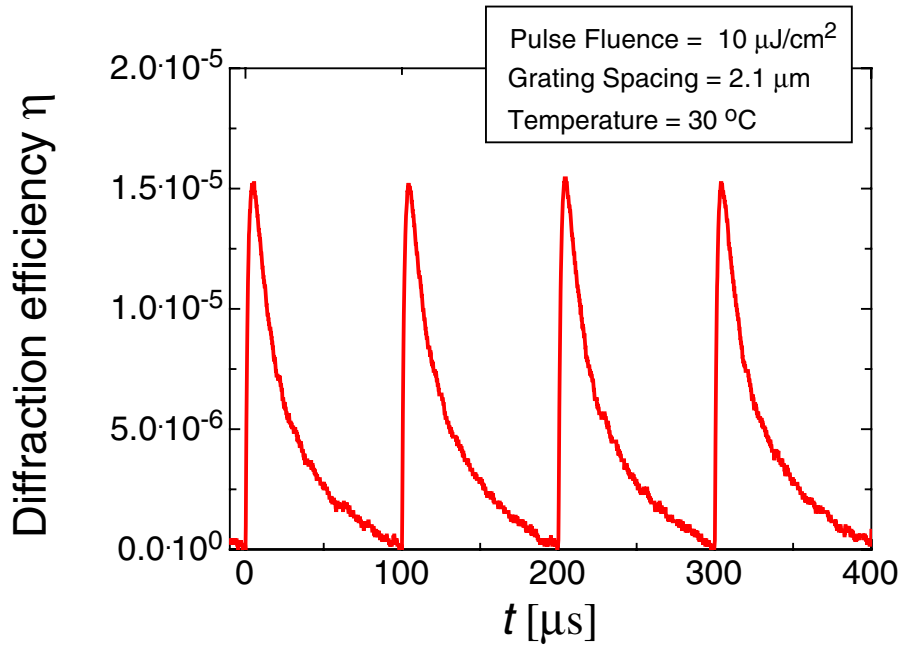
Figure 6.6: Time dependence of the diffraction efficiency for plane-wave holograms recorded in $Sn_2P_2S_6$ with 50 ns long pulses ($\lambda = 532$ nm) at a repetition rate of 10 kHz.

6.2 High-speed optical processing in $KNbO_3$ with high resolution

It has already been pointed out several times that interband photorefractive effects lead to a much increased response speed as compared to conventional photorefraction. If combined with the higher resolution proper of short-wavelength light, this leads to an extremely high effective parallel processing rate. One of the best test benches to demonstrate these properties is a photorefractive incoherent to coherent optical converter (PICOC) operated in the interband regime [139]. A PICOC is basically an optically addressed spatial light modulator based on the photorefractive effect by which an incoherent wave is transferred onto a coherent beam. The key performance characteristics obtained with this test bench can be easily extrapolated to other optical processing devices such as for instance optical correlators.

In a PICOC the information transfer between incoherent and coherent light occurs through diffraction at a modulated holographic phase grating. This approach was realized earlier by using conventional photorefraction [140–144]. The grating is the key element of the device which determines the time response and influences the optical resolution. Resonantly absorbed ultraviolet light not only gives faster response and higher intrinsic resolution. As already mentioned, it also produces gratings which are robust under non-resonant illumination, i.e. they are not affected by light with wavelengths longer than the absorption edge. Therefore, the read-out wavelength λ_{ro}, on which the image is converted, can be chosen inside the whole transparency range of the material with no restriction on its intensity.

The experimental implementation [139] of the interband PICOC is performed with a 47 μm thick sample of nominally pure, single domain $KNbO_3$ crystal. The principle of the set-up is schematically shown in Fig. 6.7. The photorefractive grating is recorded by two interfering s-polarized laser beams at λ_{rec}=364 nm. For this wavelength the
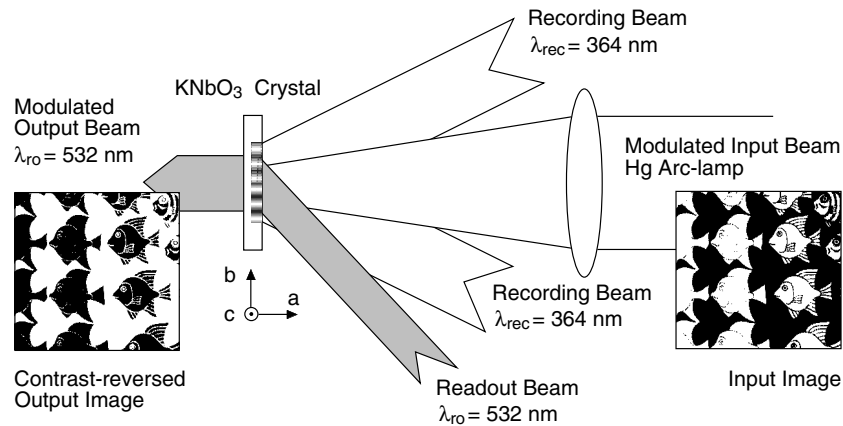
Figure 6.7: Schematic set-up of the implemented Photorefractive-Incoherent-to-Coherent Converter (PICOC). The two recording waves interfere in the crystal to produce a photorefractive grating which is modulated by the projected image carried by incoherent light of the Hg arc-lamp. The read-out laser beam is anisotropically Bragg diffracted and reveals the contrast reversed image on the coherent output beam.

absorption is 2α=540 cm^{-1} [46]. The grating wavevector $\vec{K}$ was oriented along the crystallographic b axis and the grating period Λ adjusted to 0.6 μm. In this geometry the read-out beam at λ_{ro}=532 nm is diffracted anisotropically and perpendicular to the crystal surface. This anisotropic diffraction geometry offers the largest electro-optic coefficient and thus the largest diffraction efficiency. In addition, the fact that the diffracted beam leaves the surface perpendicularly prevents a reduction in resolution that would occur if the incoherent input beam and the coherent output beam would not be colinear [145, 146]. The total intensity of the recording laser beams is set to 85 mW/cm^2 to insure an almost homogeneous interband photorefractive grating throughout the whole crystal depth [47]. The read-out intensity is 5 W/cm^2. Because of the robustness of the interband grating, the wavelength of the incoherent light has to be shorter than the fundamental absorption edge as well. A mercury arc-lamp filtered by a bandpass filter (transmission: 300-400 nm) provides the incoherent light which is first modulated by a resolution chart and then imaged onto the crystal. The image carried by the output wave is finally monitored by a CCD camera.

Before presenting the experimental outcomes it is useful to discuss shortly the parameters limiting the resolution R [2] of such a PICOC. It is well known, that Abbé resolution increases with increasing aperture of the optical projection system. However, at the same time the depth of focus is decreasing. Therefore, if the recording medium or grating has a certain thickness d, the system aperture cannot be made infinitely large. Given the thickness d, optimization of the aperture A for maximum resolution leads to $R \propto \sqrt{n/d\lambda}$ [50]. This limitation comes from pure diffraction considerations for the incoherent input wave and shows that both, a short wavelength λ and a small grating thickness d lead to a better resolution. In addition, the diffraction process at the

---

[2]Two spatially separated bright pixels are resolved when their intensity is at least twice as large as the intensity of the dark pixel which separates them. The resolution R in line pairs per unit length is then given by the inverse of twice the minimum size of the pixels for which the above condition is fulfilled [142, 146].

modulated Bragg grating limits the resolution as well, as was discussed extensively in Refs. [142,145]. Here we calculate the resolution limit due to the finite grating diffraction in a similar way as in [142], however, by taking into account wavelength dispersion and the anisotropic nature of the coupled wave equations discussed extensively in Chapter 4. The curves obtained by this procedure are shown in Fig. 6.8. For a 47 μm thick grating and a read-out wavelength of 532 nm one predicts that the Bragg diffraction process limits the resolution to a maximum of 160 lp/mm. This number is slightly larger than the resolution of 148 lp/mm allowed by the simple projection system for the incoherent illumination.
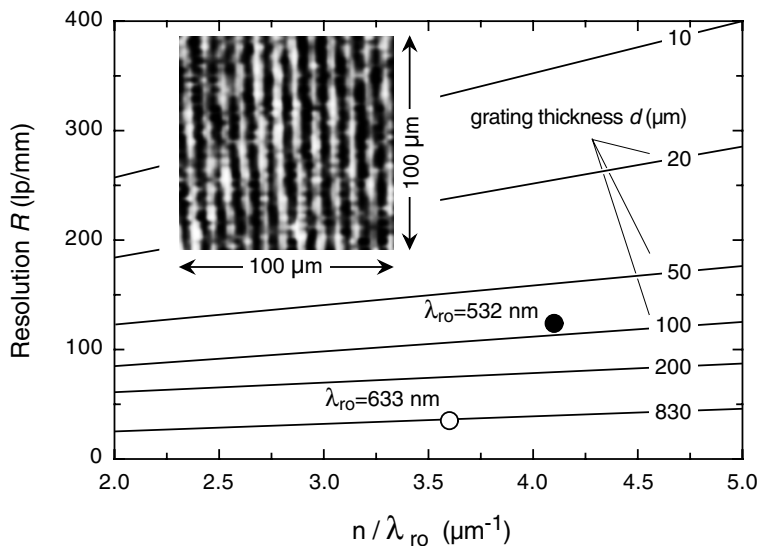
Figure 6.8: Resolution limit R according to Ref. [142] vs. the ratio n/λ_{ro} for different grating thicknesses d in KNbO$_3$. R is defined at 50% of the modulation transfer function, and n is the refractive index at λ_{ro}. The lines are calculated assuming a grating period $\Lambda = 0.6$ μm and a diffraction efficiency of $\eta = 0.01$. ($\bigcirc$) is the resolution measured with a 0.83 mm thick conventional photorefractive grating in Ref. [142] at λ_{ro}=633 nm, ($\bullet$) is measured in this work with a 47 μm thick interband grating at λ_{ro}=532 nm. In the inset, a detail of the converted image obtained with a resolution chart showing the best optical resolution achieved of 124 lp/mm.

In the experiments we find a best optical resolution of 124 line pairs/mm (lp/mm). This value is obtained using an intensity of 70 mW/cm^2 for the incoherent light and is among the best of those achieved with different implementation of optically addressed spatial light modulators (see Table 6.1). For stronger intensities of the incoherent or of the recording waves, the resolution did not show any improvement. We noticed instead an increase of noise due to light scattering at the read-out wavelength. For lower intensities the optical resolution decreased because of a worse image contrast when reducing the incoherent intensity, and because of a reduction of the grating homogeneity [47] when reducing the recording intensity. E.g., with a total recording intensity of 10 mW/cm^2 and an incoherent intensity of 70 mW/cm^2, the resolution fell below 96 lp/mm.

As mentioned earlier, the interband PICOC is interesting not only because of the achievable resolution, but also because of its short build-up and reconfiguration time. For the experimental parameters giving the maximum resolution we measured a response time of 35 μs with an overall contrast better than 10:1 (Fig. 6.8) and a diffraction

efficiency of $\eta = 0.4\%$. For increasing intensities the speed and the diffraction efficiency increases. As shown in Fig. 6.9a, stronger incoherent intensities accelerate the recording, i.e. the time needed to modulate the grating, while no influence is noticed on the recovery time needed to restore the original homogeneous grating. The recovery time is governed by the recording intensity (Fig. 6.9b).
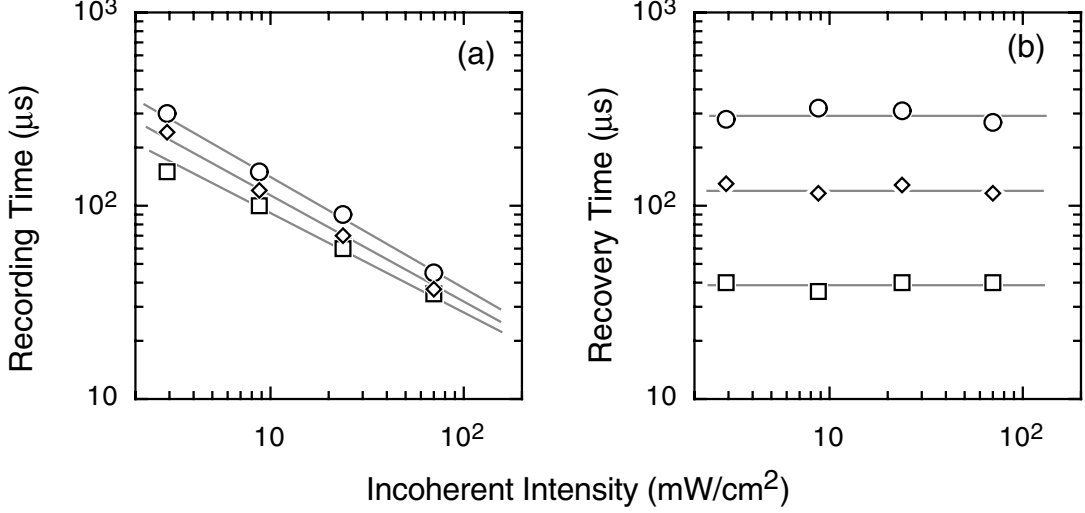

Figure 6.9: Dependence of the recording time (a) and of the grating recovery time (b) on the incoherent intensity for different recording intensities I_{rec}: ($\bigcirc$) 8 mW/cm^2, ($\Diamond$) 25 mW/cm^2, ($\square$) 85 mW/cm^2. The lines are guides to the eye.

The write-read-erase cycle of 70 μs achieved with the present approach is almost as fast as for multiple quantum well (MQW) structures and much faster than spatial light modulators (SLM) based on ferroelectric liquid crystals (FLC) which show responses of typically 1 ms. In our case, speed and resolution combine to give, to our knowledge, the highest incoherent-to-coherent conversion rate $\Gamma \equiv (2R)^2/\tau = 88$ Gbit/(s cm^2) demonstrated to date in cw regime (Table 6.1).

The PICOC implementation discussed here is also energetically very competitive. By defining the optical switching energy per bit as

$$\mathrm{En/bit} \equiv (I_{rec} + I_{inc})\frac{\tau}{2R^2}, \qquad (6.1)$$

we obtain En/bit = 0.5 pJ, one of the smallest values measured in optically addressed SLM's as reported in Table 6.1. However, this figure does not consider the readout intensity I_{ro} and the output power in the coherent beam carrying the image. An appropriate figure of merit is then given by pp_{in}/pp_{out} i.e., the number of total input photons per pixel necessary to generate one photon per pixel at the output [147]. For our experiment this is expressed by

$$pp_{in}/pp_{out} = \left(\frac{3}{\eta}\right)^{1/3}\left[\frac{(2R)^2 h\nu_{ro}}{I_{ro}\tau}\right]^{1/3} \times$$
$$\left[\frac{\tau}{(2R)^2}\left(\frac{I_{rec}}{h\nu_{rec}} + \frac{I_{inc}}{h\nu_{inc}} + \frac{I_{ro}}{h\nu_{ro}}\right)\right], \qquad (6.2)$$

where I and $h\nu$ are the intensities and the photon energies of the recording (*rec*), the incoherent (*inc*), and of the read-out (*ro*) waves. This figure has to be minimized and

allows to compare the performance of the converter with optical correlators. In fact, a PICOC can also be used as a correlator by directly modulating the recording waves with the object and the reference images and by placing the crystal in the Fourier-plane. The diffraction of the read-out beam would reveal the correlation function of the two input images in the object plane. With Eq. (6.2), we obtain $pp_{in}/pp_{out} = 5 \times 10^5$ for our PICOC-correlator, a value which compares well even with correlators implemented in vapor gases [147, 148].

Table 6.1: Comparison of selected optically addressed SLM's operated in the diffraction (D) or transmission (T) mode. The quantities are defined in the text. For this work, the values of R, τ_c, and η correspond to a single measurement. For most of the other cases these three quantities have been extracted from distinct experiments.

Optical - Modulating sensor - material	R $(\frac{lp}{mm})$	τ_c (ms)	η (%)	Γ $(\frac{Gbit}{s\,cm^2})$	En/bit (pJ)	$\frac{pp_{in}}{pp_{out}}$	Ref.
pure KNbO$_3$	124	0.07	D=0.4	88	0.5	$5 \cdot 10^5$	this work, [139]
Fe:KNbO$_3$	35	100	D=1.2	0.005	10^3	$4 \cdot 10^8$	[142]
BSO thin film	27	10	T=3.8	0.03	170	10^7	[149]
GaAs PROM [a]	17	2	T=70	0.06	175	$4 \cdot 10^6$	[150]
bacteriorhodopsin	100	100	T=1	0.04	10^4	$8 \cdot 10^7$	[151]
GaAs-AlGaAs MQW [a]	70	0.035	D=1.5	56	0.2	$3 \cdot 10^5$	[152]
a-Si:H - FLC [a]	150	2	D=0.2	4.5	0.02	10^6	[153]
Si diodes - LC (nem.) [a]	70	16	-	0.12	0.3	-	[154]
Sn$_2$P$_2$S$_6$ [b]	32	0.1	D=10^{-5}	4.1	20	$2 \cdot 10^7$	this work, [155]
Cs atom vapor [b]	15	-	D=$7 \cdot 10^{-4}$	-	-	10^4	[147]

[a] Operated with an external voltage. [b] Operated as correlator.

Table 6.1 summarizes performance characteristics of selected OA-SLM implementations. The reported values do not always reflect the best limiting performances achievable when the parameters are singularly optimized, but they correspond to the best global results obtained through a single measurement. The values have been chosen trying to optimize the conversion rate and the energetic aspects. One can conclude that a PICOC based on the interband photorefractive effect can be competitive with devices based on semiconductor MQW or on liquid crystals. It is faster than liquid crystal devices and is more versatile with respect to devices based on MQW's because the readout wavelength does not need to be chosen in a narrow spectral range corresponding to the excitonic resonance.

The resolution, optical energy budget and versatility of the incoherent-to-coherent optical converter discussed in this section proves that interband photorefractive effects are very well suited for parallel optical processing at low intensities. In the next section we describe a further example where one makes use of these properties for the demonstration of a high repetition rate optical correlator using Sn$_2$P$_2$S$_6$. Figures for this optical processing element were included in Table 6.1 as well.

6.3 High frame rate joint Fourier transform correlation in Sn$_2$P$_2$S$_6$

If an optical correlator has to compete with the steadily improving purely electronic alternatives its operation frame rate has to be high enough. Figure 6.10 compares the

processing time required to compare two images by dedicated electronic devices[3] and by the approach taken in this section. Clearly, if the linear input dimension is smaller than approximately 50 pixels an optical correlator that processes all pixels in parallel would need to be operated with a cycle time not exceeding 100 μs per frame.
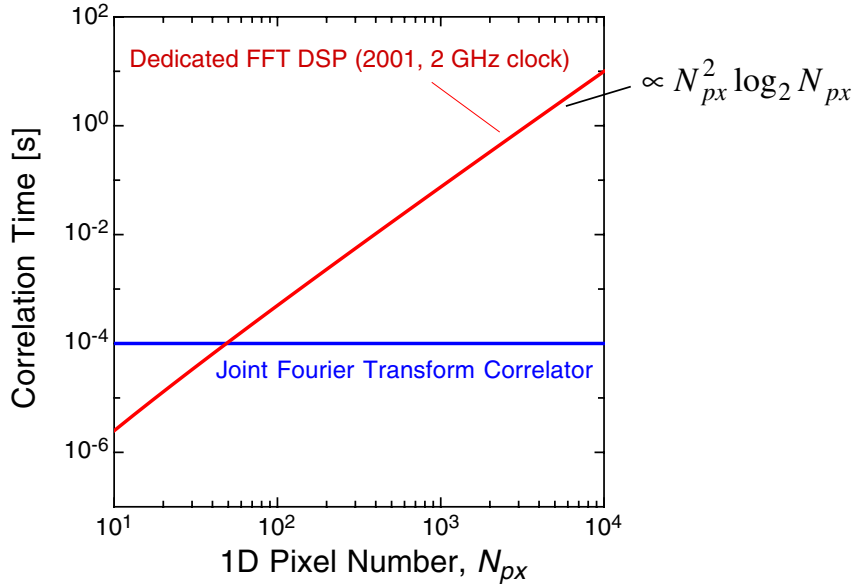

Figure 6.10: Processing time required for calculating the correlation between two images of size $N_{px} \times N_{px}$. A JFT optical correlator with 10 kHz frame rate is faster than a 2 GHz clock rate state of the art dedicated digital processor as long as the number of pixels exceeds $N_{px} \approx 50$.

In the past the speed of optical correlators was often limited by the input electronic interface device, such as the input spatial light modulator (SLM) used in one or both arms of the joint Fourier transform (JFT) scheme first proposed by Weaver and Goodman [156]. Today, the advent of faster display devices such as ferroelectric liquid crystals SLM's has shifted the limiting factor back to the nonlinear device element [157]. It is therefore important to provide a material where the optical processing operation can be performed at a rate at least equal to the input data rate. Among the low-power nonlinear optical effects coming into consideration, the interband photorefractive effect discussed in this chapter is particularly attractive because of the high sensitivity and speed and because the relatively small thickness of the recorded gratings leads to higher spatial resolution and an increased shift invariance of the correlator. As discussed in Sect. 6.1 for the green spectral range the material of choice to obtain highly sensitive interband photorefractive gratings is $Sn_2P_2S_6$.

Here we use $Sn_2P_2S_6$ as nonlinear optical processing element performing fast JFT correlation operation. The system is operated in the pulsed regime using a high repetition rate frequency doubled Nd:YAG laser at the wavelength of 532 nm. The main features of the pulsed band-edge photorefraction at this wavelength were described in Sect. 6.1. The optical system consists of an angularly multiplexed holographic storage memory cascaded to the $Sn_2P_2S_6$ dual axis JFT correlator. The principle of operation is schematically shown in Fig. 6.11. The use of the holographic memory permits to

---

[3]such as a 2001 generation Texas Instruments TMS320C82 or TMS320C80 digital signal processor.

overcome the available speed of the electronic/optic interface device and to operate the JFT correlator at a rate of 10 kHz.
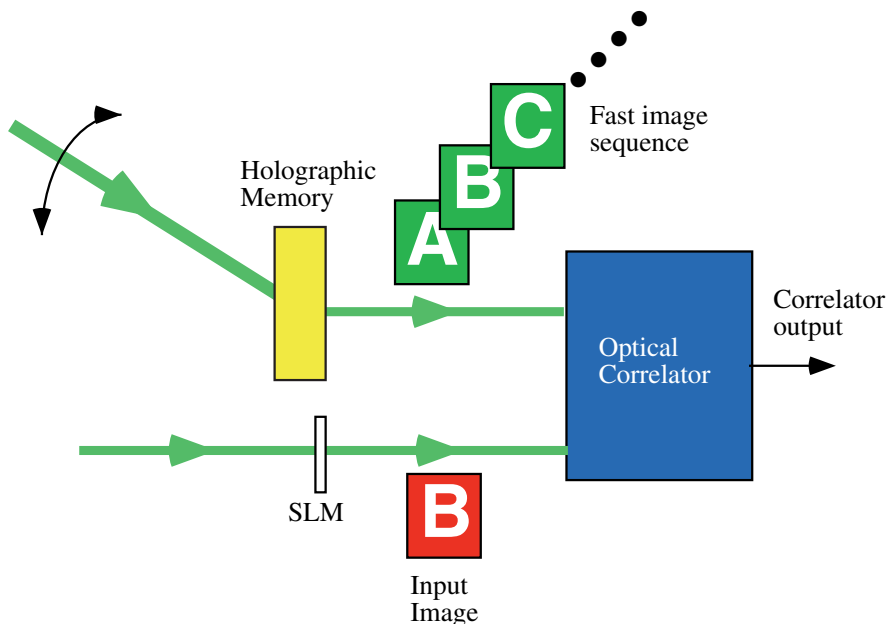

Figure 6.11: Principle of operation of the high rate JFT correlator.

A schematic view of the setup is shown in Fig. 6.12. The left upper part is the holographic storage memory stage used to provide a fast image template sequence. In the lower right part the two arms of the dual axis JFT correlator cascaded to the memory can be recognized. The collimated laser light enters the setup at top left. The beam is divided by a polarizing beam splitter. The transmitted part is reflected by a galvanic scanner, which is used to produce the reference wave of the angular multiplexed holograms. The other beam is modulated and reflected by a ferroelectric liquid crystal spatial light modulator (SLM) with 256 x 256 pixels (Displaytech Inc., pixel size = 17 μm) that acts as an array of switchable half-wave plates. After modulation the image beam passes the beam splitter for the second time and is imaged inside the LiNbO$_3$ crystal which acts as holographic storage medium. In the arrangement chosen in our experiment the image pixels are modulated in phase but there is no modulation in intensity (binary phase images). The library images are recorded in the angularly multiplexed holographic memory by the incremental recording scheme [158, 159] with about 100 writing cycles, which guarantees holograms with equivalent diffraction efficiency. This part of the set-up can also work as a Vander Lugt type correlator if the holograms are read out with the image beam [160]. Examples of images recovered from the memory stage of the set-up are shown in Fig. 6.13. In order to permit direct observation, in this particular case the images were recorded in the amplitude rather than in the phase domain. By synchronizing the laser pulse train and the galvanic mirror movement by means of a digital word generator, a read-out frame rate of 50 kFrames/s was achieved. This number is limited by the available repetition rate of our laser.

In the JFT implementation the reconstructed images from the static hologram are reflected by two mirrors and are Fourier transformed by the upper FT lens ($f = 250$ mm) to the location of the nonlinear Sn$_2$P$_2$S$_6$ crystal. The second input beam of the
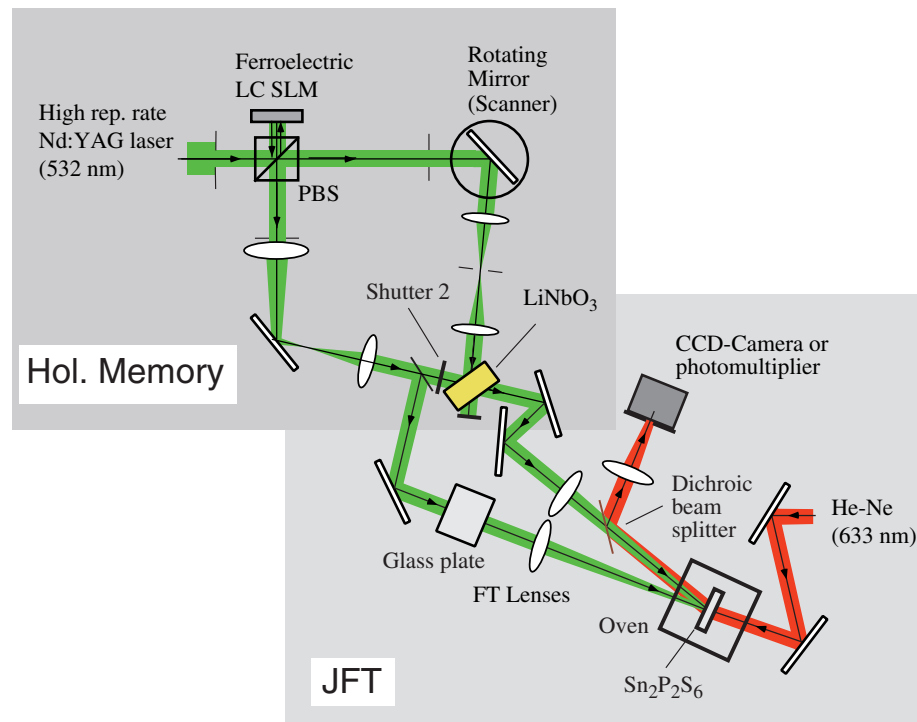
Figure 6.12: Scheme of the set-up for the joint transform correlator.

correlator is derived from the original image beam of the storage system by the beam splitter placed in front of shutter 2. The paths length of the two arms are adjusted in order to produce exactly overlapping Fourier transforms patterns of the input objects on the incidence surface of the $Sn_2P_2S_6$ crystal. A thick glass plate (25 mm) compensates the 10 mm thick $LiNbO_3$ crystal and ensures mutual coherence between the waves propagating in the two arms. The gratings written by the green input beams are read out with the expanded and collimated beam of a cw He-Ne laser ($\lambda = 633$ nm , 10 mW power). The read-out angle matches the Bragg condition of the grating ($\Lambda \approx 3.3$ μm) written by the zero-order Fourier components of the input beams. The diffracted read-out beam is extracted using a dichroic beam splitter and Fourier transformed into the correlator output plane. The intensity distribution on the output plane can be detected by a CCD-camera, in alternative the central peak can be selected by an aperture and detected with a photomultiplier.

The system is operated in two steps. First the images are stored holographically in the $LiNbO_3$ crystal. In a second step the object beam is stopped by shutter 2, and the image to be correlated with the stored images is displayed on the SLM. The correlation between the input wave from the SLM and the read-out wave from the holographic memory will build up in the output plane. High speed image sequences were produced by reading-out 10 phase modulated Escher-images [161] of the kind shown in Fig. 6.13 at a rate of 10'000 frames/s from the holographic memory. The total energy of the image sequence incident on the $Sn_2P_2S_6$ was 200 nJ per image, whereas the pulse energy coming from the SLM was 800 nJ. The polarization of the beams was vertical ($||Y$) and $T = 27$ °C. The intensity of the correlation peak was selected using a pinhole. Two typical correlation traces are shown Fig. 6.14. The 10 mutual correlation peaks can be clearly identified. Peak 4 in (a) and peak 10 in (b) are the highest. They correspond to the correctly identified images that were displayed on the SLM. The height of the peaks
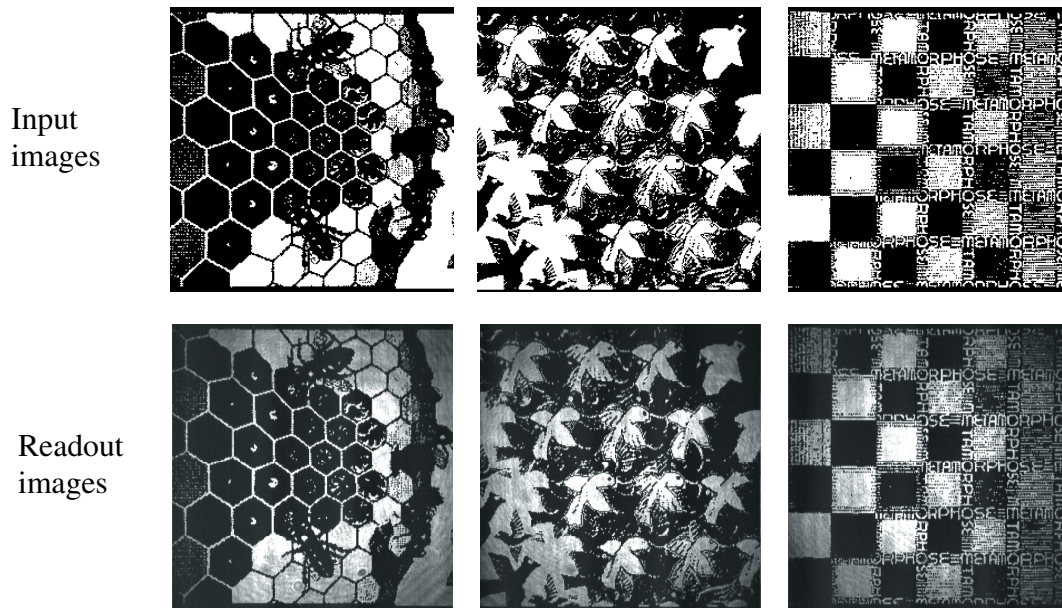
Input images

Readout images

Figure 6.13: Digitized input images and images retrieved from the holographic memory stage. Three out of 100 stored amplitude modulated images are shown.

corresponding to the non matching images are however higher than expected by theory. This is related to the limited usable aperture (4x4 mm^2) of the available Sn$_2$P$_2$S$_6$ crystal, which acts as spatial low pass filter on the input images. The height of the correlation peak was in fact particularly low for input images showing high spatial frequencies (like image number 1 in our case). An important figure of merit for light driven SLM's is the switching energy per pixel, which is about 20 pJ/pixel for the correlator described here. This is less than two orders of magnitude higher than the best values found previously for semiconductors, multiple quantum wells, and interband operated KNbO$_3$ devices (see Table 6.1).
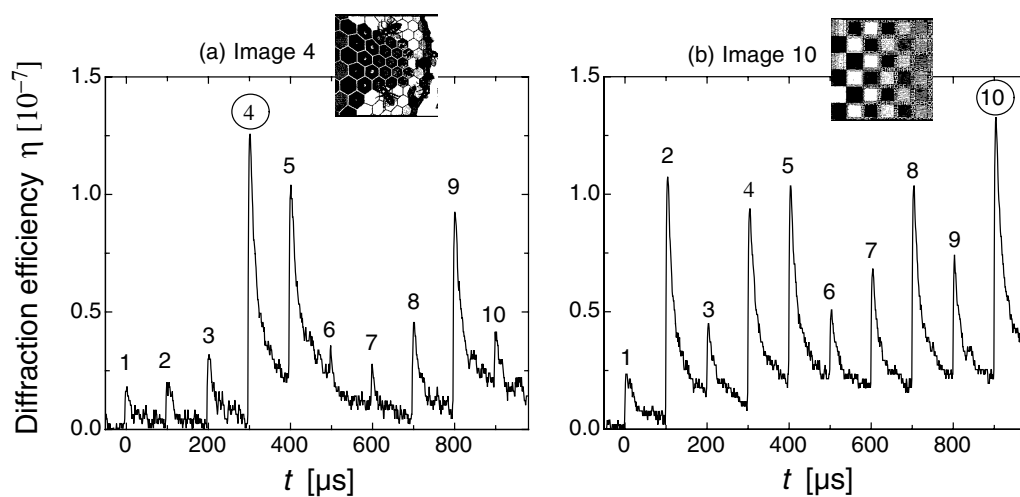

Figure 6.14: Intensity of the correlation peaks produced by comparing image 4 (a) and image 10 (b) with an image sequence extracted from the holographic memory at the rate of 10 kHz.

In summary, in this section it was shown that, by a combination of a holographic memory with fast dynamic holography in Sn$_2$P$_2$S$_6$, realization of a joint Fourier trans-

form optical correlator working at a frame rate of 10 kHz is possible. To our knowledge, this is the highest correlation rate demonstrated to date in a photorefractive JFT correlator. The corresponding processing speed also exceeds the performance of current electronics (see Fig.6.10). Typical applications of such correlators are pattern and position recognition (fingerprints, faces, industrial tools, objects, ...), tracking of unknown objects or search in large databases of page coded information.

6.4 Reconfigurable light-induced waveguides in KNbO$_3$

Optical waveguides play a key role in the field of optoelectronics. In crystalline materials, waveguides can be fabricated by various techniques, including ion in-diffusion, ion exchange, ion implantation, etching, and epitaxial thin film deposition [162–164]. For some applications such as optical switching or dynamic optical interconnection, reconfigurable waveguides are desirable. A further advantage would be achieved if the fabrication step could be fully omitted. We show here a technique based on the interband photorefractive effect by which a one-dimensional waveguide is created in real-time by means of light illumination only [165]. The waveguide shape reflects the spatial distribution of a top surface illumination and can be reconfigured in a time of few tens of microseconds [4].

So far, waveguide formation by means of the conventional photorefractive effect [166, 167] has been demonstrated either with the combined effect of multiple exposure illumination of aligned focused spots [168, 169], or by using the self-induced channel generated by a self-focused or spatial soliton beam [170, 171]. These approaches make use of the conventional photorefractive effect and are therefore associated with a relatively slow response time. Waveguides formed by spatial soliton beams are also critically dependent on the beam intensity and on the exact self focusing conditions. In addition, except for a small bending due to charge diffusion effects, soliton induced waveguides are essentially straight, which precludes the possibility of constraining light propagation along an arbitrary path.

In our case the mechanisms underlying waveguide formation is the local screening of an external electric field E. This is analogous with the mechanisms acting in the case light induced waveguides are produced by beam self-focusing [170] or light induced domain switching [172]. Using an electro-optic crystal, if the light polarization and field direction are chosen properly, the refractive index decreases homogeneously across the sample apart for the regions which are externally illuminated. There the field is screened by bipolar charge transport. Because the desired structure can be imaged onto the surface by a deflector or a photo-lithographic like process, various waveguide configurations can be easily produced in this way.

A schematic view of the setup used to produce the light induced waveguides in KNbO$_3$ is shown in Fig. 6.15. A pure, single domain crystal of dimensions $a \times b \times c = 13.8 \times 3.9 \times 7.3$ mm^3 is used for the experiments presented below. The field is applied along the c-axis using silver paste electrodes. A mask with a slit width of 100 μm was homogeneously

---

[4]It is possible to implement the technique presented below building on the conventional instead of the interband photorefractive effect, however, at the cost of a much longer response time.
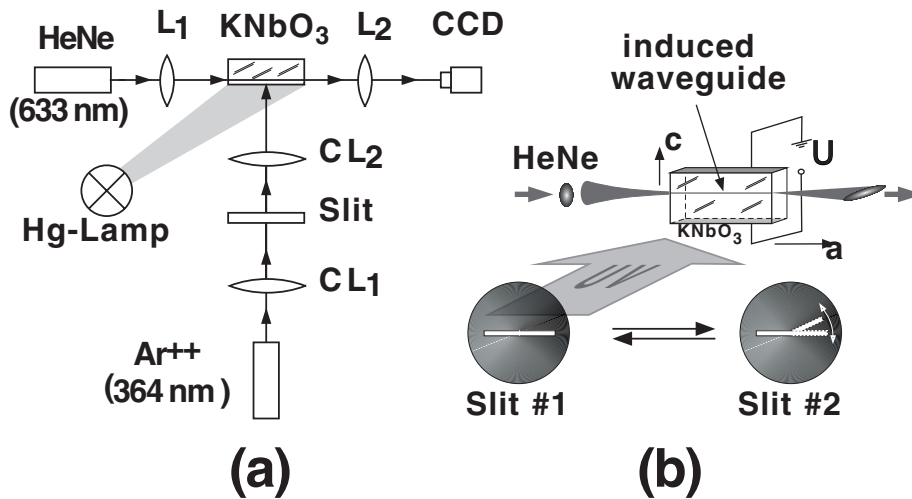
Figure 6.15: Schematic top (a) and front view (b) of the experimental setup for creating light induced waveguides. L_1 and L_2, and CL_1 and CL_2 are spherical and cylindrical lenses, respectively. In (b), the intensity distribution of the probe beam at the front and exit faces of the waveguide is depicted.

illuminated by an Ar^{++} laser ($\lambda = 364$ nm) polarized parallel to the c-axis. This controlling light has a photon energy larger than the 3.3 eV bandgap of $KNbO_3$. The slit is imaged by the cylindrical lens CL_2 ($f = 50$ mm) onto the b-surface of the sample. The imaged UV stripe has a width of 25 μm along the c-axis at the incident surface and is aligned parallel to the a-axis. Due to the strong absorption of UV light in pure $KNbO_3$ (intensity absorption coefficient $2\alpha_c = 540\pm50$ cm^{-1}) [46], the UV stripe can induce field screening only for about 150 μm below the surface. A c-polarized HeNe laser beam ($\lambda = 633$ nm) [5] is focused by a spherical lens L_1 ($f = 80$ mm) down to a full width at half maximum (FWHM) of 15 μm and fed into the waveguide entrance. The opposite exit face is imaged by L_2 ($f = 100$ mm) onto a calibrated CCD camera that monitors the beam intensity distribution. Additional background illumination of the crystal is provided by a mercury arc-lamp with a total intensity of about 30 mW/cm^2. This background light produces a homogeneous conductivity which permits a better definition of the narrow stripe region where the external field is screened. Due to the extremely large photoconductivity induced by interband illumination, already weak intensity side lobes can enlarge the width of the induced waveguides in absence of background illumination.

Figure 6.16 depicts the output beam profile under the influence of the external field and of the striped UV illumination for different scenarios. Without both the electric field (E=0) and imaged slit (UV off), one observes the expected natural diffraction of the HeNe beam, which expands to a FWHM of 88 μm after traveling the 13.8 mm long crystal (Fig. 6.16(a)). No significant change in the intensity distribution is observed when either imaging the slit onto the crystal surface (UV on, here I_{UV}=3 W/cm^2) or when applying an external field, each separately, as shown in Figs. 6.16(b) and 6.16(c).

---

[5]While all results presented in this section are obtained with red probe light, as might be expected we could also demonstrate that the above technique can be used to guide light at the telecommunication wavelengths of 1.3 and 1.55 μm. Obviously, due to the larger natural diffraction, larger fields are required to achieve the same waveguide width in this case. The guided beam full-width-at-half maximum scales roughly as $\lambda/E^{1/2}$.
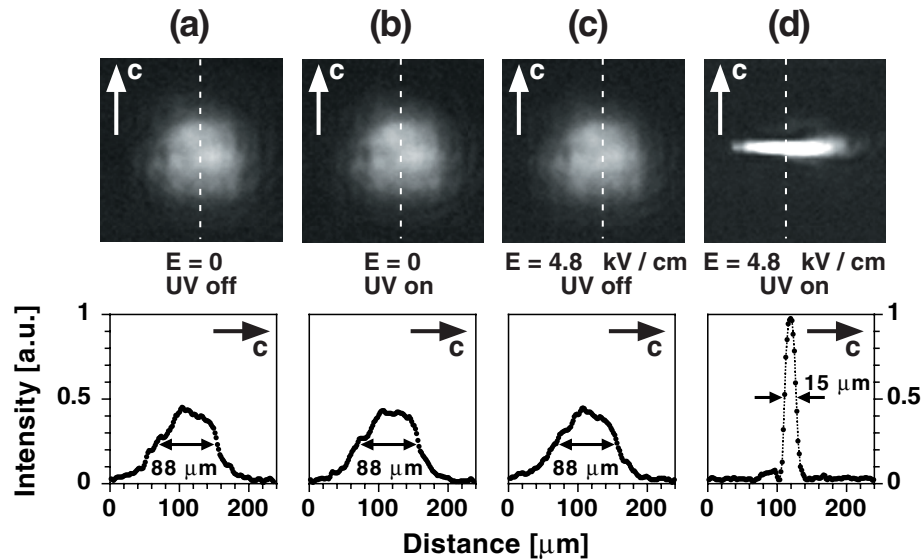
Figure 6.16: CCD-images of the intensity distribution of the probe beam at the exit face of the waveguide (240×240 μm). The UV light is incident from the left side. Underneath, the corresponding 1-D beam profiles along the white dotted lines. (a) E=0, UV illumination off, (b) E=0, UV on, (c) E=4.8 kV/cm, UV off, and (d) E=4.8 kV/cm, UV on. The intensity in the UV illumination pattern is 3 W/cm^2 corresponding to a total UV power of 10 mW.

Only the combination of electric field and slit illumination leads to waveguide formation and to the decrease of the beam width along c to 15 μm (FWHM, Fig. 6.16(d)), which corresponds to the width at the waveguide entrance. The guiding properties are found to be unchanged as the intensity of the HeNe beam varies from 0.004 to 200 W/cm^2. This confirms the robustness of interband photorefractive gratings mentioned earlier. The total losses in the induced waveguide correspond to an intensity loss coefficient $2\alpha < 0.02$ cm^{-1}, i.e. less than 0.1 dB/cm. In contrast to the beam width along c, the one along b (profiles not shown in Fig. 6.16) stays practically unchanged. Upon waveguide formation, one observes here an improved, more Gaussian like, beam profile, as well as a slight attraction of the beam's center towards the UV illuminated surface of the crystal, where the change in refractive index is the highest.
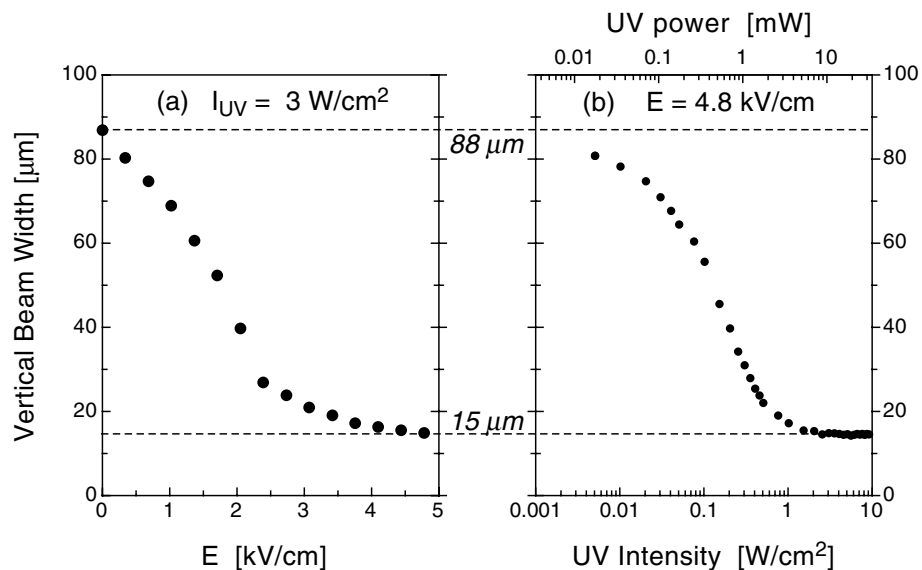

Figure 6.17: Dependence of the beam width (FWHM) along the c-axis on (a) the applied electric field E, and (b) the incident UV intensity.

By using the known electro-optic coefficients of KNbO$_3$ [88], for $E=$ 4.8 kV/cm, we expect the refractive index inside the illuminated region (core) to be larger by $\Delta n_c = 1.34 \times 10^{-4}$ with respect to the surrounding regions (cladding). For a simple model of a step-profile planar waveguide of 25 μm width along c and infinite extent along the b axis, waveguide theory [173] implies then that the two lowest order modes should be guided. The ground mode TM$_0$ of such a waveguide is expected to have a width of 17 μm (FWHM), which is in very good agreement with the measured 15 μm.

The influence of the experimental parameters on the guiding properties is analyzed with the help of Fig. 6.17. For increasing applied electric field the beam width decreases before reaching the constant saturation value. For $I_{UV}=$3 W/cm^2 the FWHM is smaller than 20 μm for $E > 3$ kV/cm as seen in Fig. 6.17(a). The corresponding UV intensity required for a field of 4.7 kV/cm (Fig. 6.17(b)) is ≈ 0.8 W/cm^2 that corresponds to a total UV power of less than 3 mW. Therefore the formation of the dynamic waveguide is possible already with a very moderate amount of UV light.
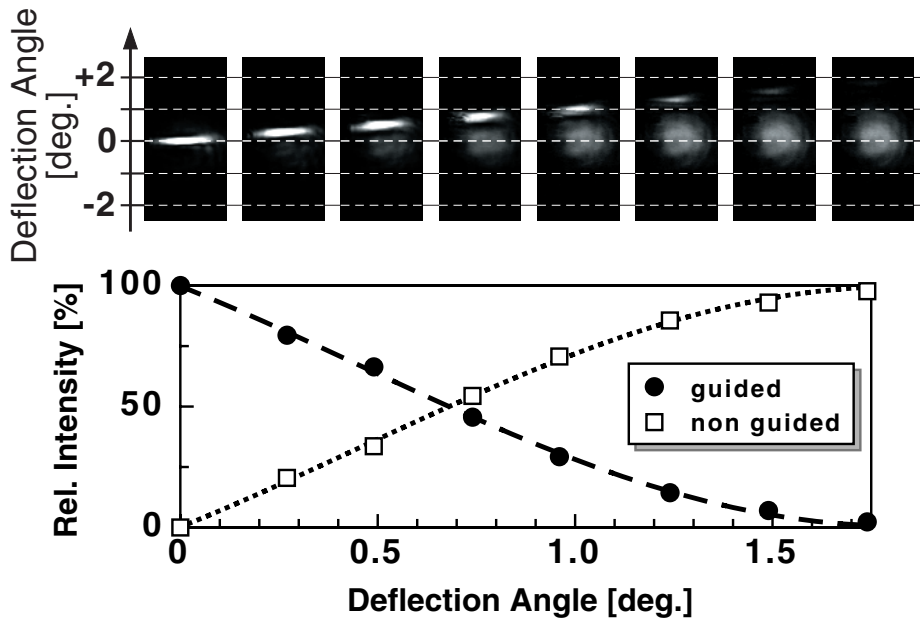

Figure 6.18: CCD-images of the intensity distribution of the probe beam at the exit face of the waveguide for different deflection angles. The integrated intensities of the guided and non-guided portion of the beam are plotted underneath as a function of the deflection angle inside the crystal. The dotted lines are guides to the eye.

One big advantage of the present approach is that it allows a reconfiguration of the waveguide structure in real time. By simply modifying the image mask, various waveguide designs are possible, e.g. Y- or multiple branches, Mach-Zehnder like interferometers, or switches. The feasibility of such structures is demonstrated by replacing the simple slit mask (Slit #1 in Fig. 6.15(b)) by a mask (Slit #2 in Fig. 6.15(b)) permitting a continuous rotation of one of its arms. The guided red beam encounters the pivot point of this rotation after 1/4 of its propagation in the crystal. By rotating the other 3/4 of the induced waveguide using the mask the guided beam is deflected. The beam profiles for different deflection angles are shown in the upper part of Fig. 6.18. The corresponding integrated relative intensities of the guided and non-guided portions are plotted underneath. For increasing deflection angles, the intensity of the guided beam decreases continuously from 100% at 0 deg. to 2.3% at 1.75 deg. For an angle of 0.7 deg.,

the deflected and non deflected beams are of equal intensity. In a 13.8 mm long crystal a deflection angle of 0.7 degrees corresponds to a total displacement of 170 μm at the exit surface. This displacement is larger than what was recently achieved with spatial solitons steering [174] and should allow separation of up to 12 output channels in a 1xN optical interconnect. Figure 6.19 shows two examples of light induced waveguides in the form of a Y-branch. In the first case the Y-branch is formed by straight waveguides, in the second by curved ones. As expected, the latter case leads to a better confinement of the input wave into the two exit channels. In the example presented here the mutual distance of the probe beams at the exit of the crystal is about 150 μm, corresponding to a deflection of each beam by about 0.5 degrees.
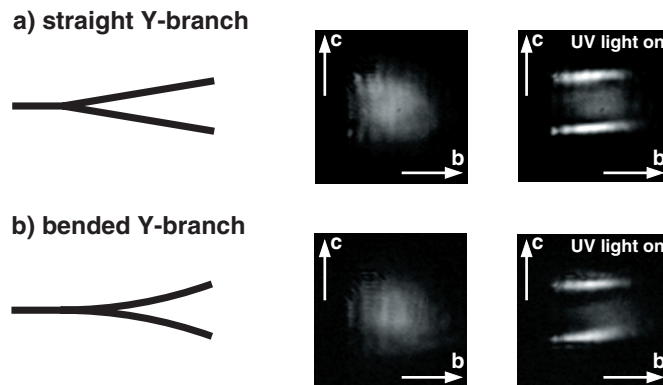

Figure 6.19: Straight (a) and bended (b) Y-branch waveguides. The CCD images show the diffracted He-Ne laser beam without controlling UV illumination (left) and the two splitted guided beams (right).

The buildup and reconfiguration time of the induced waveguide decreases as the square root of the light intensity as seen in Fig. 6.20. This behaviour is expected for interband photorefraction as already shown theoretically in section 2.2.2 and demonstrated experimentally in Fig. 2.8. One measures a waveguide build-up time of 63 μs for an UV intensity of 2.65 W/cm^2 and 780 μs for I_{UV}=20 mW/cm^2.
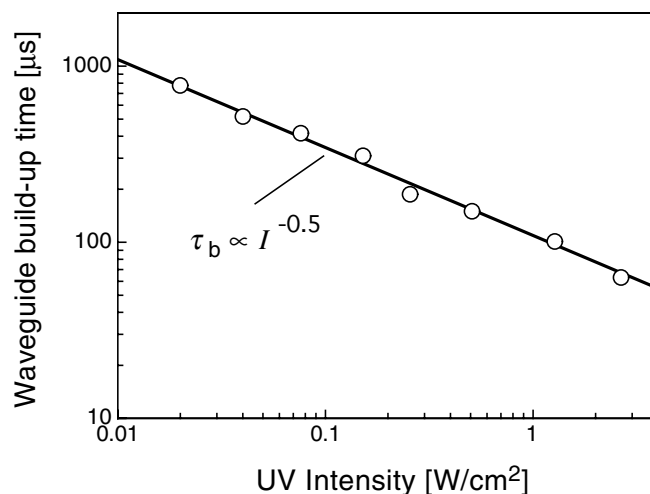

Figure 6.20: Buildup time constants of the light induced waveguide as a function of the UV stripe intensity measured at the crystal surface (E=4.8 kV/cm).

In summary, in this section we have shown that light can be guided by transient one-

dimensional[6] waveguides produced through side-illumination by means of the interband photorefractive effect. Reconfiguration and switching of such dynamic waveguides is possible in a time scale of few tens of microseconds. The presented method appears attractive for creation of active all-optical devices such as switches , tunable Y-branches, reconfigurable optical interconnects compatible with telecommunication wavelengths, or for the use as low loss waveguides for nonlinear optical frequency conversion applications.

6.5   Summary

In this chapter we have given a short description of interband photorefractive effects in two electro-optic materials, $KNbO_3$ and $Sn_2P_2S_6$. In the first material the band-to-band processes occur at near ultraviolet wavelengths while in the second one they take place already in the blue-green spectral region. In both cases refractive index variations being robust against erasure with longer wavelength light and having response speeds in the few μs region can be achieved. This makes them interesting for applications in fast parallel optical processing such as the optically addressed spatial light modulator and the Joint Fourier transform optical correlator presented in Sects. 6.2 and 6.3, respectively. By the same effect, as shown in Sect. 6.4, manipulation of an optical beam by means of a controlling light pattern becomes also possible.

---

[6]Several methods for a more efficient confinement also in the second transverse dimension based on alternative electrode configurations and/or special geometries are under investigation.

Chapter 7

Conclusions

Low power optical waves can interact in an efficient way by means of the photorefractive effect. This interaction is generally strongest in highly anisotropic crystals, such as $BaTiO_3$, $KNbO_3$, $LiNbO_3$, $Sr_xBa_{1-x}Nb_2O_6$ or $Sn_2P_2S_6$, that exhibit large electro-optic effects. We have presented the first treatment that takes into account the complete set of anisotropic material properties. These include the birefringence, the dielectric constants, the dichroism, the electro-optic constants, the elastic and photoelastic constants, the piezoelectric constants, the mobility tensor, and the cross-sections for free carrier photoexcitation. All these quantities influence the coupling constant substantially.

The role played by the anisotropy of the photoexcitation process with respect to light polarization was generally overlooked in previous literature. It was shown here that this anisotropy influences dramatically the two-wave mixing coupling constant because it determines directly the modulation depth of the photoexcited free carriers, which drives the whole charge redistribution process. We have also shown that the case where this quantity is isotropic corresponds to a worst-case scenario. An enhancement of the achievable two-wave mixing gain is always possible by introducing such an anisotropy.

Gratings in photorefractive materials are in general anisotropic in the sense that the refractive index modulation seen for different polarizations of the read-out wave can be strongly different. An extension of the well known coupled wave theory of Kogelnik [12], required to describe diffraction at such kind of gratings, was given in this work. New expressions which describe isotropic or anisotropic diffraction in general geometries for either transmission or reflection type gratings were given. For completeness, the simultaneous presence of phase and absorption modulation with arbitrary mutual phase shift was considered. This phase shift leads in general to nonreciprocal diffraction with respect to an exchange of the role of the incident and diffracted waves. The anisotropic coupled-wave theory presented here is relevant for any holographic materials having strong birefringence and/or containing gratings with strongly anisotropic properties, such as organic crystals [175], liquid crystals [176, 177] or polymer dispersed liquid crystals [178, 179].

Photorefractive gratings induced by interband absorbed light were modeled and characterized in the crystals $KNbO_3$ and $Sn_2P_2S_6$. The two most important advantages with respect to conventional photorefraction are the strongly increased response speed and the robustness of these dynamic gratings against erasure through a probe wave at a wavelength longer than the recording one. For parallel optical processing tasks based on Fourier or image plane processing a further advantage comes into play. The resulting gratings are rather thin with the thickness that depends on the absorption constant and on the recording light intensity. This leads to an increased resolution in image transfer

applications and to a higher shift invariance for pattern recognition tasks [142, 160, 180]. On the other hand, the drawbacks of interband photorefractive effects are also related with the large absorption constant. Any application where the recording light has to be reused or detected after the nonlinear material is better performed using conventional photorefractive effects. Examples of such applications can be found in the fields of holographic storage, adaptive interferometry, coherent image amplification, laser beam cleanup, phase conjugation, etc. [4, 6]. If, in contrast, the recording light can be fully sacrificed in the nonlinear sample, one is better off by using the interband processes. We have given three examples of this latter kind of applications. An optical addressed spatial light modulator with speed comparable to semiconductor multiple quantum well devices but higher resolution, a device where one is able to guide, steer and switch a light beam by means of a controlling light pattern, and a fast photorefractive Joint Fourier transform correlator cascaded to a holographic memory. This system is able to perform correlations at the, to our knowledge, unsurpassed rate of 10 kHz. The investigations on interband effects reported in this work were performed in the crystals $KNbO_3$ and $Sn_2P_2S_6$. However, the interband photorefractive effect is not limited to these two materials and, depending on the required wavelength of operation, other electro-optic compounds may be selected. For instance, the light induced waveguides reported in Sect. 6.4 may be produced using smaller applied fields with crystals possessing electro-optic coefficients even larger than $KNbO_3$, such as $BaTiO_3$ and $Sr_xBa_{1-x}Nb_2O_6$. Reaching the same, very low, waveguide losses observed in $KNbO_3$ puts a significant challenge on high purity crystal growth of these two materials.

In conclusion, this work has indicated two ways to increase the sensitivity and the strength of the photorefractive nonlinear process. The first is based on exploiting the increased efficiency of charge photoexcitation related to interband absorption processes. The second relates to the targeted utilization of the anisotropic properties of the material. We hope that these insights will lead to alternative approaches to new practical applications.

Appendix A

Linear propagation in dichroic birefringent media

Throughout this work we have used the effective amplitude absorption constants α seen by a given wave. In dichroic birefringent crystal this quantity is obviously not obtained by a simple trigonometric operation on a scalar number. It is related to the imaginary part $\overleftrightarrow{\varepsilon}_i^0$ of the dielectric tensor. We treat here the problem of linear propagation in a dichroic birefringent medium and derive Eq. (4.38) relating the effective amplitude absorption constants to the tensor $\overleftrightarrow{\varepsilon}_i^0$.

We consider a wave of the form $\vec{E} \exp\left[i(\vec{k} \cdot \vec{r} - \omega t)\right]$ with complex wavevector of the form $\vec{k} = \vec{k}_r + i\vec{k}_i$. If this wave is an eigenwave of the medium it has to fulfill the wave equation (4.5), which translates into

$$
-E\left[\left(\hat{e} \times \left(\vec{k}_r + i\vec{k}_i\right)\right) \times \left(\vec{k}_r + i\vec{k}_i\right)\right] e^{i\vec{k}_r \cdot \vec{r}} e^{-\vec{k}_i \cdot \vec{r}}
$$
$$
= k_o^2 \left[\overleftrightarrow{\varepsilon}_r^0 + i\overleftrightarrow{\varepsilon}_i^0\right] E\hat{e}\, e^{i\vec{k}_r \cdot \vec{r}} e^{-\vec{k}_i \cdot \vec{r}}, \tag{A.1}
$$

where we have used $\vec{E} = E\hat{e}$. Equation (A.1) is the same as Eq. (4.13) of Sect. 4.1. The real part of the space independent terms in (A.1) reads

$$
E\left[\left(\hat{e} \times \vec{k}_r\right) \times \vec{k}_r - \left(\hat{e} \times \vec{k}_i\right) \times \vec{k}_i\right] = -E\, k_o^2\, \overleftrightarrow{\varepsilon}_r^0 \cdot \hat{e}, \tag{A.2}
$$

Under our general assumption of moderate absorption ($\left|\vec{k}_i\right| \ll \left|\vec{k}_r\right|$), we recognize Eq. (A.2) as the equation describing linear propagation in lossless anisotropic media, as can be verified in several textbooks [104, 105, 181]. The remaining (imaginary) terms of (A.1) are related to the effective scalar absorption constant we are looking for, they read

$$
-iE\left[\left(\hat{e} \times \vec{k}_r\right) \times \vec{k}_i + \left(\hat{e} \times \vec{k}_i\right) \times \vec{k}_r\right] = i\, E\, k_o^2\, \overleftrightarrow{\varepsilon}_i^0 \cdot \hat{e}. \tag{A.3}
$$

We are considering here a boundary value problem, the wave should have a constant intensity at the input surface of the medium defined by the condition $\hat{\zeta} \cdot \vec{r} = 0$ (Figure 4.1). A constant intensity implies

$$
\left|\vec{E}\, e^{i\vec{k} \cdot \vec{r}}\right| \left(\hat{\zeta} \cdot \vec{r} = 0\right) = \text{constant}, \tag{A.4}
$$

which can be fulfilled only if the vector $\vec{k}_i$ is parallel to the surface normal $\hat{\zeta}$. One can write

$$
\vec{k}_i = \alpha \left(\pm \hat{\zeta}\right), \tag{A.5}
$$

where the effective absorption constant α is positive, and the (+) sign in (A.5) holds if the wave enters the medium at the plane $\hat{\zeta} \cdot \vec{r} = 0$, while the (-) sign holds if it enters at the plane $\hat{\zeta} \cdot \vec{r} = d$ and exits at $\hat{\zeta} \cdot \vec{r} = 0$. Therefore, the vectors $\vec{k}_r$ and $\vec{k}_i$ are in general noncollinear and the wave is inhomogeneous even in the absence of a nonlinear grating. By inserting (A.5) into (A.3) and using the vector identity $\left(\vec{a} \times \vec{b} \right) \times \vec{c} = \left(\vec{a} \cdot \vec{c} \right) \vec{b} - \left(\vec{b} \cdot \vec{c} \right) \vec{a}$ one gets

$$\alpha k_0 \, n \left[\left(\hat{e} \cdot \hat{\zeta} \right) \hat{k}_r + \left(\hat{e} \cdot \hat{k}_r \right) \hat{\zeta} - 2 \left(\hat{k}_r \cdot \hat{\zeta} \right) \hat{e} \right] = -k_0^2 \, \overset{\leftrightarrow}{\varepsilon}_i^0 \cdot \hat{e}, \tag{A.6}$$

where we have introduced explicitly the refractive index n seen by the wave and we have used the relationship $\vec{k}_r = k_0 n \hat{k}_r$. We are looking for an expression for α, which is obtained by multiplying Eq. (A.6) by $\hat{e}$

$$2\alpha k_0 \, n \left[\left(\hat{e} \cdot \hat{\zeta} \right) \left(\hat{k}_r \cdot \hat{e} \right) - \left(\hat{k}_r \cdot \hat{\zeta} \right) \right] = -k_0^2 \left(\hat{e} \cdot \overset{\leftrightarrow}{\varepsilon}_i^0 \cdot \hat{e} \right). \tag{A.7}$$

As in (4.21) the expression in the square brackets on the left-hand side is related again to the unit vector $\hat{u}$ along the Poynting vector of the wave and can be rewritten as

$$\left[\left(\hat{e} \cdot \hat{\zeta} \right) \left(\hat{k}_r \cdot \hat{e} \right) - \left(\hat{k}_r \cdot \hat{\zeta} \right) \right] = \hat{\zeta} \cdot \left[\hat{e} \left(\hat{k}_r \cdot \hat{e} \right) - \hat{k}_r \right]$$
$$= -g \left(\hat{\zeta} \cdot \hat{u} \right) = -g \cos \theta, \tag{A.8}$$

where the angle θ is defined by the last equality and is the same as the one introduced in Chapt. 4. We recall that $g = \hat{e} \cdot \hat{d}$, with $\hat{d}$ being the unit vector pointing in direction of the dielectric displacement vector (polarization). By combining Eqs. (A.7) and (A.8) one obtains finally the value of the amplitude absorption constant α which fulfills Eq. (4.5), that is

$$\alpha = \frac{k_0 \left(\hat{e} \cdot \overset{\leftrightarrow}{\varepsilon}_i^0 \cdot \hat{e} \right)}{2n \, g \, |\cos \theta|} = \frac{\pi \left(\hat{e} \cdot \overset{\leftrightarrow}{\varepsilon}_i^0 \cdot \hat{e} \right)}{\lambda n \, g \, |\cos \theta|}, \tag{A.9}$$

where λ is the vacuum wavelength. Equation (A.9) can also be used to derive the elements of the tensor $\overset{\leftrightarrow}{\varepsilon}_i^0$ from measurements of α for various wave propagation directions and polarizations.

Bibliography

[1] R. W. Boyd, *Nonlinear Optics* (Academic Press, San Diego, 1992).

[2] A. Ashkin, G. D. Boyd, J. M. Dziedzic, R. G. Smith, A. A. Ballman, J. J. Levinstein, and K. Nassau, "Optically induced refractive index inhomogeneities in $LiNbO_3$ and $LiTaO_3$," Appl. Phys. Lett. **25**, 233 (1966).

[3] P. Günter and J. P. Huignard, *Photorefractive materials and their Applications I : Fundamental Phenomena*, Vol. 1 of *Topics in Applied Physics* (Springer Verlag, Berlin, 1988).

[4] P. Günter and J. P. Huignard, *Photorefractive materials and their Applications II : Applications*, Vol. 2 of *Topics in Applied Physics* (Springer Verlag, Berlin, 1989).

[5] P. Yeh, *Introduction to photorefractive nonlinear optics*, *Wiley series in pure and applied optics* (Wiley, New York, 1993).

[6] S. I. Stepanov, "Applications of photorefractive crystals," Rep. Progr. Phys. **57**, 39 (1994).

[7] *Photorefractive effects and materials*, edited by D. D. Nolte (Kluwer Academic Publishers, Boston, 1995).

[8] L. Solymar, D. J. Webb, and A. Grunnet-Jepsen, *The physics and applications of photorefractive materials*, Vol. 11 of *Oxford Series in Optical and Imaging Science* (Clarendon Press, Oxford, 1996).

[9] F. Laeri, T. Tschudi, and J. Albers, "Coherent cw image amplifier and oscillator using two-wave interaction in a $BaTiO_3$ crystal," Opt. Commun. **47**, 387 (1983).

[10] M. H. Garrett, J. Y. Chang, H. P. Jenssen, and C. Warde, "High photorefractive sensitivity in an n-type 45°-cut $BaTiO_3$ crystal," Opt. Lett. **17**, 103 (1992).

[11] P. Günter, "Holography, coherent light amplification and optical phase conjugation with photorefractive materials," Phys. Rep. **93**, 199 (1982).

[12] H. Kogelnik, "Coupled wave theory for thick hologram gratings," Bell Syst. Tech. J. **48**, 2909 (1969).

[13] W. E. Moerner, A. Grunnetjepsen, and C. L. Thompson, "Photorefractive Polymers," Ann. Rev. Mat. Sci. **27**, 585 (1997).

[14] G. C. Valley, "Short-pulse grating formation in Photorefractive materials," IEEE J. Quantum Electr. **QE-19**, 1637 (1983).

[15] G. Pauliat and G. Roosen, "Photorefractive effect generated in sillenite crystals by picosecond pulses and comparison with the quasi-continuous regime," J. Opt. Soc. Am. B **7**, 2259 (1990).

[16] I. Biaggio, M. Zgonik, and P. Günter, "Photorefractive effects induced by picosecond light pulses in reduced $KNbO_3$," J. Opt. Soc. Am. B **9**, 1480 (1992).

[17] G. Montemezzani, P. Rogin, M. Zgonik, and P. Günter, "Interband photorefractive effects in $KNbO_3$ induced by ultraviolet illumination," Opt. Lett. **18**, 1144 (1993).

[18] V. L. Vinetskii and N. V. Kukhtarev, "Theory of the conductivity induced by recording holographic gratings in nonmetallic crystals," Sov. Phys. Solid State **16**, 2414 (1975).

[19] N. V. Kukhtarev, V. B. Markov, S. G. Odulov, M. S. Soskin, and V. L. Vinetskii, "Holographic storage in electro-optic crystals. I. Steady state," Ferroelectrics **22**, 949 (1979).

[20] N. V. Kukhtarev, V. B. Markov, S. G. Odulov, M. S. Soskin, and V. L. Vinetskii, "Holographic storage in electro-optic crystals. II: Beam coupling and light amplification," Ferroelectrics **22**, 961 (1979).

[21] J. Feinberg, J. D. Heimen, A. R. Tanguay, and R. W. Hellwarth, "Photorefractive effects and light-induced charge migration in barium titanate," J. Appl. Phys. **51**, 1297 (1980).

[22] A. M. Glass, D. VonderLinde, and T. J. Negran, "High-voltage bulk photovoltaic effect and the photorefractive effect in $LiNbO_3$," Appl. Phys. Lett. **25**, 233 (1974).

[23] B. I. Sturman and V. M. Fridkin, *The Photovoltaic and Photorefractive Effects in Noncentrosymmetric Materials*, 1 ed. (Gordon and Breach, Philadelphia, 1992).

[24] H. G. Ferstl, P. Hertel, E. Krätzig, and R. V. Baltz, "Investigations of the photovoltaic tensor in doped $LiNbO_3$," Phys. Stat. Sol. (b) **113**, 157 (1982).

[25] G. Montemezzani, C. Medrano, P. Günter, and M. Zgonik, "Charge Carrier Photoexcitation and Two Wave Mixing In Dichroic Materials," Phys. Rev. Lett. **79**, 3403 (1997).

[26] M. Cronin-Golomb, "Whole beam method for photorefractive nonlinear optics," Opt. Commun. **89**, 276 (1992).

[27] D. N. Christodoulides and M. I. Carvalho, "Bright, dark, and gray spatial soliton states in photorefractive media," J. Opt. Soc. Am. B **12**, 1628 (1995).

[28] A. A. Zozulya and D. Z. Anderson, "Propagation of an optical beam in a photorefractive medium in the presence of a photogalvanic nonlinearity or an externally applied electric field," Physical Review A **51**, 1520 (1995).

[29] R. Ryf, G. Montemezzani, M. Wiki, P. Günter, and A. A. Zozulya, "Launching one-transverse-dimensional photorefractive solitons in $KNbO_3$ crystals," Opt. Commun. **159**, 339 (1999).

[30] F. Vachss and L. Hesselink, "Nonlinear photorefractive response at high modulation depths," J. Opt. Soc. Am. A **5**, 690 (1988).

[31] E. Serrano, M. Carrascosa, and F. Agullo-Lopez, "Analytical and Numerical Study Of Photorefractive Kinetics At High Modulation Depths," J. Opt. Soc. Am. B **13**, 2587 (1996).

[32] M. R. Belic, D. Timotijevic, M. Petrovic, and M. V. Jaric, "Exact solution to photorefractive two-wave mixing with arbitrary modulation depth," Opt. Commun. **123**, 201 (1996).

[33] N. Kukhtarev, S. Lyuksyutov, P. Buchhave, T. Kukhtareva, K. Sayano, and P. P. Banerjee, "Self-enhancement of dynamic gratings in photogalvanic crystals," Phys. Rev. A **58**, 4051 (1998).

[34] F. Jariego and F. Agullo-Lopez, "Monotonic versus oscillatory behaviour during holographic writing in photorefractive photovoltaic materials," Opt. Commun. **76**, 169 (1990).

[35] C. Gu, J. Hong, H. Y. Li, D. Psaltis, and P. Yeh, "Dynamics of grating formation in photovoltaic media," J. Appl. Phys. **69**, 1167 (1991).

[36] F. Agullo-Lopez, J. M. Cabrera, and F. Agullo-Rueda, *Electrooptics: Phenomena, Materials and Applications* (Academic Press, London, 1994).

[37] L. Solymar, in *Electro-optic and Photorefractive Materials*, *Springer Proceedings in Physics*, edited by P. Günter (Springer-Verlag, Berlin, 1987), pp. 229–245.

[38] G. Montemezzani, M. Zgonik, and P. Günter, "Photorefractive charge compensation at elevated temperatures and application to $KNbO_3$," J. Opt. Soc. Am. B **10**, 171 (1993).

[39] B. I. Sturman, M. Mann, J. Otten, and K. H. Ringhofer, "Space-charge waves and their parametric excitation," J. Opt. Soc. Am. B **10**, 1919 (1993).

[40] B. I. Sturman, E. Shamonina, M. Mann, and K. H. Ringhofer, "Space-charge waves in photorefractive ferroelectrics," J. Opt. Soc. Am. B **12**, 1642 (1995).

[41] M. Cronin-Golomb, "Photorefractive surface waves," Opt. Lett. **20**, 2075 (1995).

[42] V. A. Kalinin and L. Solymar, "Energy relations for space-charge waves in photorefractive materials," Appl. Phys. Lett. **68**, 3826 (1996).

[43] B. I. Sturman, M. Aguilar, and F. Agullo-Lopez, "Analysis of space-charge wave effects in GaAs:EL2," Phys. Rev. B **54**, 13737 (1996).

[44] H. C. Pedersen and P. M. Johansen, "Space-charge wave theory of photorefractive parametric amplification," J. Opt. Soc. Am. B **16**, 1185 (1999).

[45] P. Yeh, "Fundamental limit of the speed of photorefractive effect and its impact on device applications and material research," Appl. Opt. **26**, 602 (1987).

[46] G. Montemezzani, P. Rogin, M. Zgonik, and P. Günter, "Interband photorefractive effects: Theory and experiments in $KNbO_3$," Phys. Rev. B **49**, 2484 (1994).

[47] P. Bernasconi, G. Montemezzani, and P. Günter, "Off-Bragg-angle light diffraction and structure of dynamic interband photorefractive gratings," Appl. Phys. B **68**, 833 (1999).

[48] M. Carrascosa, F. Agullo-Lopez, G. Montemezzani, and P. Günter, "Photorefractive gratings generated by band-gap excitation: Application to $KNbO_3$," Appl. Phys. B **72**, 697 (2001).

[49] P. Bernasconi, G. Montemezzani, I. Biaggio, and P. Günter, "Characterization Of the Bipolar Mobility In Polar Materials By Interband Photoexcitation," Phys. Rev. B **56**, 12196 (1997).

[50] P. Bernasconi, PhD. Dissertation, Swiss Federal Institute of Technology, Diss ETH Nr. 12761, Zürich, 1998.

[51] G. C. Valley, "Simultaneous electron/hole transport in photorefractive materials," J. Appl. Phys. **59**, 3363 (1986).

[52] F. P. Strohkendl, J. M. C. Jonathan, and R. W. Hellwarth, "Hole-electron competition in photorefractive gratings," Opt. Lett. **11**, 312 (1986).

[53] N. V. Kukhtarev, G. E. Dovgalenko, and V. N. Markov, "Influence of the optical activity on hologram formation in photorefractive crystals," Appl. Phys. A **33**, 227 (1984).

[54] S. Zhivkova and M. Miteva, "Holographic recording in photorefractive crystals with simultaneous electron-hole transport and two active centers," J. Appl. Phys. **68**, 3099 (1990).

[55] M. C. Bashaw, T.-P. Ma, R. C. Barker, S. Mroczkowski, and R. R. Dube, "Theory of complementary holograms arising from electron-hole transport in photorefractive media," J. Opt. Soc. Am. B **7**, 2329 (1990).

[56] R. Matull and R. A. Rupp, "Microphotometric investigation of fixed holograms," J. Phys. D: Appl. Phys. **21**, 1556 (1988).

[57] G. M. Sessler, *Electrets*, Vol. 33 of *Topics in Applied Physics*, 2 ed. (Springer, Berlin, 1987).

[58] E. M. Panchenko, O. I. Prokopalo, A. E. Panich, V. A. Zagouriko, and Y. A. Trusov, "Electret state in oxides of the perovskite family," J. Phys. D **22**, 1372 (1989).

[59] E. I. Bondarenko, V. A. Zagorulko, Y. S. Kuz'minov, A. N. Pavlov, E. M. Panchenko, and E. M. Prokopalo, "Model of the electret state in oxygen-octahedral materials," Sov. Phys. Sol. State **27**, 629 (1985).

[60] R. Kressmann, G. M. Sessler, and P. Gunther, "Space-charge electrets," IEEE Trans. Diel. Electr. Insul. **3**, 607 (1996).

[61] G. Montemezzani, PhD. Dissertation, Swiss Federal Institute of Technology, Diss ETH Nr. 10013, Zürich, 1993.

[62] M. C. Bashaw and J. F. Heanue, "Quasi Stabilized Ionic Gratings In Photorefractive Media For Multiplex Holography," J. Opt. Soc. Am. B **14**, 2024 (1997).

[63] A. Yariv, S. S. Orlov, and G. A. Rakuljic, "Holographic Storage Dynamics In Lithium Niobate: Theory and Experiment," J. Opt. Soc. Am. B **13**, 2513 (1996).

[64] J. J. Amodei and D. L. Staebler, "Holographic pattern fixing in electro-optic crystals," Appl. Phys. Lett. **18**, 540 (1971).

[65] L. Arizmendi, "Thermal fixing of holographic gratings in $Bi_{12}SiO_{20}$," J. Appl. Phys. **65**, 423 (1989).

[66] G. Montemezzani and P. Günter, "Thermal fixing in pure and doped $KNbO_3$ crystals," J. Opt. Soc. Am. B **7**, 2323 (1990).

[67] D. Kirillov and J. Feinberg, "Fixable complementary gratings in photorefractive $BaTiO_3$," Opt. Lett. **16**, 1520 (1991).

[68] A. Xin, D. Psaltis, and G. W. Burr, "Thermal fixing of 10,000 holograms in $LiNbO_3$:Fe," Appl. Opt. **38**, 386 (1999).

[69] P. Hertel, K. H. Ringhofer, and R. Sommerfeldt, "Theory of thermal hologram fixing and application to $LiNbO_3$:Cu," Phys. Stat. sol. (a) **104**, 855 (1987).

[70] M. Carrascosa and F. Agullo-Lopez, "Theoretical modeling of the fixing and developing of holographic gratings in $LiNbO_3$," J. Opt. Soc. Am. B **7**, 2317 (1990).

[71] M. Carrascosa and F. Agullo-Lopez, "Optimization of the developing stage for fixed gratings in $LiNbO_3$," Opt. Commun. **126**, 240 (1996).

[72] B. I. Sturman, M. Carrascosa, F. Agullo-Lopez, and J. Limeres, "Theory of high-temperature photorefractive phenomena in $LiNbO_3$ crystals and applications to experiment," Phys. Rev. B **57**, 12792 (1998).

[73] G. C. Valley, "Erase rates in photorefractive materials with two photoactive species," Appl. Opt. **22**, 3160 (1983).

[74] G. Lesaux, G. Roosen, and A. Brun, "Observation and analysis of the fast photorefractive process in BSO," Opt. Commun. **56**, 374 (1986).

[75] G. A. Brost, R. A. Motes, and J. R. Rotge, "Intensity-dependent absorption and photorefractive effects in barium titanate," J. Opt. Soc. Am. B **5**, 1879 (1988).

[76] L. Holtmann, "A model for the nonlinear photoconductivity of $BaTiO_3$," Phys. Stat. Sol. (a) **113**, K89 (1989).

[77] F. P. Strohkendl, "Light-induced dark decays of photorefractive gratings and their observation in $Bi_{12}SiO_{20}$," J. Appl. Phys. **65**, 3773 (1989).

[78] D. Mahgerefteh and J. Feinberg, "Explanation of the sublinear photoconductivity of photorefractive barium titanate," Phys. Rev. Lett. **64**, 2195 (1990).

[79] R. S. Cudney, R. M. Pierce, G. D. Bacher, and J. Feinberg, "Absorption gratings in photorefractive crystals with multiple levels," J. Opt. Soc. Am. B **8**, 1326 (1991).

[80] P. Tayebati and D. Mahgerefteh, "Theory of the photorefractive effect for $Bi_{12}SiO_{20}$ and $BaTiO_3$ with shallow traps," J. Opt. Soc. Am. B **8**, 1053 (1991).

[81] K. Buse, "Light Induced Charge Transport Processes In Photorefractive Crystals I: Models and Experimental Methods," Appl. Phys. B **64**, 273 (1997).

[82] A. A. Izvanov, A. E. Mandel, N. D. Khatkov, and S. M. Shandarov, "Influence of the piezoelectric effect on hologram writing and reconstruction in photorefractive crystals," Optoel. Data Proc. Instr. **2**, 80 (1986).

[83] S. I. Stepanov, S. M. Shandarov, and N. D. Khatkov, "Photoelastic contribution to the photorefractive effect in cubic crystals," Sov. Phys. Solid State **29**, 1754 (1987).

[84] P. Günter and M. Zgonik, "Clamped-unclamped electro-optic coefficient dilemma in photorefractive phenomena," Opt. Lett. **16**, 1826 (1991).

[85] G. Pauliat, M. Mathey, and G. Roosen, "Influence of piezoelectricity on the photorefractive effect," J. Opt. Soc. Am. B **8**, 1942 (1991).

[86] J. F. Nye, *Physical properties of crystals* (Clarendon Press, Oxford, 1985).

[87] D. F. Nelson and M. Lax, "New symmetry for acousto-optic scattering," Phys. Rev. Lett. **24**, 1187 (1970).

[88] M. Zgonik, R. Schlesser, I. Biaggio, E. Voit, J. Tscherry, and P. Günter, "Materials constants of $KNbO_3$ relevant for electro- and acousto-optics," J. Appl. Phys. **74**, 1287 (1993).

[89] M. Zgonik, P. Bernasconi, M. Duelli, R. Schlesser, P. Günter, M. H. Garrett, D. Rytz, Y. Zhu, and X. Wu, "Dielectric, elastic, piezoelectric, electro-optic, and elasto-optic tensors of $BaTiO_3$ crystals," Phys. Rev. B **50**, 5941 (1994).

[90] M. Zgonik, K. Nakagawa, and P. Günter, "Electro-optic and dielectric properties of photorefractive $BaTiO_3$ and $KNbO_3$," J. Opt. Soc. Am. B **12**, 1416 (1995).

[91] G. Montemezzani, A. A. Zozulya, L. Czaia, D. Z. Anderson, M. Zgonik, and P. Günter, "Origin of the lobe structure in photorefractive beam fanning," Phys. Rev. A **52**, 1791 (1995).

[92] K. Kojima, "Diffraction of light in an inhomogeneous and anisotropic medium," Jap. J. Appl. Phys. **21**, 1303 (1982).

[93] K. Rokushima and J. Yamakita, "Analysis of anisotropic dielectric gratings," J. Opt. Soc. Am. **73**, 901 (1983).

[94] R. V. Johnson and J. A. R. Tanguay, "Optical beam propagation method for birefringent phase grating diffraction.," Opt. Eng. **25**, 235 (1986).

[95] E. N. Glytsis and T. K. Gaylord, "Rigurous three-dimensional coupled-wave diffraction analysis of single and cascaded anisotropic gratings," J. Opt. Soc. Am. A **4**, 2061 (1987).

[96] F. Vachss and L. Hesselink, "Holographic beam coupling in anisotropic photore-fractive media," J. Opt. Soc. Am. A **4**, 325 (1987).

[97] I. C. Khoo, "Dynamic gratings and the associated self diffractions and wavefront conjugation processes in nematic liquid crystals," IEEE J. Quantum Electron. **22**, 1268 (1986).

[98] W. E. Moerner and S. M. Silence, "Polymeric photorefractive materials," Chem. Rev. **94**, 127 (1994).

[99] K. Sutter, J. Hulliger, and P. Günter, "Photorefractive effects observed in the organic crystal 2-cyclooctylamino-5-nitropyridine doped with 7,7,8,8-teracyanoquidodimethane," Solid State. Commun. **74**, 867 (1990).

[100] G. Montemezzani and P. Günter, in *Notions and Perspectives in Nonlinear Optics*, edited by O. Keller (World Scientific, Singapore, 1996), pp. 370–427.

[101] S. J. Stepanov, M. P. Petrov, and A. A. Kamshilin, "Diffraction of light with ro-tation of the plane of polarization in volume holograms in electrooptical crystals," Sov. Tech. Phys. Lett. **3**, 345 (1977).

[102] T. K. Gaylord and M. G. Moharam, "Thin and thick gratings: terminology clari-fication," Appl. Opt. **20**, 3271 (1981).

[103] M. G. Moharam and T. K. Gaylord, "Rigorous coupled-wave analysis of planar-grating diffraction," J. Opt. Soc. Am. **71**, 811 (1981).

[104] V. M. Agranovich and V. L. Ginzburg, in *Crystal optics with spatial dispersion, and excitons, Springer Series in Solid-State Sciences 42*, 2 ed., edited by H. J. Queisser (Springer Verlag, Berlin, 1984).

[105] M. Born and E. Wolf, *Principles of optics*, 6 ed. (Pergamon Press, Oxford, 1980).

[106] G. N. Ramachandran and S. Ramaseshan, in *Handbuch der Physik*, edited by S. Flügge (Springer-Verlag, Berlin, 1961), Vol. 25/1, pp. 85–96.

[107] E. Guibelalde, "Coupled wave analysis for out-of-phase mixed thick hologram gratings," Opt. Quantum Electr. **16**, 173 (1984).

[108] R. Birabassov, A. Yesayan, and T. V. Galtsyan, "Nonreciprocal diffraction by spatial modulation of absorption and refraction," Opt. Lett. **24**, 1669 (1999).

[109] S. R. Marder, J. W. Perry, and C. P. Yakymyshyn, "Organic salts with large second-order optical nonlinearities," Chem. Mater. **6**, 1137 (1994).

[110] F. Pan, G. Knöpfle, C. Bosshard, S. Follonier, R. Spreiter, M. S. Wong, and P. Günter, "Electro-optic properties of the organic salt 4-N,N-Dimethylamino-4'-N-methyl-stilbazolium tosylate (DAST)," Appl. Phys. Lett. **69**, 13 (1996).

[111] K. Sutter and P. Günter, "Photorefractive Gratings in the Organic Crystal 2-Cyclooctylamino-5-Nitropyridine doped with 7,7,8,8-Tetracyanoquinodimethane," J. Opt. Soc. Am. B **7**, 2274 (1990).

[112] R. A. Rupp, A. Maillard, and J. Walter, "Inpact of the sublinear photoconductivity law on the interpretation of holographic results in BaTiO$_3$," Appl. Phys. A **49**, 259 (1989).

[113] P. Yeh, "Contra-directional two-wave mixing in photorefractive media," Opt. Comm. **45**, 323 (1983).

[114] D. Mahgerefteh, D. Kirillov, R. S. Cudney, G. D. Bacher, R. M. Pierce, and J. Feinberg, "Anisotropy of the hole drift mobility in barium titanate," Phys. Rev. B **53**, 7094 (1996).

[115] P. Bernasconi, I. Biaggio, M. Zgonik, and P. Günter, "Anisotropy Of the Electron and Hole Drift Mobility In KNbO$_3$ and BaTiO$_3$," Phys. Rev. Lett. **78**, 106 (1997).

[116] D. Rytz, M. B. Klein, R. A. Mullen, R. N. Schwartz, G. C. Valley, and B. A. Wechsler, "High-efficiency fast response in photorefractive BaTiO$_3$ at 120 C," Appl. Phys. Lett. **52**, 1759 (1988).

[117] G. Montemezzani, "Optimization of photorefractive two-wave mixing by accounting for material anisotropies: KNbO$_3$ and BaTiO$_3$," Phys. Rev. A (62), 053803 (2000).

[118] S. MacCormack, G. D. Bacher, J. Feinberg, S. O'Brien, R. J. Lang, M. B. Klein, and B. A. Wechsler, "Powerful diffraction-limited semiconductor laser using photorefractive beam coupling," Opt. Lett. **22**, 227 (1997).

[119] C. Medrano, M. Zgonik, I. Liakatas, and P. Günter, "Infrared photorefractive effect in doped KNbO$_3$ crystals," J. Opt. Soc. Am. B **13**, 2657 (1996).

[120] K. R. MacDonald, J. Feinberg, M. Z. Zha, and P. Günter, "Asymmetric transmission through a photorefractive crystal of barium titanate," Opt. Commun. **50**, 146 (1984).

[121] S. Breugnot, H. Rajbenbach, M. Defour, and J. P. Huignard, "Low-noise preamplifier for multistage photorefractive image amplification," Opt. Lett. **20**, 1568 (1995).

[122] P. Xie, P. Y. Wang, J. H. Dai, and H. J. Zhang, "Effect of random volume scattering on image amplification and beam fanning in photorefractive materials," J. Opt. Soc. Am. B **15**, 1889 (1998).

[123] T. Kuroiwa and M. Matsubara, "Selective image amplification by two-wave mixing with two photorefractive BaTiO3 crystals," Electron. Commun. Jpn. Part II Electronics **83**((7)), 14 (2000).

[124] A. Takada and M. Cronin-Golomb, "Laser beam cleanup with photorefractive two-beam coupling," Opt. Lett. **20**, 1459 (1995).

[125] A. Brignon, J. P. Huignard, M. H. Garrett, and I. Mnushkina, "Spatial beam cleanup of a Nd:YAG laser operating at 1.06 μm with two wave mixing in Rh:BaTiO$_3$," Appl. Opt. **36**, 7788 (1997).

[126] M. Lobel, P. M. Petersen, and P. M. Johansen, "Tunable single-mode operation of a high-power laser-diode array by use of an external cavity with a grating and a photorefractive phase-conjugate mirror," J. Opt. Soc. Am. B **15**, 2000 (1998).

[127] M. Ewart, M. Zgonik, and P. Günter, "Nanosecond optical response to pulsed UV excitation in KNbO$_3$," Opt. Commun. **141**, 99 (1997).

[128] G. Montemezzani, P. Bernasconi, P. Dittrich, R. Ryf, and P. Günter, "Interband photorefractive effects and applications," Proc. SPIE **4358**, 1-10 (2001).

[129] H. J. Eichler, P. Günter, and D. W. Pohl, *Laser-induced dynamic gratings* (Springer Verlag, Berlin, 1986).

[130] N. Kukhtarev, T. Kukhtareva, and P. P. Banerjee, "A unified treatment of radiation-induced photorefractive, thermal, and neutron transmutation gratings," Proc. IEEE **87**, 1857 (1999).

[131] S. Ducharme, "Pyro-electro-optic phase gratings," Opt. Lett. **16**, 1791 (1991).

[132] K. Buse, "Thermal gratings and pyroelectrically produced charge redistribution in BaTiO$_3$ and KNbO$_3$," J. Opt. Soc. Am. B **10**, 1266 (1993).

[133] C. D. Carpentier and R. Nitsche, "Vapour growth and crystal data of the thio(seleno)-hypodiphosphates Sn$_2$P$_2$S$_6$, Sn$_2$P$_2$Se$_6$, Pb$_2$P$_2$S$_6$, Pb$_2$P$_2$Se$_6$ and their mixed crystals," Mat. Res. Bull. **9**, 401 (1974).

[134] A. A. Grabar, Y. M. Vysochanskii, S. I. Perechinskii, L. A. Salo, M. I. Gurzan, and V. Y. Slivka, "Thermooptic investigations of ferroelectric Sn$_2$P$_2$S$_6$," Sov. Phys. Solid State **26**, 2087 (1984).

[135] S. G. Odoulov, A. N. Shumelyuk, U. Hellwig, R. A. Rupp, A. A. Grabar, and I. M. Stoyka, "Photorefraction in tin hypothiodiphosphate in the near infrared," J. Opt. Soc. Am. B **13**, 2352 (1996).

[136] A. A. Grabar, I. V. Kedyk, M. I. Gurzan, I. M. Stoika, A. A. Molnar, and Y. M. Vysochanskii, "Enhanced photorefractive properties of modified Sn$_2$P$_2$S$_6$," Opt. Commun. **188**, 187 (2001).

[137] R. Ryf, G. Montemezzani, P. Günter, A. A. Grabar, and I. M. Stoika, "Interband photorefraction at visible wavelength in Sn$_2$P$_2$S$_6$ crystals," Trends Opt. Photon. **27**, 80 (1999).

[138] R. Ryf, Ph.D. thesis, Swiss Federal Institute of Technology, Diss ETH Nr. 13546, Zürich, 2000.

[139] P. Bernasconi, G. Montemezzani, M. Wintermantel, I. Biaggio, and P. Günter, "High resolution, high speed photorefractive incoherent-to-coherent optical converter," Opt. Lett. **24**, 199 (1999).

[140] A. A. Kamshilin and M. P. Petrov, "Holographic image conversion in a Bi$_{12}$SiO$_{20}$ crystal," Sov. Tech. Phys. Lett. **6**, 144 (1980).

[141] Y. Shi, D. Psaltis, A. Marrakchi, and A. R. Tanguay, "Photorefractive incoherent-to-coherent optical converter," Appl. Opt. **22**, 3665 (1983).

[142] P. Amrhein and P. Günter, "Resolution limit for isotropic and anisotropic Bragg diffraction from finite holographic gratings," J. Opt. Soc. Am. B **12**, 2387 (1990).

[143] J. S. Zhang, H. T. Wang, S. Yoshikado, and T. Aruga, "Incoherent to Coherent Conversion By Use Of the Photorefractive Fanning Effect," Opt. Lett. **22**, 1612 (1997).

[144] J. S. Zhang, H. T. Wang, S. Yoshikado, and T. Aruga, "High-resolution incoherent-to-coherent conversion by use of the photorefractive fanning effect," Appl. Opt. **38**, 995 (1999).

[145] A. Marrakchi, A. R. Tanguay, J. Yu, and D. Psaltis, "Physical characterisation of the photorefractive incoherent-to-coherent optical converter," Opt. Eng. **24**, 124 (1985).

[146] E. Voit and P. Günter, "Photorefractive spatial light modulation by anisotropic self-diffraction in $KNbO_3$ crystals," Opt. Lett. **12**, 769 (1987).

[147] B. Ai, D. S. Glassner, R. J. Knize, and J. P. Partanen, "A thin atomic vapor as nonlinear optical medium," Appl. Phys. Lett. **64**, 951 (1994).

[148] I. Biaggio, J. P. Partanen, B. Ai, R. J. Knize, and R. W. Hellwarth, "Optical image processing by an atomic vapour," Nature **371**, 318 (1994).

[149] Y. Nagao, H. Sakata, and Y. Mimura, "$Bi_{12}SiO_{20}$ thin-film spatial light modulator," Appl. Opt. **31**, 3966 (1992).

[150] Y. Bitou and T. Minemoto, "High-contrast spatial light modulator by use of the electroabsorption and electro-optic effects in a GaAs single crystal," Appl. Opt. **37**, 4347 (1998).

[151] Q. Wang-Song, C. Zhang, R. Blumer, R. B. Gross, Z. Chen, and R. R. Birge, "Chemically enhanced bacteriorhodospin in thin-film spatial light modulator," Opt. Lett. **18**, 1373 (1993).

[152] S. R. Bowman, W. S. Rabinovich, G. Beadie, S. M. Kirkpatrick, D. S. Katzer, K. Ikossi-Anastasiou, and C. L. Adler, "Characterization of high performance integrated optically adressed spatial light modulators," J. Opt. Soc. Am. B **15**, 640 (1998).

[153] S. Fukushima, T. Kurokawa, and M. Ohno, "Real-time hologram construction and reconstruction using a high-resolution spatial light modulator," Appl. Phys. Lett. **58**, 787 (1991).

[154] B. S. Lowans, B. Bates, and R. G. H. Greer, "Optical characteristics of an optically addressed spatial light modulator for nonlinear joint transform correlation," Opt. Commun. **109**, 29 (1994).

[155] R. Ryf, G. Montemezzani, P. Günter, A. A. Grabar, I. M. Stoika, and Y. M. Vysochanskii, "High frame rate joint Fourier transform correlation by pulsed interband photorefraction in $Sn_2P_2S_6$," Trends Opt. Photon. **62**, (in press) (2001).

[156] C. S. Weaver and J. W. Goodman, "A technique for optically convolving two functions," Appl. Opt. **5**, 1248 (1966).

[157] J. Colin, N. Landru, V. Laude, S. Breugnot, H. Rajbenbach, and J. P. Huignard, "High-speed photorefractive joint transform correlator using nonlinear filters," J. Opt. A: Pure Appl. Opt. **1**, 283 (1999).

[158] Y. Taketomi, J. E. Ford, H. Sasaki, J. Ma, Y. Fainman, and S. H. Lee, "Incremental recording for photorefractive hologram multiplexing," Opt. Lett. **16**, 1774 (1991).

[159] E. S. Maniloff and K. M. Johnson, "Incremental recording for photorefractive hologram multiplexing: comment," Opt. Lett. **17**, 961 (1992).

[160] R. Ryf, G. Montemezzani, P. Günter, Y. Furukawa, and K. Kitamura, "Photorefractive multichannel correlator based on stoichiometric LiTaO$_3$," Appl. Phys. B **72**, 737 (2001).

[161] D. R. Hofstadter, *Gödel, Escher, Bach: an eternal golden braid* (New York Vintage Books, New York, 1980).

[162] C. Vassallo, in *Optical waveguide concepts*, Vol. 1 of *Optical Wave Sciences and Technology*, edited by H. Hung-Chia (Elsevier, Amsterdam, 1991).

[163] K. J. Ebeling, *Integrated optoelectronics: waveguide optics, photonics, semiconductors* (Springer-Verlag, Berlin, 1993).

[164] R. G. Hunsperger, *Integrated optics: theory and technology*, 4th ed. (Springer-Verlag, Berlin, 1995).

[165] P. Dittrich, G. Montemezzani, P. Bernasconi, and P. Günter, "Fast, reconfigurable light-induced waveguides," Opt. Lett. **24**, 1508 (1999).

[166] D. Kip, "Photorefractive waveguides in oxide crystals: fabrication, properties, and applications," Appl. Phys. B **67**, 131 (1998).

[167] O. Matoba, K. Itoh, and K. Kuroda, "Photorefractive optics in dynamic interconnection," Proc. IEEE **87**, 2030 (1999).

[168] K. Itoh, O. Matoba, and Y. Ichioka, "Fabrication experiment of photorefractive three-dimensional waveguides in lithium niobate," Opt. Lett. **19**, 652 (1994).

[169] O. Matoba, T. Inujima, T. Shimura, and K. Kuroda, "Segmented photorefractive waveguides in LiNbO3:Fe," J. Opt. Soc. Am. B **15**, 2006 (1998).

[170] M. F. Shih, Z. G. Chen, M. Mitchell, M. Segev, H. Lee, R. S. Feigelson, and J. P. Wilde, "Waveguides Induced By Photorefractive Screening Solitons," J. Opt. Soc. Am. B **14**, 3091 (1997).

[171] M. Segev and G. Stegeman, "Self-trapping of optical beams: Spatial solitons," Physics Today **51**((8) Part 1), 42 (1998).

[172] A. Bekker, A. Peda'el, N. K. Berger, M. Horowitz, and B. Fischer, "Optically induced domain waveguides in $Sr_xBa_{1-x}Nb_2O_6$ crystals," Appl. Phys. Lett. **72**, 3121 (1998).

[173] A. W. Snyder and J. D. Love, *Optical Waveguide Theory* (Chapman & Hall, London, 1983).

[174] L. Friedrich, G. I. Stegeman, P. Millar, and J. S. Aitchison, "1 x 4 optical interconnect using electronically controlled angle steering of spatial solitons," IEEE Photon. Techn. Lett. **11**, 988 (1999).

[175] S. Follonier, C. Bosshard, F. Pan, and P. Günter, "Photorefractive effects observed in 4-N, N-dimethylamino-4'-N'-methyl-stilbazolium toluene-p-sulfonate," Opt. Lett. **21**, 1655 (1996).

[176] E. V. Rudenko and A. V. Sukhov, "Optically induced spatial charge separation in a nematic and the resultant orientational nonlinearity," JETP **78**, 875 (1994).

[177] I. C. Khoo, M. Y. Shih, M. V. Wood, B. D. Guenther, P. H. Chen, F. Simoni, S. S. Slussarenko, O. Francescangeli, and L. Lucchetti, "Dye-doped photorefractive liquid crystals for dynamic and storage holographic grating formation and spatial light modulation," Proc. IEEE **87**, 1897 (1999).

[178] A. Golemme, B. Kippelen, and N. Peyghambarian, "On the mechanism of orientational photorefractivity in polymer dispersed nematics," Chemical Physics Letters **319**, 655 (2000).

[179] J. J. Butler and M. S. Malcuit, "Diffraction properties of highly birefringent liquid-crystal composite gratings," Opt. Lett. **25**, 420 (2000).

[180] M. Levene, G. J. Steckman, and D. Psaltis, "Method for controlling the shift invariance of optical correlators," Appl. Opt. **38**, 394 (1999).

[181] A. Yariv and P. Yeh, *Optical waves in crystals*, (Wiley, New York, 1984).

Acknowledgements